

## ABSTRACT

Title of Document: Ferrocene-based molecular electronics and nanomanufacturing of Pd nanowires.

Lixin Wang, Ph. D., 2007

Directed By: Professor, Lawrence R. Sita, Department of Chemistry and Biochemistry

Two test structures were tried out for molecular junction formation and subsequent I-V characteristics measurements. One is formed by insertion of certain dithiol molecules into an alkanethiol self-assembled monolayer (SAM), followed by tethering the free thiol end with gold nanoparticles. The test structure can then be measured with CP-AFM. The matrix SAM, mixed monolayer with inserted dithiol molecules, and final test structure with gold nanoparticles were prepared and characterized by ellipsometry, AFM and STM. However, the CP-AFM measurements were very irreproducible, even on an alkanethiol SAM. This problem was analyzed and believed to come from two possible causes, namely thermal drift and deformation of the metalized tips.

The other test structure was from insertion of molecules into nanogaps made by electromigration technique. Two molecules were tested and drastically different properties were observed from junctions with each molecule. For Fc-OPE molecules, near perfect conductance peaks ( $>0.6G_0$ ) were observed in some junctions and

analysis indicates that such molecular junction contains only one or two molecules inside the nanogap. The formation of conductance peaks was analyzed with Landauer formula and a simple metal-molecule-metal model. Computational calculation also predicted high conductance through such junctions and the existence of resonant peaks. The junctions with OPE molecules, however, showed poor conductance. Possible causes such as molecular structure and easiness of molecular junction formation were discussed.

In the second part of this dissertation, a new method was developed to fabricate Pd nanowires on HOPG surface using a sacrificial Cu film. The morphology and composition of the nanowires were characterized by AFM, SEM and XPS. The formation of such Pd nanowires was explained with a galvanic displacement mechanism and some test experiments were carried out to prove such growth mechanism. It was also found that the size of the Pd nanowires can be directly controlled by the thickness of the Cu film that was initially deposited. However, attempts to make Au, Pt and Ag nanowires with the same method failed, and possible causes were discussed.

FERROCENE-BASED MOLECULAR ELECTRONICS AND  
NANOMANUFACTURING OF PALLADIUM NANOWIRES.

By

Lixin Wang

Dissertation submitted to the Faculty of the Graduate School of the  
University of Maryland, College Park, in partial fulfillment  
of the requirements for the degree of  
Doctor of Philosophy  
2007

Advisory Committee:  
Professor Lawrence R. Sita, Chair  
Professor Robert M. Briber  
Professor Michael S. Fuhrer  
Professor John T. Fourkas  
Professor Bryan W. Eichhorn

© Copyright by  
[Lixin Wang]  
[2007]

## Acknowledgements

I'd like to thank my advisor, Professor Lawrence R. Sita, for his supervision during my research at the University of Maryland. Professor Sita's tremendous enthusiasm for science, knowledge of the research field and brilliant ideas have benefited my research significantly. I am also very grateful for his encouragement and support, especially during those hard times in my research.

Part of my research was carried out in collaboration with other groups. I'd like to thank Dr. Stephanie A. Getty, Prof. Michael S. Fuhrer in Department of Physics, Rui Liu, San-Huang Ke, Prof. Harold U. Baranger, Prof. Weitao Yang in Department of Chemistry and Department of Physics, Duke University, Xin Zhang and Prof. Robert M. Briber in Department of Materials Science and Engineering, for the beneficial discussions during the collaboration and their partial contribution to my dissertation.

My committee has given me great support for advice and suggestions. Discussion with committee members from different backgrounds and research fields often inspired me and helped me to view problems from different angles. I'd also thank them for their help and advices during my dissertation writing.

Special thanks go to the Sita group, both former and current members: Dr. Chaiwat Engtrakul, Dr. Richard Keaton, Dr. Yonghui Zhang, Dr. Matthew B. Harney, Dr. Denis A. Kissounko, Dr. Albert Epshteyn, Dr. Laura Picraux, Jeniffer Shaw, Andrea E. Young, Erin K. Reeder, Wei Zhang, Hao He and Samuel Hundert. I am grateful not only for their support in the past years, but also for so many joyful moments that I had in this group.

I'd also thank Tim Maugel in the Laboratory for Biological Ultrastructure for SEM and TEM analysis, and Dr. Bindu Varughese for assistance with XPS characterization. Without their help, this work would be impossible.

Finally, I would like to thank my family for their support, especially my grandparents Zhaoming Wang, Wenjing Wang, my parents Shunsheng Wang, Mingying Gong, and my elder brother and sister-in-law Jianxin Wang, Suyuan Huang.

# Table of Contents

Acknowledgements.....	ii
Table of Contents.....	iv
List of Tables.....	vi
List of Figures.....	vii
Chapter 1: Molecular Electronics.....	1
1.1 Basics of Molecular Electronics.....	1
1.1.1 Why molecular electronics?.....	1
1.1.2 Requirements and challenges for molecular electronics.....	3
1.1.3 Early developments of molecular electronics.....	5
1.2 Test structure.....	8
1.2.1 Several known issues about current test structures.....	25
1.3 Theory of charge transfer.....	27
Chapter 2: Molecular electronics based on a conjugated molecule containing a ferrocene unit: CP-AFM studies.....	33
2.1 Introduction.....	33
2.2 Characterization of SAM and doped SAMs with AFM.....	37
2.2.1 Introduction of AFM.....	37
2.2.2 Introduction of self-assembled monolayer (SAM).....	39
2.2.3 Substrate.....	42
2.2.4 Self-assembled monolayer as the matrix layer.....	43
2.2.5 Au nanoparticles.....	47
2.2.6 Au (substrate)-molecule-Au nanoparticle junctions characterized by AFM.....	48
2.3 Characterization of SAM and doped SAMs with STM.....	52
2.3.1 Introduction of STM.....	52
2.3.2 STM tips.....	54
2.3.3 Characterization of pure and doped SAMs with STM.....	59
2.4 Fabrication of Au(substrate)-molecule 1-Au(nanoparticle) junctions.....	74
2.5 I-V measurements of self-assembled monolayer with conductive probe AFM (CP-AFM).....	75
2.5.1 Some considerations about CP-AFM measurements.....	75
2.5.2 CP-AFM set-up.....	80
2.5.3 Results and discussion.....	81
2.6 Experiments.....	88
Chapter 3: I-V measurement on ferrocene-based molecules with break junction test structure.....	97
3.1 Fabrication of Au-molecule-Au test structures in break junctions via electromigration.....	97
3.2 I-V characterization of nanogaps by electromigration without molecules.....	101
3.3 I-V characterization of the Au-molecule-Au test structure.....	102
3.4 Conclusion and future plans.....	113

Chapter 4: Growing Pd nanowires on Highly Ordered Pyrolytic Graphite (HOPG).	115
4.1. Introduction.....	115
4.2 Growth of Pd nanowires on HOPG from a Cu sacrificial film.....	125
4.2.1 Motivation.....	125
4.2.2 Preparing Pd nanowires from Cu sacrificial films.....	130
4.2.3 Further mechanistic study of Pd nanowire formation.....	137
4.2.4 Size control of the Pd nanowires .....	141
4.2.5 Galvanic displacement method for other metals.....	144
4.3 conclusion and future plans .....	147
4.4 Experimental section:.....	149



## List of Tables

Table 1. Thickness measurement of the SAMs with ellipsometry .....	45
Table 2. Standard reduction potentials of some metals and ferrocene derivatives. <sup>181,182</sup> .....	127

## List of Figures

Figure 1. Trend of Fab cost vs. linewidth <sup>3,4</sup> .....	2
Figure 2. An example of a rectifier molecule .....	6
Figure 3. Energy levels of electrodes, acceptor and donor when a) no voltage was applied and b) voltage of one polarity (as shown) was applied. ....	7
Figure 4. Conductive probe AFM measurements on a) octanethiol monolayer, and b) octanethiol monolayer doped with 1,8-octanedithiol which binds an Au nanoparticle. ....	10
Figure 5. Schematic representation of STM measurement of an octanethiol SAM on Au. ....	14
Figure 6. Schematic diagram of a nanopore device <sup>48</sup> . A) Cross section of a silicon wafer with a nanopore etched through a suspended silicon nitride membrane. B) Au-SAM-Au junction in the pore area. C) Enlarged view of B). ....	17
Figure 7. Schematic illustration of a mercury drop junction. Two SAMs were formed on Hg and Ag surfaces before they came into contact with each other. ....	19
Figure 8. A cross-wire junction test structure <sup>41</sup> . I-V characteristics of four classes of molecules were investigated. ....	21
Figure 9. A break junction with gate control. Molecules with Co atom in the center were used. ....	23
Figure 10. Schematic diagram of procedures to form a mechanically controlled break junction <sup>48</sup> .....	25
Figure 11. Energy levels in a metal (L)-molecule (M)-metal (R) model system before (a) and after (b) a bias is applied. ....	29
Figure 12. Cyclic Voltammogram (CV), scan rate 0.1 V/s (top) and Differential Pulse Voltammogram (DPV) (bottom) for A) 1 and B) 2 in 0.1 M [n-Bu <sub>4</sub> N][B(C <sub>6</sub> F <sub>5</sub> ) <sub>4</sub> ] in CH <sub>2</sub> Cl <sub>2</sub> using a glassy carbon working electrode. Potentials are referenced to the redox couple of an internal decamethylferrocene standard <sup>83</sup> .....	33
Figure 13. Similar molecules with different numbers of ferrocene units .....	36
Figure 14. Illustration of AFM concept .....	37
Figure 15. Illustration of formation of self-assembled monolayer. ....	40

Figure 16. Strategy of conductance measurement of single molecules in a SAM matrix with CP-AFM .....	41
Figure 17. Surface images of (a) Si wafer (750 nm × 750 nm scan size) and (b) Au film coated Si wafer (1 μm × 1 μm scan size) .....	43
Figure 18. AFM image of dodecanethiol SAM surface on Au/Cr/Si substrate .....	44
Figure 19. Cyclic Voltammogram of (a) bare gold surface, (b) SAM of hexadecanethiol on Au in 1 M KCl containing 1 mM K <sub>3</sub> Fe(CN) <sub>6</sub> .....	46
Figure 20. TEM images of Au nanoparticles .....	48
Figure 21. AFM surface image of gold nanoparticles tethered on hexadecanedithiol in a dodecanethiol SAM, left: height image, right: phase image .....	49
Figure 22. Section analysis on the AFM height image in Figure 21. ....	50
Figure 23. Illustration of AFM tip convolution which makes small features appear larger in image .....	51
Figure 24. Basic concept of scanning tunneling microscope .....	53
Figure 25. Illustration of an STM tip, which has two "minitips", scanning over sample surface. (a) On a smooth surface, the tunneling current mainly comes from minitip 1, (b) Minitip 2 may cause artifacts when the surface is not smooth. ....	55
Figure 26. SEM images of two mechanically cut STM tips .....	56
Figure 27. SEM image of a heavily contaminated STM tip. ....	57
Figure 28. SEM images of an electrochemically etched STM tip. ....	58
Figure 29. STM images of HOPG with an electrochemically etched tip. (a) height image, (b) current image, inset is 2d spectrum of the height image .....	59
Figure 30. Illustration of the two-layer tunnel junction model .....	60
Figure 31. (top) STM image of dodecanethiol SAM on Au. Inset is the 2D spectrum of the terrace in the middle of the image; (down) section analysis of the height image .....	62
Figure 32. STM height image (top) and schematic representation (bottom) of dodecanethiol SAM with inserted Fc-OPE molecule. ....	67
Figure 33. Cross section analysis of STM constant height image of dodecanethiolate SAM with doped Fc-OPE molecule. ....	68

Figure 34. Analysis of the STM image in Figure 32, assuming each Fc-OPE molecule is perpendicular to the substrate.....	70
Figure 35. Possible conformations of Fc-OPE molecule in dodecanethiolate matrix SAM. Fc-OPE molecule may be bent around the ferrocene unit. ....	71
Figure 36. Possible conformations of Fc-OPE molecule in dodecanethiolate SAM with both ends bonded with the Au substrate. ....	73
Figure 37. AFM image of Au nanoparticles on dodecanethiolate SAM with inserted Fc-OPE molecules, and cross section analysis over one particle. ....	74
Figure 38. Normal sample holder (a) and tip holder (b), in contrast to the home-made sample holder (c) and the tip holder for fluid cell (d).....	76
Figure 39. SEM images of an Au/Cr coated Si tip .....	77
Figure 40. Illustration of capillary force caused by formation of meniscus between tip and sample surface.....	78
Figure 41. Typical force curves under (a) ambient condition and (b) organic fluid... ..	80
Figure 42. Diagram of general set-up for CP-AFM measurement. ....	81
Figure 43. Consecutive three I-V scans on the same spot with CP-AFM on one dodecanethiol SAM, (a) scan range -1.0~1.0 V, (b) zoom in at -0.3~0.3 V.....	83
Figure 44. (a) I-V curves of a 1 M resistor, (b) noise measurement of the open circuit. ....	84
Figure 45. Au coated AFM tips. (a) a fresh one (b) under low bias for a few sweeps (c) after long time use.....	87
Figure 46. Fabrication of STM tips, Step 1. ....	94
Figure 47. Fabrication of STM tips, Step 2. ....	95
Figure 48. A complete test pattern on Silicon wafer. (a) overview, (b) magnified image of the thin gold wire array on top of the common Al gate electrode, (c) one gold thin wire with width of 33 nm.....	98
Figure 49. Illustration of nanogaps formed by electromigration. (a) imaginary side view of the nanogaps, (b) SEM image of a nanogap, inset is illustration of a molecule of ferrocene oligophenylethynyl dithiol bonded to both electrodes inside the nanogap.....	101

Figure 50. I-V characteristics of five nanogap junctions formed in the presence of Fc-OPE. (a) Fc-OPE molecule, (b)-(f): Current (red) and conductance (dark blue, light blue or purple) vs. bias curves. The insets are conductance curves under low bias regions. Gate voltages are: (c) dark blue: -5 V, light blue: 0 V, purple: +5 V (e) dark blue: -1V, light blue: 0 V, purple: +1 V (f) dark blue: +1.1 V, light blue: +1.4 V, purple: +1.7 V. ....	104
Figure 51. Lorentzian fits for conductance curves from Figure 50(b) and (c). The red curve and purple-blue curve are experimental results, and the black curves are Lorentzian fits of the data. ....	108
Figure 52. I-V characteristics of four nanogap junctions formed in the presence of OPE molecules. ....	110
Figure 53. (a) Relaxed configuration of Fc-OPE molecule between two gold (001) leads. (b) The surface of local density of states (LDOS) of the junction at resonant transmission. (c) Transmission between the gold leads (dashed line) and the density of states projected onto the molecule (solid line) at zero bias. ....	111
Figure 54. Metal nanowires from deposition of metal onto positive template wires. ....	116
Figure 55. Fabrication of metal nanowires from a negative template. ....	118
Figure 56. Illustration of metal nanowires fabricated by electrodeposition of metal oxide nanowires followed by reduction. ....	121
Figure 57. Triple-pulse method for nanowire growth. <sup>186</sup> (a) pulse diagram, (b) proposed mechanism. ....	123
Figure 58. Proposed mechanism of galvanic displacement method for metal nanowire fabrication. Reproduced from Dryfe's paper <sup>188</sup> , with permission; copyright 2004, Wiley-VCH Verlag GmbH & Co. KGaA. ....	126
Figure 59. Proposed mechanism for growth of Pd nanowire from the sacrificial Cu film on the edge. ....	131
Figure 60. SEM images of Pd nanostructures on HOPG. ....	133
Figure 61. TM-AFM images of Pd nanostructures on HOPG. ....	134
Figure 62. XPS spectra for (a) Pd and (b) Cu analysis. ....	136
Figure 63. SEM image of Pd nanoparticles at step edges on HOPG. ....	138

Figure 64. Schematic illustration of formation of Pd nanowire loops on HOPG surface .....	139
Figure 65. Pd nanowire loops that formed around monatomic pits on HOPG. ....	141
Figure 66. SEM images of Pd nanowires from Cu films with thickness of (a) 5 nm, (b) 20 nm. ....	144
Figure 67. AFM images of HOPG surfaces in attempts of nanowire fabrication of (a) Ag, (b) Au, (c) Pt .....	146
Figure 68. XPS data from curve fitting of the Pd spec .....	151

## List of Schemes

<b>Scheme 1.</b> Oligophenylene derivatives with 1-3 phenyl groups .....	10
<b>Scheme 2.</b> conjugated molecules. (a) phenylethynyl oligomers, (b) phenylene oligomers.....	15
<b>Scheme 3.</b> Synthesis of compound 2 from compound 1. ....	34
<b>Scheme 4.</b> Molecular representation of a ferrocene-based diode and the proposed schematic describing operation in state 1 and state 2 <sup>83</sup> .....	34

## List of Abbreviations

AFM	atomic force microscope
BDV	breakdown voltages
BE	binding energy
CNT	carbon nanotube
CP-AFM	conductive probe atomic force microscope
CPU	central processing unit
CV	cyclic voltammogram
CVD	chemical vapor deposition
DFT	density functional theory
DNA	deoxyribonucleic acid
DPV	differential pulse voltammogram
Fc-OPE	ferrocene oligophenylethynyl dithiol
GPIB	general purpose interface bus
HOMO	highest occupied molecular orbital
HOPG	highly ordered pyrolytic graphite
LDOS	local density of states
LUMO	lowest unoccupied molecular orbital
NEGF	non-equilibrium Green function
NDR	negative differential resistance
OPE	oligophenylethynyl dithiol
PSt-b-PMMA	polystyrene-b-poly(methyl methacrylate)
PVD	physical vapor deposition



SAM	self-assembled monolayer
SEM	scanning electron microscope
SPM	scanning probe microscope
STM	scanning tunneling microscope
SWNT	single-walled carbon nanotube
TCNQ	tetracyanoquinodimethane
TEM	tunneling electron microscope
TM-AFM	tapping-mode atomic force microscope
XPS	X-ray photoelectron spectroscopy

# Chapter 1: Molecular Electronics

## 1.1 Basics of Molecular Electronics

### 1.1.1 Why molecular electronics?

Molecular electronics, defined as “the set of electronic behaviors in molecule-containing structures that are dependent upon the characteristic molecular organization of space” by Ratner<sup>1</sup>, has attracted growing interests from scientists around the world. One important driving force behind this interest is the increasingly demanding requirements in modern semiconductor industry to make devices smaller. The conventional photolithography based technology has achieved linewidth down to 65 nm nowadays, from a few  $\mu\text{m}$  in 1970s, but this technology will soon reach its limit of miniaturization because of quantum effect and increasing fabrication cost. As scientists try to make transistors smaller and put more transistors on a chip, the leakage current, which is the continued flow of current when a transistor is at “off” state, will increase and thus the whole chip will consume more power and generate more heat. If the size of transistors is small enough, the quantum tunneling of the carriers, electrons and holes, will become too great for the transistor to operate properly. The other limiting factor is the increasing cost to develop complex instruments and plants for smaller linewidth with conventional lithography technology. This is described as “Rock’s Law” or “Moore’s second Law”<sup>2</sup>, which states that the cost of building a semiconductor fabrication plant, which is usually

called “fab” in the industry, will double every 4 years. Figure 1 shows the trend of fabrication plant cost vs. linewidth during the past 30 years or so. A fab cost 20 million dollar to build in 1970s (with linewidth 3.5  $\mu\text{m}$ ), while it cost 2-3 billion dollar to build one fab in 2005 with 90nm linewidth<sup>3,4</sup>. At this rate, it will become economically infeasible to build a fab in the near future. Such difficulties have forced the chip manufacturers to seek other ways to enhance CPU performance, instead of purely by pushing smaller linewidth and higher working frequency of CPUs. A good approach is to put 2 or more cores in one CPU.

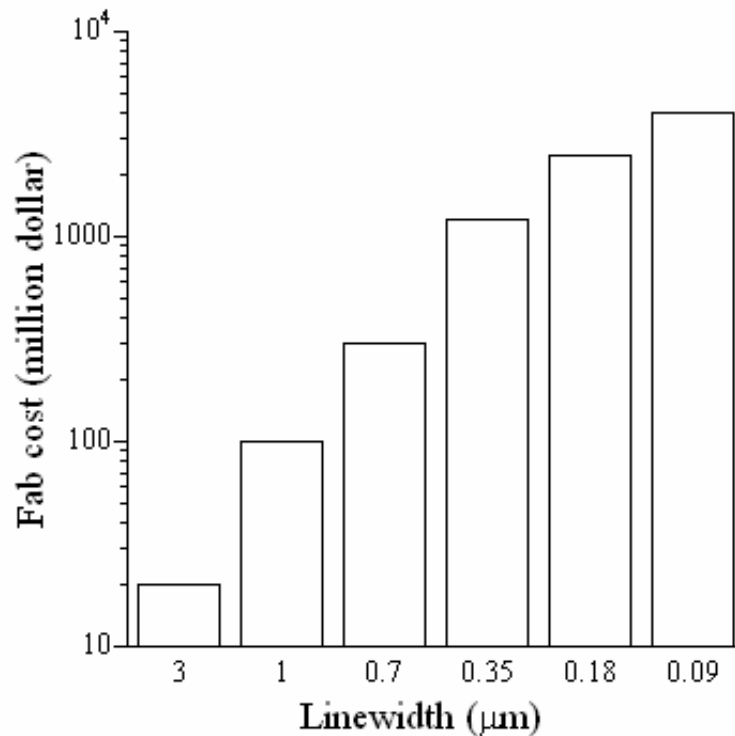


**Figure 1. Trend of Fab cost vs. linewidth<sup>3,4</sup>**

Due to these physical and economical difficulties with the conventional photolithography based technology, people started to look for potential alternatives which can provide smaller feature size and be more affordable. Single molecules came into scientists’ sight immediately because they have some obvious advantages.

First, most molecules are small, with typical length less than a few nm. Second, organic synthesis is a quite developed science. Molecules can be modified with different functional groups to give desired properties. Third, since the discovery of self-assembly of some organic molecules on gold surfaces<sup>5</sup>, people believe this may provide a solution to integrating large quantities of electrical components on a small area, if organic molecules can be these “electrical components”. Because this kind of self-assembly can happen in solution, the production cost can be decreased significantly compared to current photolithography method which requires very complicated and expensive instruments.

### **1.1.2 Requirements and challenges for molecular electronics**

Before molecular electronics comes into reality and be industrialized, some issues need to be solved.

First, a detailed study of the electronic properties of molecules is required to answer the following questions: 1) How does the current flow through molecules? 2) What is the relationship between the electronic properties and molecular structures? 3) How can the molecule-electrode interface affect the whole properties of molecular devices? 4) How can the electronic properties of molecular devices be controlled externally, for example, by an electrical field or magnetic field? This imposes challenges to both the experimentists and theoretical researchers. Experimentally, due to the small size of molecules, it is nontrivial to fabricate a junction with the right gap size to fit in the desired molecules. Recent studies showed that molecule-electrode interface plays an important role in determining the molecular device properties, thus it would be desirable to fabricate electrodes with controllable shape, ideally at atomic

precision. Such electrodes can only be fabricated with scanning tunneling microscope (STM) currently<sup>6</sup>, but STM requires a conductive substrate, which severely limits its application. Theoretically, it is still not well understood how the discrete molecular energy levels align with the continuous energy band structures in the bulk electrodes. Little is known about how to predict the electrical properties such as conductance when a small modification is made to the molecules.

Second, the stability of molecular devices needs to be considered. Chemically, the molecules should be stable during the lifetime of the corresponding molecular devices. They should not decompose over a long time, and should be chemically inert to their working environment. Thermal stability is another issue to consider. Molecules may diffuse on electrodes, because the molecule-metal bond is not a strong bond. The Lindsay group<sup>7</sup> observed stochastic on-off conductivity switching in octanedithiol, decanedithiol and dodecanedithiol on Au, and they ascribed the cause to the well-known mobility of molecules tethered to Au surface through S-Au bond. They also found the switching rate increased substantially when they increased the temperature from 25 °C to 60 °C. Such switching behavior and its temperature dependence should be characterized carefully when researchers design new molecular devices.

Third, how to assemble molecules to their desired sites on a chip may prove to be another challenge. There can be many different molecular components on one chip, thus assembling one kind of molecules at each step can increase the production cost dramatically. So the desirable case would be assembling different kinds of molecules at one time. However, that may cause problems with molecules interfering with each

other. To solve this problem, more molecule-electrode bond structures need to be tested besides the current popular S-Au bond structure. Si-C bonding<sup>8-12</sup> has shown to be one of the candidates of interest, as Si is currently the dominant material used in the semiconductor industry. Replacing the Au with another metal such as Pt<sup>13</sup>, or with SWNTs<sup>12,14</sup>, also seems promising.

Other challenges may appear as molecular electronics goes from lab to market. It has already been pointed out that power consumption, heat dissipation and interconnections can be big hurdles for developers<sup>15,16</sup>. Heat dissipation has already been a big problem for current Si based semiconductor industry. The state-of-the-art Pentium 4 CPU has around 125 million transistors, with power density around 100 W/cm<sup>2</sup>, which is much higher than a hotplate (~10 W/cm<sup>2</sup>) and thus requires a large heatsink/cooling fan to dissipate the heat generated by the CPU. If a single molecule can act as transistor, one can potentially integrate orders of magnitude more transistors on the same area as the current CPUs, due to the much smaller feature size of molecules. The power density would be impractically high if each “molecular transistor” consumes the same energy as the ones used in current CPUs. At the same time, the feature size of interconnection wires should also scale down to be comparable with the corresponding molecular components. This would also be challenging as it is beyond the capability of current lithography techniques.

### **1.1.3 Early developments of molecular electronics**

The earliest studies of electrical properties of molecules were carried out on monolayers of molecules. In 1971, Mann and Kuhn<sup>17</sup> studied tunneling through monolayers of Cd salts of fatty acid CH<sub>3</sub>(CH<sub>2</sub>)<sub>n</sub>COOH with different chain length, i.e.,

different values of  $n$ . The monolayers were fabricated between Al and another metal (Hg, Pb or Al). They observed exponential decay of current with molecular length and it agreed well with theoretical expectation based on the assumption that the current just tunneled through the monolayers.

Mann and Kuhn used the fatty acid salt monolayers just as some insulating layers, instead of active elements in the circuit. The first use of organic molecules as “active” elements can be traced back to 1974 when McGinness and coworkers<sup>18</sup> reported a voltage-controlled bistable switch, in which the electrical property was determined by melanin, a mixed polymer of polyacetylene, polypyrrole, and polyaniline. Such switching properties were maintained even after 3.5 hours of continuous testing.

Also in 1974, Aviram and Ratner<sup>19</sup> proposed a theoretical molecular rectifier. The molecules they used contained an acceptor site and a donor site. (See Figure 2) The donor and acceptor sites were effectively insulated from one another by a “bridge” part so that the energy levels of the donor and acceptor wouldn’t interact with each other and thus can be treated separately.

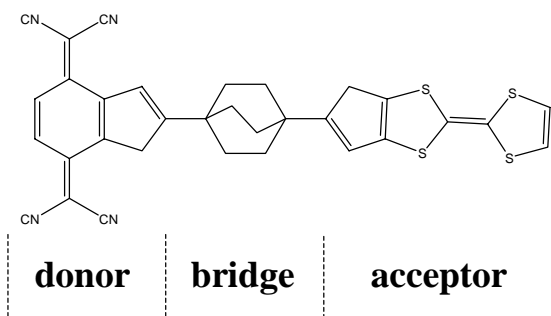


**Figure 2. An example of a rectifier molecule**

A simple model was proposed to explain the mechanism of the molecular rectifier. Figure 3(a) shows the relative energy levels of 2 electrodes and the donor

and acceptor. The Fermi levels of the electrodes usually lie between the highest occupied molecular orbital (HOMO) and the lowest unoccupied molecular orbital (LUMO) of both the donor and acceptor sites. In order for electrons to flow, some voltage of proper polarity needs to be applied, so that the Fermi level of the left electrode is higher than the LUMO level of the acceptor and the HOMO level of the donor is higher than the Fermi level of the right electrode. The electrons can then tunnel from left electrode to the LUMO level of the acceptor, then tunnel to the HOMO level of the donor, and finally tunnel to the right electrode, as shown in Figure 3(b). In order for electrons to flow when voltage of reversed polarity is applied, much higher voltage is required. Thus in certain range of voltage, electrons can only flow in one direction, which behaves just like a rectifier.

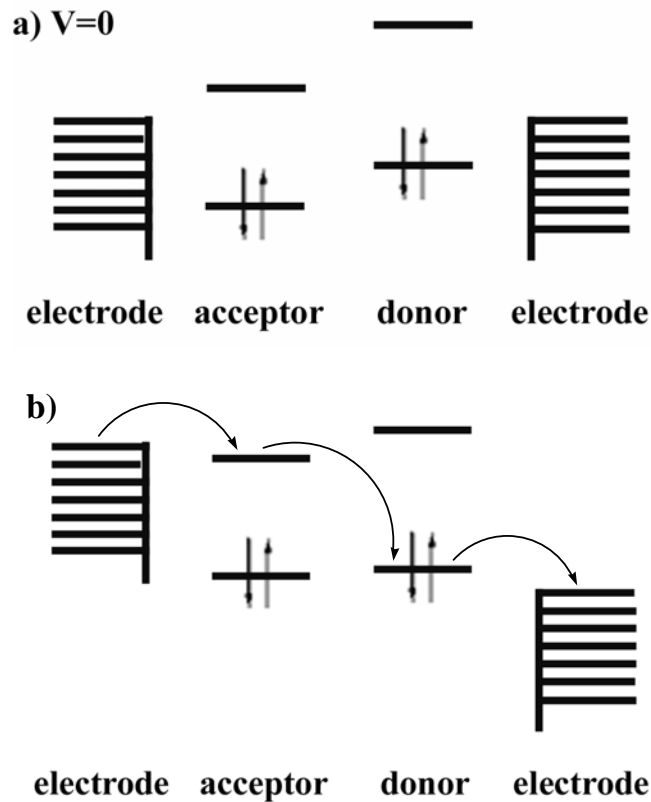


**Figure 3.** Energy levels of electrodes, acceptor and donor when a) no voltage was applied and b) voltage of one polarity (as shown) was applied.



In 1988, Aviram further proposed a molecular switch and possible use of the same molecule memory and logic<sup>20</sup>. The molecule can be turned from insulating to conductive or vice versa by external electronic field, which makes the “switch” to be “on” or “off”.

Inspired by these exciting simple theoretical models, researchers tried to test these ideas by experiments. The following development of molecular electronics consists of not only attempts to find molecules with interesting electronic properties, but also attempts to find good test structures to test these molecules.

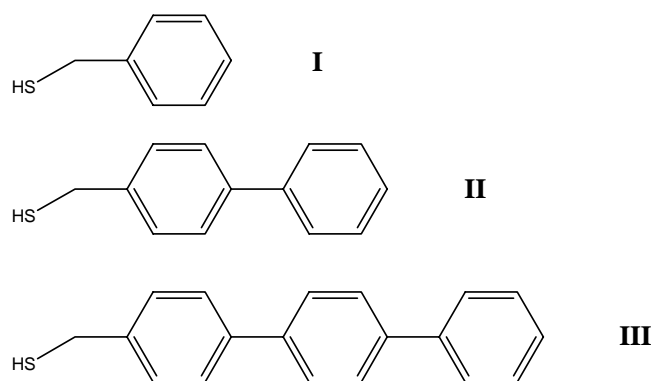
### **1.2 Test structure**

To study the electrical properties of molecules, one starts by measuring the conductance of molecules. Theoretically, with an appropriate test structure, the voltage ( $V$ ) and current ( $I$ ) across the molecule or monolayer can be measured and the conductance ( $g$ ) can be calculated simply by equation  $g(V) = \frac{I}{V}$ . However, due to the small size of molecules, researchers have had difficulties to find a reliable test structure. Furthermore, to avoid possible contamination or reaction with oxygen and water, most measurements were conducted under protective environments such as under an inert gas, in a protective inert organic solvent, or under ultra high vacuum, which add more restrictions for the design of a test structure. To date, researchers have tested molecule-based devices by experiments based on conductive probe atomic force microscope (CP-AFM) on monolayers<sup>7,21-37</sup>, scanning tunneling microscope (STM) on monolayers<sup>38-45</sup>, nanopores<sup>46-51</sup>, mercury drop junctions<sup>52-54</sup>, cross-wire junctions<sup>55-57</sup>, break junctions formed from electromigration<sup>58-61</sup> of tiny

wires, and mechanically controlled break junctions<sup>62</sup>. The details of each technique will be discussed below.

#### 1. CP-AFM on monolayers.

Frisbie and co-workers<sup>22-24,36,37</sup> measured the resistance of an alkane thiol monolayer by placing a conductive AFM tip onto self-assembled monolayers (SAM) formed through chemisorption of alkanethiol onto gold surfaces. Figure 4(a) shows such a set-up, where the conductive tip and the gold substrate act as two electrodes. They measured the current through the monolayer by applying bias on the tip, and from the data the resistance of the monolayer could be obtained. SAMs derived from alkanethiol,  $\text{CH}_3(\text{CH}_2)_n\text{SH}$ , with  $n$  in the range of 5 to 16, were measured and it was found that the I-V curves were approximately linear in the -0.3 V to +0.3 V region. The results agreed with the proposed coherent nonresonant tunneling mechanism, in which resistance ( $R$ ) increases exponentially with tunneling distance ( $d$ ), as  $R = R_0 \exp(\beta d)$ , with  $R_0$ ,  $\beta$  being constants. From the plot of resistance vs number of carbons in the alkane chain, the constant  $\beta$  was determined to be 1.19 per methylene group, or  $1.10 \text{ \AA}^{-1}$ . SAMs derived from chemisorption of oligophenylene derivatives I-III (Scheme 1) were also studied with this technique, and the  $\beta$  constant was determined to be  $0.41 \text{ \AA}^{-1}$ . The difference of the  $\beta$  constants was ascribed to the structural difference between these oligophenylene derivatives and the alkanethiols. Besides, these researchers also found that the I-V curves were strongly influenced by the tip load force and the tip radius, as both would affect the tip-SAM contact area and the extent of SAM deformation.



**Scheme 1.** Oligophenylene derivatives with 1-3 phenyl groups

While such an Au-SAM-probe test structure is easy to make, the resistance of a single molecule cannot be obtained, as the exact number of molecules under the probe is unknown. Furthermore, the contact between the surface of the monolayer and the AFM probe is susceptible to contamination. The same investigators also believed that contamination layers of uncontrolled thickness were the primary factor contributing to the tip-to-tip variance in these CP-AFM measurements<sup>63</sup>.

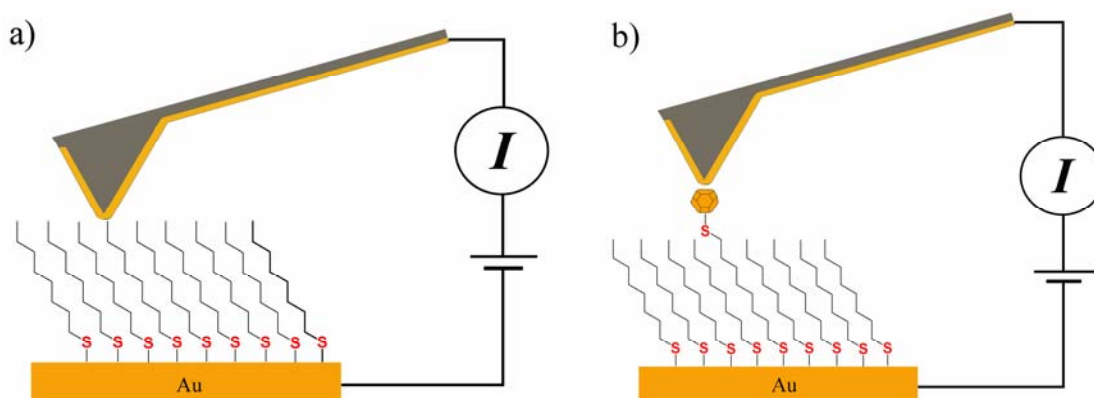


**Figure 4.** Conductive probe AFM measurements on a) octanethiol monolayer, and b) octanethiol monolayer doped with 1,8-octanedithiol which binds an Au nanoparticle.

Lindsay<sup>7,21,25-29,35</sup> used a similar experimental test design to measure the resistance of alkanedithiols (Figure 4(b)). Alkanedithiol adsorbates were first doped into a SAM derived from alkanethiol, and then the sample was placed in a solution

containing Au nanoparticles in order to tether Au nanoparticles onto the free thiol groups of the doped alkanedithiol adsorbates. A conductive AFM tip was then placed on top of the Au nanoparticles and the current collected. While it was believed that the molecule-metal contact was better in this test structure due to the chemical bond between the nanoparticle and the dithiol adsorbates, further investigation indicated that the introduction of the nanoparticle into the conducting pathway might also introduce a new problem, namely the contact resistance of the AFM tip and the nanoparticle. More specifically, since the nanoparticle already has a stabilizing ligand layer initially, the contact between the tip and the nanoparticle may not form metallic bonds. As a result, the Coulomb charging energy (i.e., “Coulomb blockade”<sup>64</sup>) of the nanoparticle needs to be overcome before current can flow through. Nevertheless, these investigators found that the results were quite reproducible, and the I-V curves obtained were quantized, indicating current through different numbers of molecules. From these I-V curves, resistance of single molecules, or more strictly, resistance of Au-single molecule-Au nanoparticle junctions, can be determined. These researchers studied octanedithiol, decanedithiol and dodecanedithiol molecules, and their resistances turned out to be  $0.965 \pm 0.02 \text{ G}\Omega$ ,  $2.89 \pm 0.5 \text{ G}\Omega$  and  $8.26 \pm 1 \text{ G}\Omega$ , respectively. Compared with the Au-alkanethiolate SAM-probe junctions, these Au-alkanedithiolate-Au nanoparticle/probe junctions showed to be orders more conductive and not as sensitive to the force of the probe. The  $\beta$  constant was found to be  $0.57 \pm 0.03$  per methylene group, or approximately  $0.53 \text{ \AA}^{-1}$ , which is significantly smaller than that measured from alkanethiol monolayer by Frisbie’s group. This effect was attributed to the large shift in molecular levels upon formation

of chemical bonds to gold at both ends of the molecule. In a recent paper on a carotene dithiol adsorbate, the same investigators found that by taking account of charging caused by the gold particle, the calculated I-V curve agreed with the experimental I-V data quite well<sup>25</sup>. However, the introduction of gold nanoparticles in this test structure made the data analysis more difficult, and thus prevents the wide application of this technique.

Instead of using self-assembled monolayers, Tao's<sup>30-34,65-67</sup> group measured the conductance of molecules by repeatedly moving a conductive AFM tip or STM tip into and out of contact with a gold surface in the presence of dilute dithiol or bipyridine adsorbate solution. Using this technique, it is hypothesized that some gold-molecule-gold junctions would form and break during this process, and indeed, these investigators observed staircase features on the conductance-distance map during retraction from the surface, indicating breaking of individual metal-molecule-metal junctions. Several molecules, such as 4, 4'-bipyridine, hexanedithiol, octanedithiol, decanedithiol, were measured and the resistance of each single molecule was obtained. The results of conductance for alkanedithiols were in good agreement with the first-principles calculations, but were about an order of magnitude larger than the results found by Lindsay's group. The absence of gold nanoparticle was believed to account for this difference between the results of these two groups, as the suppression of transmission due to the nanoparticle was avoided here. For the alkanedithiol molecules, the  $\beta$  constant was found to be  $1.04 \pm 0.05$  per methylene group, or  $\sim 0.83 \text{ \AA}^{-1}$ . Venkataraman *et al.* studied the effects of different binding groups of the molecules in this technique. Molecules with diamine, diisonitrile and dithiol end

groups were studied<sup>68</sup>, and it was found from the conductance-distance maps that diamine molecule-Au junctions gave far better resolved staircase features than junctions from the other two kinds of molecules. It was proposed that the amine-Au binding provides sufficient angular flexibility to facilitate junction formation while maintaining the electronic coupling of the N lone pair to the Au atom. Measurements from alkanediamine molecules gave  $\beta$  constant around  $0.77 \text{ \AA}^{-1}$ , which is close to Tao's result. Venkataraman and co-workers also studied a series of substituted benzene diamine molecules<sup>69</sup>, and the results demonstrated that electron-donating substituents increased the junction conductance while the electron-withdrawing substituents had the opposite effect.

## 2. STM on monolayers.

Tour and Weiss<sup>38-45</sup> used STM to study electron transport through monolayers by letting the STM tip sit on the monolayer and measuring the current through the molecules (Figure 5).

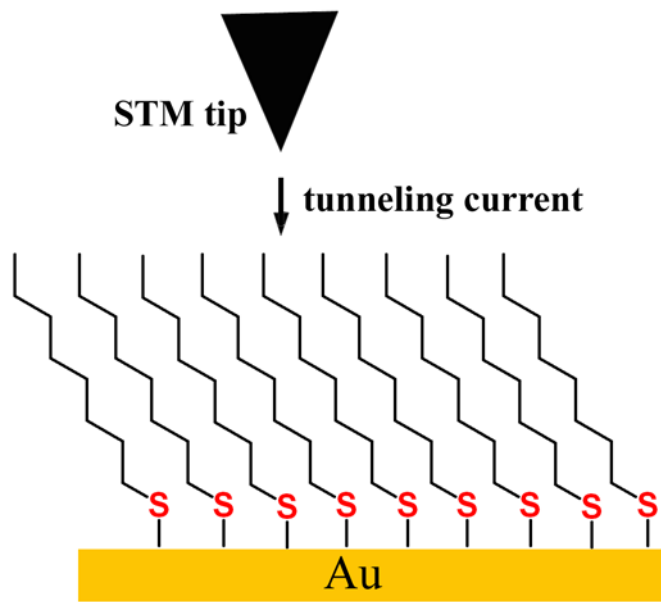
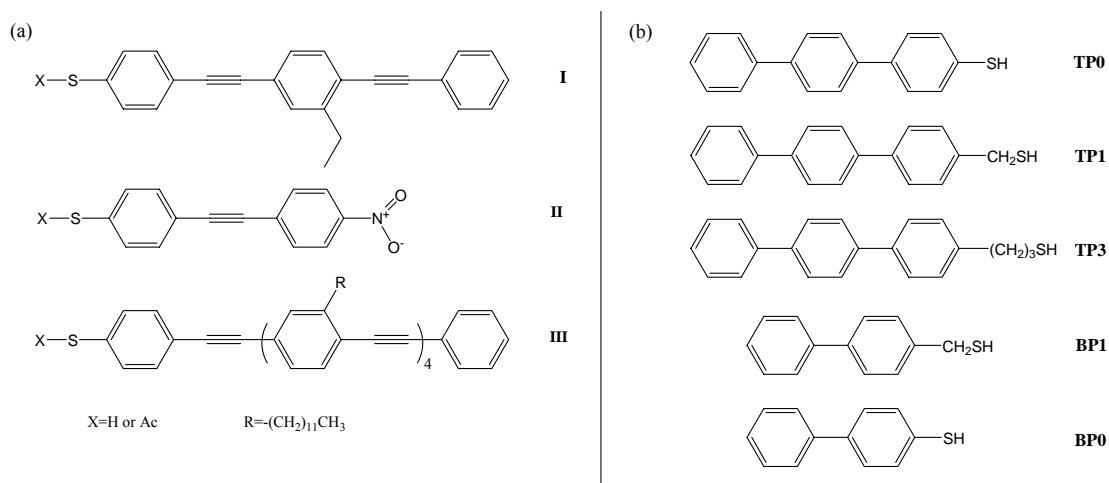


**Figure 5. Schematic representation of STM measurement of an octanethiol SAM on Au.**

Dunbar, Cygan and co-workers<sup>43,45</sup> studied a series of conjugated molecules (Scheme 2(a)) that were doped into alkanethiol monolayers. From the STM images under constant current mode, these phenylethyne oligomers appeared higher than the surrounding matrix monolayers, even in the case where the height of molecule II in Scheme 2(a) is physically shorter than the surrounding dodecanethiol SAM. The results strongly indicated that these oligomers were more conductive than the surrounding alkanethiolate molecules, which was believed due to the conjugated backbones in these molecules. Ishida and co-workers<sup>42</sup> studied another series of model molecules (Scheme 2(b)) that were doped into nonanethiol SAM. By varying the number of phenyl and/or methylene groups, the resistance of the model molecules could change from being smaller (BP1) to being larger (TP1, TP3) than the matrix nonanethiol molecule. Unfortunately, all these experimental results were difficult to interpret quantitatively because it is hard to know the exact distance between the tip

and the surface, thus the contribution of the tip-sample spacing to the total resistance is unknown.



**Scheme 2.** conjugated molecules. (a) phenylethynyl oligomers, (b) phenylene oligomers.

To precisely locate the tip position relative to the SAM surface, Fan and co-workers<sup>38-41</sup> modified the STM by attaching the tip to a tuning fork, which was excited by an attached piezoelectric element. When the tip approaches the SAM surface and just contacts the surface, the oscillation amplitude and frequency would decrease, and thus the accurate tip position can be determined. With this technique, these investigators studied several phenylene-ethynylene oligomers and obtained I-V curves for the SAMs derived from these oligomers. They found sharp peaks in these I-V curves and further discovered good correlation between these peaks and computed LUMO energies in these oligomer molecules. However, their I-V curve for dodecanethiol SAM was quite different from the results obtained by Frisbie and Lindsay groups. The nature of the tip-SAM interface in this technique is still questionable. For example, where is the exact position of the tip when the change in



oscillation amplitude can be detected? Is it right on the end groups of the SAM molecules, like  $-\text{CH}_3$  in the alkanethiol case, or the tip end has already moved certain distance into the SAM? Answers to these questions would be crucial for researchers to evaluate this technique and its possible applications.

### 3. Nanopores.

Reed and Tour<sup>46-51</sup> reported a nanopore test structure to measure the I-V curves of a monolayer (Figure 6). This experimental design is based on a  $\text{Si}_3\text{N}_4$  membrane with nanopores ( $\sim 30\text{nm}$  in diameter) inside. To fabricate this structure, a gold film was first evaporated on one side of the membrane, followed by forming a monolayer inside the nanopores, and then another layer of Au was evaporated on the other side of the membrane to form Au-monolayer-Au junctions. Some interesting phenomena were observed with this test structure on different molecules. For example, I-V curves showed prominent rectifying behavior on biphenylthiolate monolayer, which was believed to be the result of the asymmetric nature of the junctions. Negative Differential Resistance (NDR) was observed in I-V characteristics of an Au-(2'-amino-4-ethynylphenyl-4'-ethynylphenyl-5'-nitro-1-benzenethiolate)-Au junction (Figure 6(c)). Further experiments demonstrated that the nitro group accounts for the NDR behavior, but exact mechanism is still unknown.

While this test structure can be used for most monolayers, it can't measure I-V curves of single molecules due to the large pore size, and the evaporation of Au onto the monolayer may introduce some problems. More specifically, the Au atoms may

penetrate through the monolayer via defects and form an alternate conducting path for electron transfer as a result.

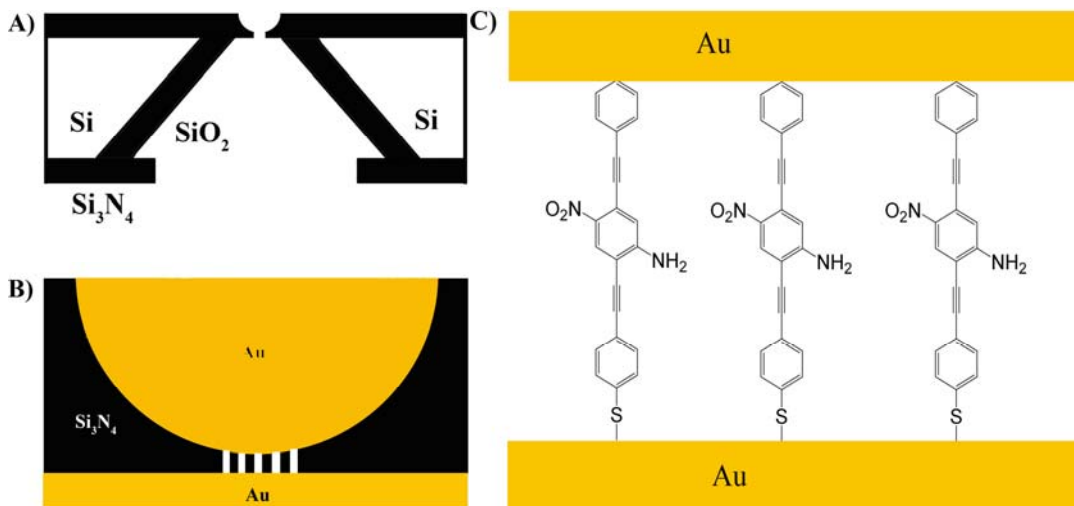


**Figure 6. Schematic diagram of a nanopore device<sup>48</sup>. A) Cross section of a silicon wafer with a nanopore etched through a suspended silicon nitride membrane. B) Au-SAM-Au junction in the pore area. C) Enlarged view of B).**

#### 4. Mercury drop junctions

Whitesides and co-workers<sup>52-54</sup> studied electron transport through organic films with a Hg/monolayer 1//monolayer 2/metal test structure shown in Figure 7. To fabricate this device, a mercury drop is brought towards a metal (Ag or Au) surface within a thiol solution. As the mercury drop approaches the surface, it deforms to make a good contact. This test structure can be used to measure most SAMs derived from organothiols, and the fabrication is quite straightforward. Alkanethiols and oligophenylene thiols of different lengths were studied by this test structure. The  $\beta$  constant was found to be  $0.87 \pm 0.1 \text{ \AA}^{-1}$  for alkanethiols, which was close to Frisbie's and Tao's results, and  $0.61 \pm 0.1 \text{ \AA}^{-1}$  for oligophenylene thiols. The electrical breakdown voltages (BDV) of these junctions were also studied. It was found that for the same SAM, BDV depends on the metal substrate because the same SAM

molecules would have different tilt angles on various substrates. SAMs with higher tilt angle exhibit lower BDV, which is not surprising since higher tilt angle means thinner SAM and higher electrical field under the same bias. These investigators also found rectification behavior in I-V characteristics from junctions where one SAM formed from molecules containing a tetracyanoquinodimethane (TCNQ) unit.

On the other hand, the nature of the monolayer 1//monolayer 2 interface in this test structure is unknown, and in this regard it is possible that small pockets of solvent can remain at the interface. The use of mercury, which is toxic and volatile, also greatly limits the practical application of this test structure. Finally, due to the relatively large contact area, this test structure is not suitable where the measurement of single molecule conductance is desired.

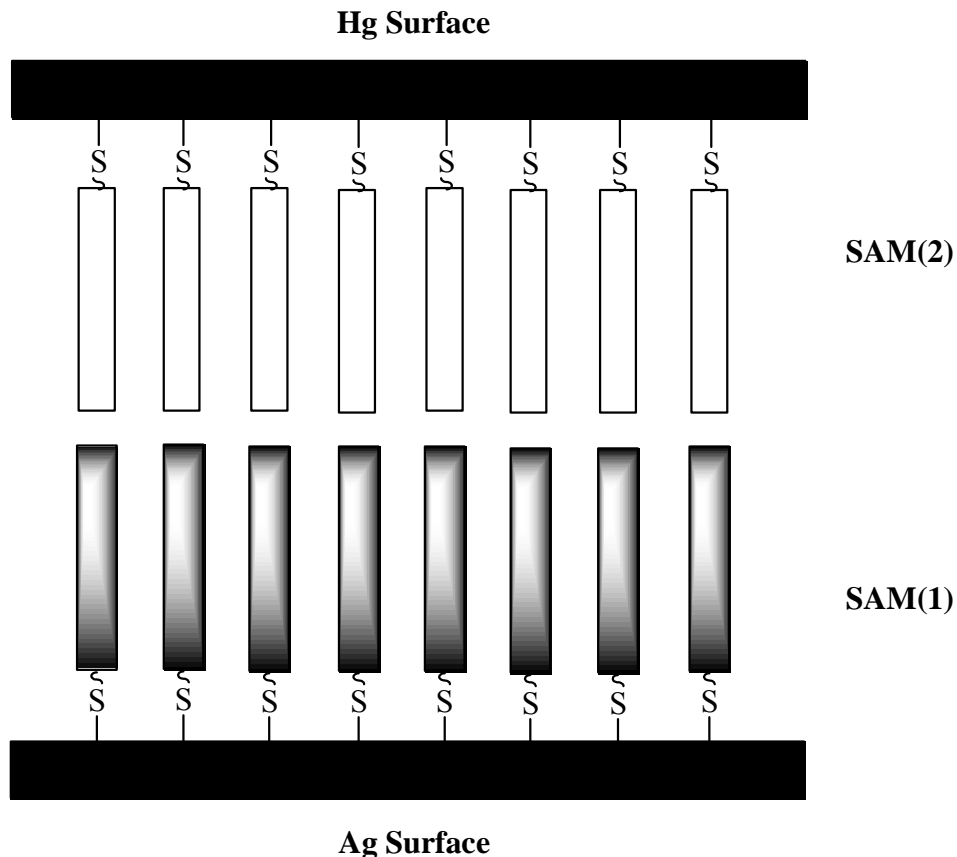


**Figure 7. Schematic illustration of a mercury drop junction. Two SAMs were formed on Hg and Ag surfaces before they came into contact with each other.**

## 5. Cross-wire junctions

Kushmerick, Shashidhar and co-workers<sup>55-57</sup> developed the cross-wire junction technique shown in Figure 8. In this test structure design, two gold wires are crossed and brought close to each other using a custom-built test stage. One gold wire is covered with a self-assembled monolayer derived through the chemisorption of organothiols, and the other one is bare gold. DC current is applied to one wire and it generates Lorentz force in an external magnetic field, which is used to control the relative distance of the two wires. The current is slowly increased to bring the two wires gently together to form a metal-molecule-metal junction. The contact area can

be varied by changing the dc deflection current. Typical number of molecules sandwiched in the junctions was estimated to be around 1000. I-V curves obtained from junctions containing dodecanedithiolate (C12), oligo(phenylene ethynylene) dithiolate (OPE) and oligo(phenylene vinylene) dithiolate (OPV) (Figure 8) showed the trend of molecular conductance to be  $C12 < OPE < OPV$ . It was previously believed that the higher coplanarity and thus better  $\pi$ -conjugation of OPV molecule made it more conductive than the OPE molecule. But the calculation results by these researchers indicated that the higher conductivity in OPV molecule was due to the smaller bond-length alternation in OPV than that in OPE. I-V curves from junctions made from OPE dithiolate and thiolate were compared to study the effect of symmetry of metal-molecule contact conditions on charge transport. Symmetric I-V curves were obtained from junctions with OPE dithiolate under symmetric metal-molecule contacts, while junctions from OPE thiolate, where the metal-molecule contacts were unsymmetric, exhibited rectifying I-V characteristics. Similar contact effects on charge transport were also reported by Tour and Whitesides. This test structure couldn't form a single molecule junction, but it was found that the I-V curves are quantized and a "reduced" I-V curve could be obtained by dividing the I-V curves by different integer divisors, a similar process done by Lindsay's group.

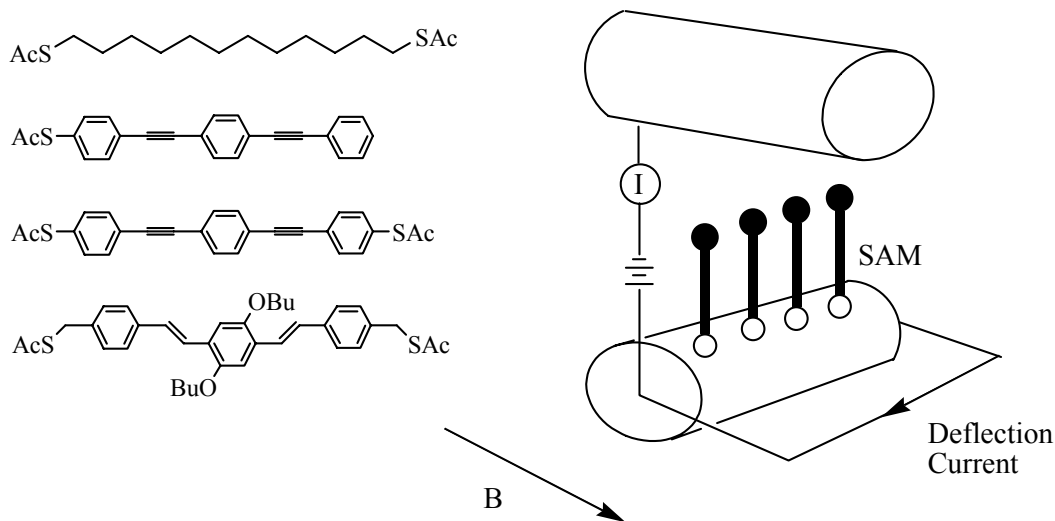


**Figure 8. A cross-wire junction test structure<sup>41</sup>. I-V characteristics of four classes of molecules were investigated.**

## 6. Break junctions by electromigration.

It would be natural for researchers to seek ways to fabricate two electrodes a few nanometers apart and put one or a few molecules between to form a junction. Though the idea appears very simple, researchers found it not an easy task to consistently fabricate electrodes just a few nm apart. Park, McEuen and coworkers<sup>58-61,70</sup> used electromigration to make these nanogaps and it proved to be a reliable technique to fabricate such nanogaps. These researchers fabricated a thin gold wire (200 nm in width and 10-15 nm in thickness) via e-beam lithography, and then applied current through this wire. Electromigration of Au atoms would happen when the current overpasses certain critical value. A gap was formed when there was an abrupt drop in conductance, which was further confirmed by HR-TEM. To make a single-molecule junction, usually a dithiol molecule monolayer was first formed on the gold wire and then the electromigration was conducted. It was hypothesized that

some molecules would also migrate during the process and part of them would fall into the gap and form metal-molecule-metal junctions (Figure 9). This technique has shown some advantages:

- a) Single molecule junctions might be obtained.
- b) The junctions were found to be quite stable, which means different measurements can be carried out on the same junction. This may be due to the fact that the experiments were conducted under low temperature and thus the distance between the leads can be accurately controlled by minimizing thermal drift.
- c) A gate can be fabricated underneath the junction. Thus it is possible to tune the electrical level of the molecule with the gate voltage.

McEuen and co-workers successfully fabricated single molecule transistors using this technique. Coulomb blockade<sup>71</sup>, a phenomenon that was first observed in charge transfer through a quantum dot between two electrodes where an electron must overcome the “charging energy” to transfer from one electrode to the quantum dot, was observed from devices with the  $\text{Co}(\text{tpy}-(\text{CH}_2)_5\text{-SH})_2$  molecule. The width of Coulomb blockade could be controlled by changing the gate voltage. By analyzing the Zeeman splitting under external magnetic field, these researchers were able to determine that the Co atom has spin 1/2 for the +2 charge state and spin 0 for +3 charge state, which agreed well with previous chemical studies. For devices from the  $\text{Co}(\text{tpy-SH})_2$  molecule, another interesting phenomenon known as Kondo effect<sup>72</sup> was observed. Kondo effect usually happens in systems with magnetic impurities like unpaired electrons, and exhibits as increased resistivity at low temperatures. Park and

co-workers also found Kondo effect in their molecular device made from divanadium molecules. The presence of Kondo effect was confirmed in both groups by the observation of 2 signature characteristics of Kondo effect: the temperature dependence of Kondo peak and the Kondo peak splitting in an external magnetic field.

Compared to other test structures, this one takes more effort to fabricate the patterns, and the success rate of getting molecular junctions when breaking the gold wire was only ~10%, but real single molecule junctions and the availability of gate control make this technique very attractive to researchers in this field.

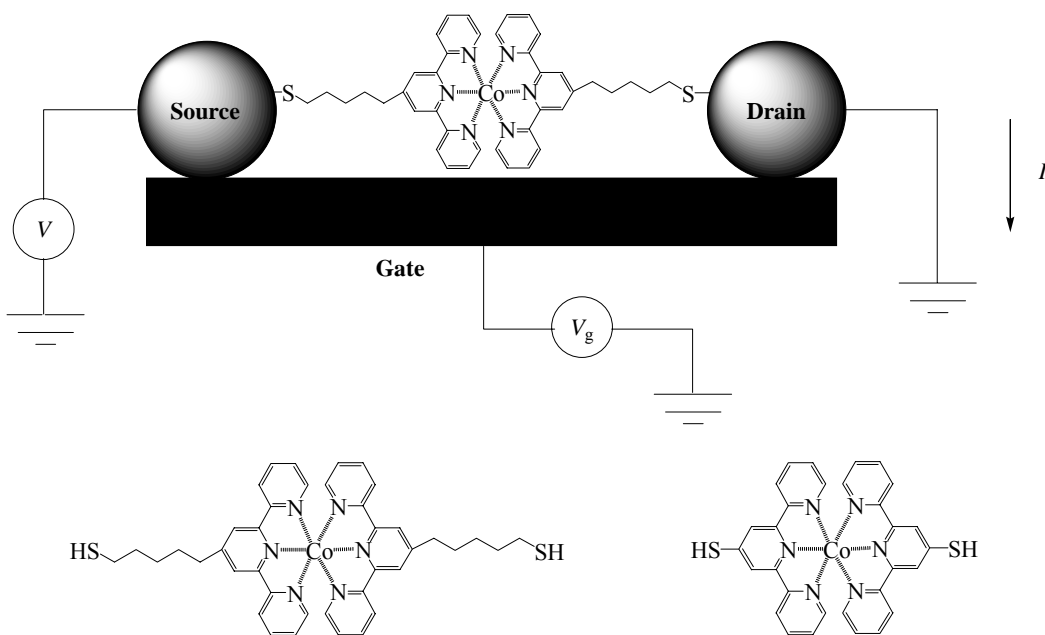


**Figure 9. A break junction with gate control. Molecules with Co atom in the center were used.**

## 7. Mechanically controlled break junctions

Reed, Tour and co-workers<sup>62</sup> once developed a mechanically controllable break junction to study the conductance of short molecules like benzene dithiol (Figure 10). Two electrodes were first fabricated by breaking a gold wire mechanically, and then



self-assembled monolayer of benzene dithiol was formed on both electrodes. The two electrodes were brought close together precisely with a piezo element. The spacing between the two electrodes was controlled to be approximately the length of the molecule so that metal-molecule-metal junctions could form. These researchers were able to obtain I-V curves from junctions containing benzene dithiol molecules. The curves were quite reproducible and they observed gap around zero voltage, which was possibly due to Coulomb blockade. However, lack of gate control in these junctions prevented definitive demonstration of Coulomb blockade. In fact, the molecular junctions made in this way are quite crude because: a) the geometry of the electrodes is poorly controlled. The cross section area of the initial gold wire is on the scale of micrometer, which is too large for molecular electronics. The geometry of the electrodes can vary vastly from sample to sample; b) it is not certain if there are any molecules that form chemical bonds with both electrodes. There maybe just physical contact at one end of the junction; c) these researchers made the monolayer on the electrodes by letting the THF solution evaporate, which may result in multiple layers on the electrodes.

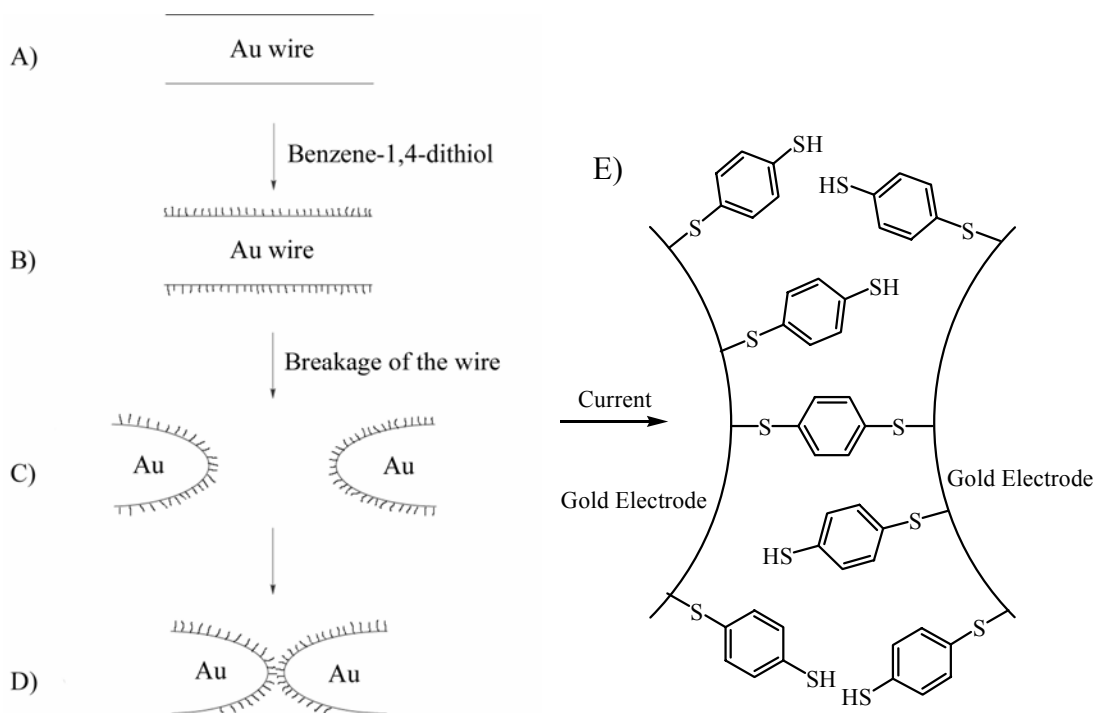


**Figure 10. Schematic diagram of procedures to form a mechanically controlled break junction<sup>48</sup>.**

### 1.2.1 Several known issues about current test structures.

The above test structures, although not perfect, have provided researchers basic tools to study and understand the electrical properties of molecules, and many interesting results have been obtained. However, more strict scrutiny and some recent experiment results raised questions about some of these test structures.

Collier *et al*<sup>73,74</sup> fabricated cross wires with rotaxane or catenane molecules sandwiched between the wires, similar to the cross-wire test structure in Figure 8. They found switching behavior in these metal-molecule-metal structures, which they attributed to the conductance change when the molecules were reduced or oxidized. However, Lau and co-workers<sup>75</sup> studied a test structure with a monolayer of stearic acid ( $C_{18}H_{36}OH$ ) sandwiched between planar Pt and Ti electrodes, and reversible switching behavior was also observed. Since the molecule has no redox centers, it is

unlikely that such switching behavior was caused by the redox behavior of the molecules. Further investigation, with the help of AFM revealed to apply local mechanical pressure on top of one electrode, revealed that the “on” (high conductance) and “off” (low conductance) state of the device was accompanied invariably with the appearance and disappearance of a local “switching center”. It was proposed that a metal nanofilament was formed during the “on” state and the formation of the filamentary pathway accounted for the change of conductance. The growth of the nanofilament may be driven by the increasing current density and/or electrical field between the metal electrodes. If this is true, extra caution should be taken during data collection and interpretation when a metal-molecule-metal test structure is used.

STM studies on doped self-assembled monolayer found the apparent height of the doped molecules “blink”<sup>7</sup> when the tip scans over some area repeatedly. The cause of such stochastic switching behavior was still not clear, but recent studies pointed out that it may be caused by changes at molecule-metal interface, such as changes of hybridization of the S-Au bonding<sup>76</sup>, or changes of geometries at the bonding sites<sup>77</sup>. Nevertheless, such stochastic change at the molecule-metal contact causes concerns about the stability of molecule-metal-molecule junctions, because the conductance of the junction can be very sensitive to the changes at the molecule-metal contact.

Houck and co-workers<sup>78</sup> studied charge transport behavior through bare gold break junctions, which were made from electromigration method. It was found that 30% of the junctions that they measured showed Kondo resonance, possibly caused by Au nanoclusters inside the junctions. This discovery raised questions on the

previous results about Kondo resonance which was thought to be caused by the molecule inside the junction. Although it was pointed out that such Kondo resonances in bare junction can be dramatically reduced by briefly applying a high voltage ( $>1V$ ) across the junction, future work on such junctions should be more careful during measurements and data interpretation.

### **1.3 Theory of charge transfer.**

During the past several years, numerous exciting results have been obtained from experiments on molecular devices and researchers have tried to interpret these results with some theories and models. To date, the connection between the theory and experiments is still quite poor, and in most cases the calculated values of the molecular conductance differ largely from the experimental results.

For a typical metal wire, one can easily predict the resistance ( $R$ ) as  $R = \rho \frac{L}{S}$ , where  $R$  is the resistance,  $\rho$  is the resistivity for that metal,  $L$  is the length of the wire and  $S$  is the cross sectional area of the wire. There is no such clear way to predict the resistance of a molecular junction because of the localized nature of most molecular electronic states.

Coherent tunneling (superexchange in some literatures) and incoherent hopping are two possible mechanisms for charge transfer through molecular devices. In the coherent tunneling mechanism, an electron or hole tunnels directly from one part to another (e.g., from one electrode to another, or from donor sites to acceptor sites in molecules), so there is no charge residing on the bridge between the two parts. The quantum tunneling rate constant  $k_{tun}$  depends exponentially on the tunneling distance  $d$ , which can be expressed as

$$k_{tun} = k_0 \exp(-\beta d) \quad (1)$$

where  $\beta$  is the electronic decay constant and  $k_0$  is a constant. If the molecule contains repeated units like methylene groups, this distance dependence equation can be expressed in terms of repeated unit number  $N$  :

$$k_{tun} = k_0 \exp(-\beta_N N) \quad (2)$$

This model agrees very well with the results of alkane thiol and oligophenylene thiol monolayers. People found that the resistance of the monolayer at low bias indeed increases exponentially with the number of methylene or phenylene units and values of  $\beta$  were found to be around  $1 \text{ \AA}^{-1}$  and  $0.42 \text{ \AA}^{-1}$ , respectively<sup>22</sup>.

In the conventional picture of electron tunneling, the probability for an incident electron of energy  $E$  to tunnel through a step barrier of height  $V_0$  and width  $L$  is approximately proportional to  $e^{-\beta L}$ , where  $\beta = 2\sqrt{2m\varphi/\hbar^2}$ ,  $m$  is the mass of electron and  $\varphi = V_0 - E$  is the barrier height. When we apply such a model to a molecular electronics system such as a metal-molecule-metal junction, a first approximation is that the barrier height becomes  $\varphi = E_{LUMO} - E$  for tunneling through the lowest unoccupied molecular orbital (LUMO) or  $\varphi = E - E_{HOMO}$  for tunneling through the highest occupied molecular orbital (HOMO). Once an external bias  $V$  is applied to the two metal leads, the position of incident electron energy relative to the LUMO energy level will change. A qualitative picture is shown in Figure 11. In a symmetric metal (L)-molecule (M)-metal (R) junction, the tunneling barrier, which is the difference between the Fermi level and the molecular LUMO level, is initially  $\varphi$  for electrons from both electrodes. When a voltage  $V$  is applied to the right electrode and

lowers the electron energy levels by  $V$  relative to the left electrode, the LUMO energy level in the molecule will also become lower. The precise shift of LUMO level with applied  $V$  is difficult to predict. If we assume the LUMO energy is lowered by  $\alpha V$ , where  $0 < \alpha < 1$ , the tunneling barrier becomes  $\varphi - \alpha V$ . So the electronic decay constant  $\beta$  is dependent on external bias  $V$ .

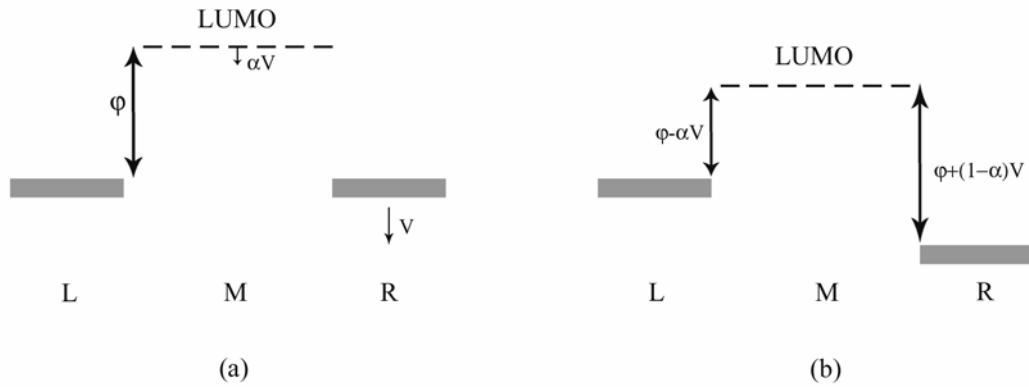


**Figure 11. Energy levels in a metal (L)-molecule (M)-metal (R) model system before (a) and after (b) a bias is applied**

One interesting phenomena, known as resonant tunneling, appears when the molecular LUMO level aligns with the Fermi level of one electrode. This happens in Figure 11 when the tunneling barrier  $\varphi - \alpha V$  approaches 0. The tunneling probability, or the conductance, rises sharply at resonant tunneling bias. In fact, resonant tunneling happens whenever a molecular level aligns with the Fermi level of the electrode. On a conductance-bias plot, resonant tunneling appears as a series of peaks at different biases.

In the incoherent hopping mechanism, the charge resides on the bridge between the electrodes or sites. The charge may be delocalized over the entire bridge or diffuse by hopping. The charge transfer rate  $k_{hop}$  of this diffusive hopping is

inversely proportional to the length of the bridge,  $k_{hop} \propto N^{-1}$ , which makes it look like “Ohmic”.

Both mechanisms may exist in charge transfer through some molecular junction. The competition between these two mechanisms would be affected by the bridge. For shorter molecules, the wave functions of the two electrodes overlap more, thus it is more likely that tunneling will dominate. As tunneling current will drop dramatically with increasing spacing between two electrodes, incoherent hopping may dominate in sufficiently long molecular devices. But even in a long molecule, tunneling may still happen between sites that are close to each other.

To interpret and exploit the experimental data for molecular electronics from all research groups, it is essential to develop a quantitative method for calculating conductance of molecular devices. The main challenge comes from understanding the coupling of individual molecular structures to macroscopic electrodes under nonequilibrium conditions. The energy levels of a characteristic molecule are discrete, with the highest occupied molecular orbital (HOMO) around -9 V. A noble metal, on the contrary, has continuous energy levels near the Fermi level, which is around -5 eV. When a molecule falls into the gap between two electrodes and forms bonds with them, some charge flow, charge rearrangement and conformational changes will occur. The Fermi level of the electrodes will lie somewhere in the HOMO-LUMO gap of the molecule. It is nontrivial to predict the exact position of the Fermi level as it depends on many factors like the electrode material, the electrode geometry etc. Even this picture is oversimplified, as we assume the interaction between the molecule and the electrodes is much weaker than the interatomic interaction in the

molecule which develops molecular energy levels. More strict way should consider the molecule and the electrodes as a whole system.

When a voltage is applied to the two electrodes of a molecular junction, the electrochemical potentials of the electrodes and molecule will shift and current will flow through. According to the Landau formulation<sup>1</sup>, current occurs because electrons are elastically scattered between the two electrodes. We can evaluate the current-voltage (I-V) relationship by the following equation:

$$I(V) = \frac{2e}{h} \int_{-\infty}^{+\infty} dE T(E, V) [f(E - \mu_1) - f(E - \mu_2)] \quad (3)$$

Here  $\mu_1$  and  $\mu_2$  are the electrochemical potentials at the two electrodes,  $f(E)$  is the Fermi function and  $T(E, V)$  is the transmission function. We can write  $\mu_1$  and  $\mu_2$  as  $\mu_1 = E_f - \eta eV$  and  $\mu_2 = E_f + (1 - \eta)eV$ , where  $E_f$  is the Fermi energy and  $\eta$  describes how the potential difference  $V$  is divided between the two contacts.

From the above equation and with some derivation we can get the conductance as:

$$g(V) = \frac{\partial I(V)}{\partial V} \approx \frac{2e^2}{h} [\eta T(\mu_1) + (1 - \eta)T(\mu_2)] \quad (4)$$

and  $g(V) \approx \frac{2e^2}{h} T(E_f + eV)$ , if  $\eta = 0$ .

The conductance may be determined directly by the following expression:

$$g(V) = \frac{2e^2}{h} \sum_{ij} T_{ij}(E, V) = g_0 \sum_{ij} T_{ij}(E, V) \quad (5)$$

Here  $g_0 = 2e^2/h = (12.8 \text{ k}\Omega)^{-1}$ , which is known as the quantum of conductance.

$T_{ij}$  is the probability that a charge will be transmitted from one electrode in state  $i$  to the other electrode in state  $j$ .



The transmission function  $T$  can be influenced by many factors, such as the molecules in the junction, the leads material and geometry, the contact between the molecule and the leads, etc. Some of them are dependent on many uncontrollable experimental factors and stochastic events, which make the results not very reproducible and hard to analyze with theoretical models. But recent computational methods based on nonequilibrium Green's functions (NEGF) combined with density function theory (DFT) have produced some encouraging results.<sup>79-82</sup>

## Chapter 2: Molecular electronics based on a conjugated molecule containing a ferrocene unit: CP-AFM studies.

### 2.1 Introduction

Sita and coworkers proposed that an asymmetric conjugated molecules containing two ferrocene units would behave like diodes<sup>83</sup>. From the electrochemical measurements of model compounds **1** and **2**, it was found that the two ferrocene units showed different reduction and oxidation potentials in compound **2** but not in compound **1** (Figure 12).

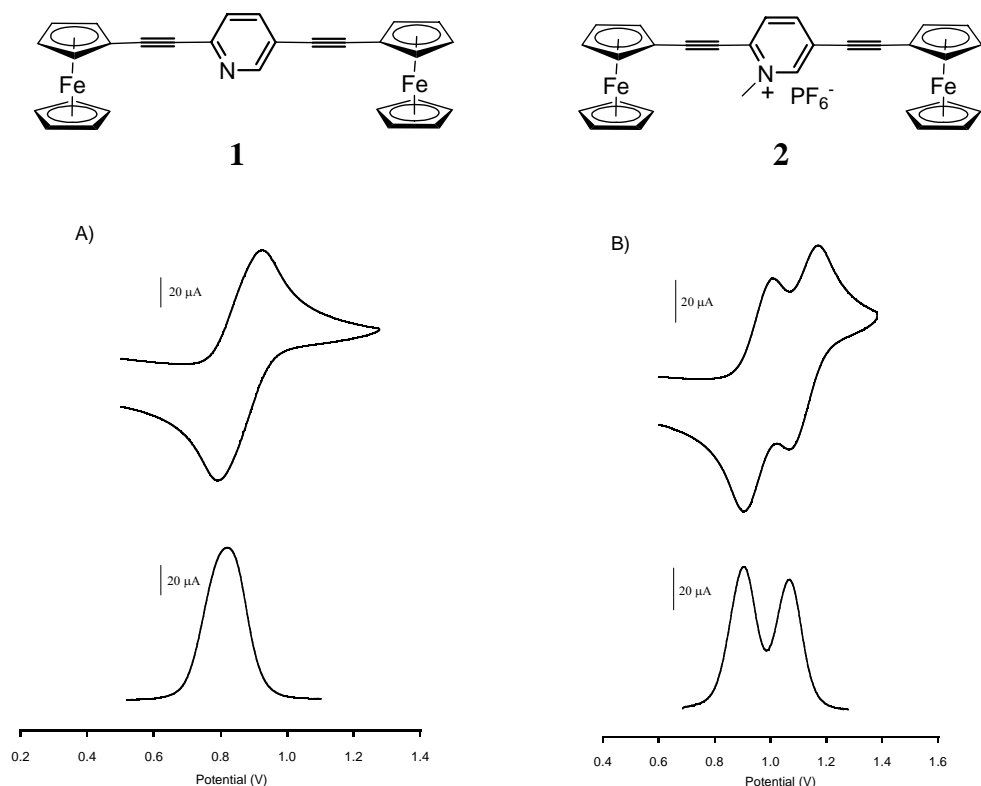
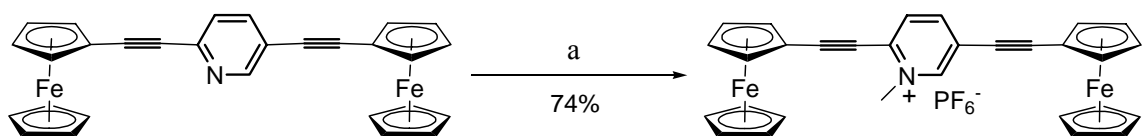


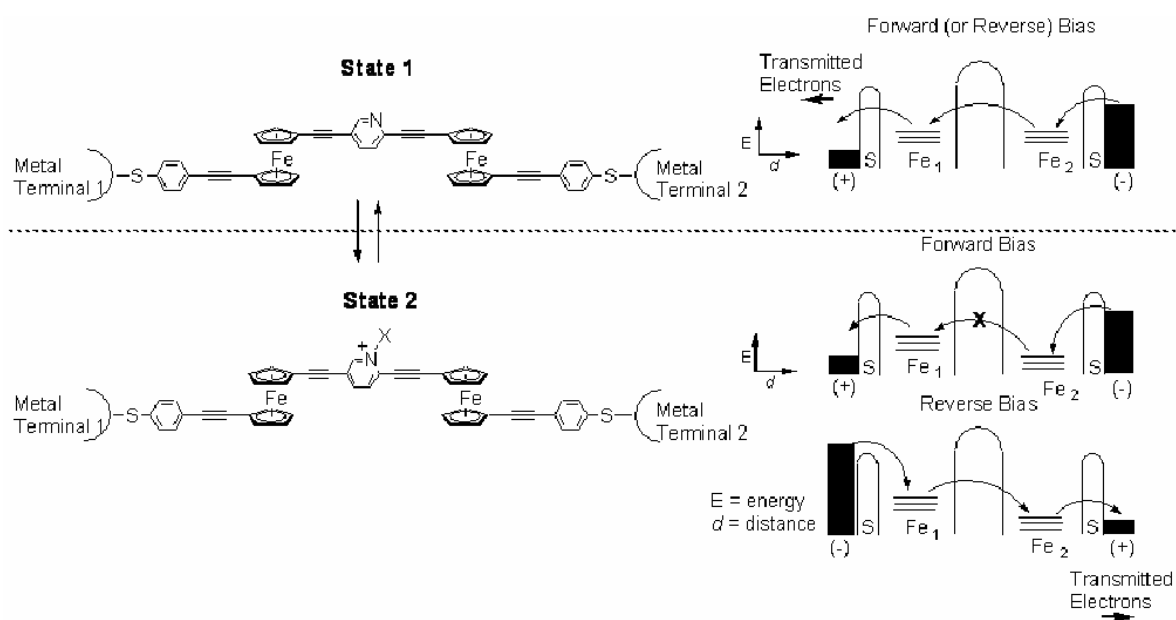
**Figure 12.** Cyclic Voltammogram (CV), scan rate 0.1 V/s (top) and Differential Pulse Voltammogram (DPV) (bottom) for A) **1** and B) **2** in 0.1 M [n-Bu<sub>4</sub>N][B(C<sub>6</sub>F<sub>5</sub>)<sub>4</sub>] in CH<sub>2</sub>Cl<sub>2</sub> using a glassy carbon working electrode. Potentials are referenced to the redox couple of an internal decamethylferrocene standard<sup>83</sup>



<sup>a</sup>Reagents: (a) (i) MeI, CH<sub>2</sub>Cl<sub>2</sub>/CH<sub>3</sub>CN, 50°C, 18 hr. (ii) H<sub>2</sub>O, NH<sub>4</sub>PF<sub>6</sub>.

**Scheme 3.** Synthesis of compound **2** from compound **1**.

Following scheme 1, compound **1** can be easily converted to compound **2**, and the electrical property of the molecule is also changed. If we can incorporate a unit like compound **1** into a molecular junction, we may modify the electrical property of that molecular junction in situ with this chemical modification. With this in mind, the following scheme was proposed<sup>83</sup>:



**Scheme 4.** Molecular representation of a ferrocene-based diode and the proposed schematic describing operation in state 1 and state 2<sup>83</sup>.

First of all, the molecule we would use is quite long. Thus, as we discussed above, we expect electron hopping would be dominant in charge transfer of this

molecular device. As we modify the molecule by turning the neutral pyridine unit into a charged state, we change the energy states of the two ferrocene units. The difference between the ferrocene units energy levels would make the electrons flow easier in one direction than the other, as shown in Scheme 2. In this way, we expect the whole device would behave like a diode.

Considering all the test structures that have been used in molecular devices, we think the CP-AFM technique used by Lindsay and the break junction from electromigration used by McEuen would be suitable for our purposes. Both techniques provide the possibility of measuring current through single molecules.

McEuen and coworkers found the Co atom in the molecule (Figure 9) plays an important role in the electronic property of the whole molecular device. Interesting phenomena like Kondo effect were observed. In our system, we would also like to study the role the ferrocene in the electronic property of the molecular devices. We would study molecules with different number of ferrocene units (Figure 13) and compare their conductances. These molecules have been successfully synthesized by Engtrakul<sup>84</sup>, and their chemical properties have also been carefully characterized.

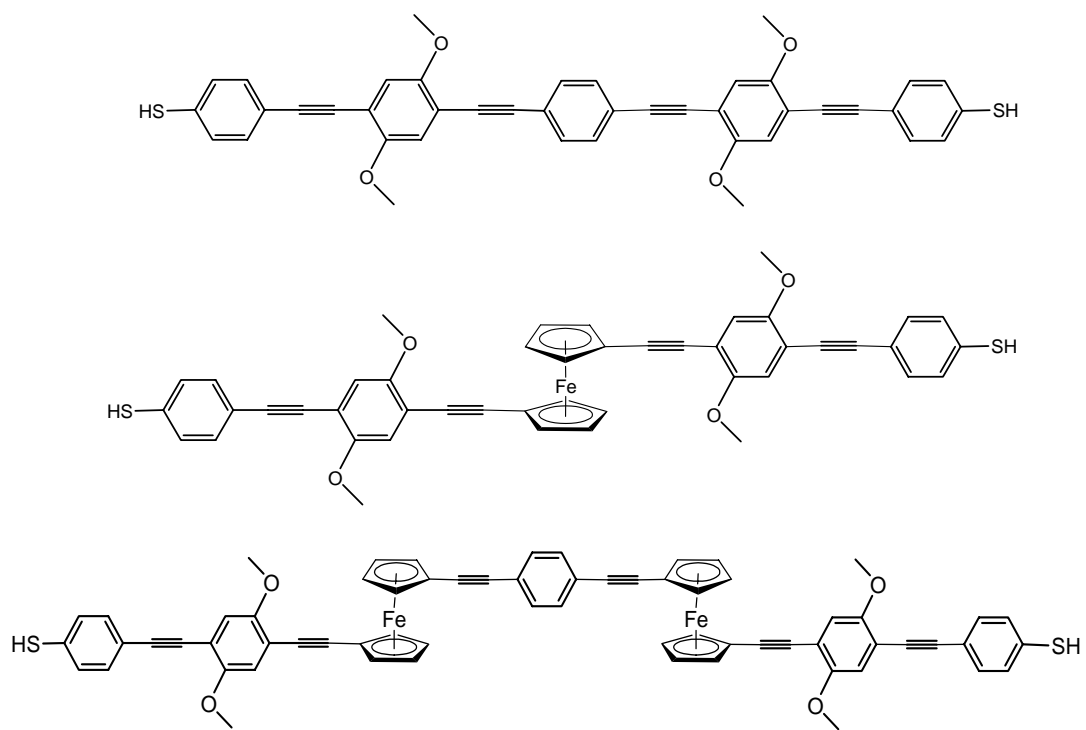


**Figure 13. Similar molecules with different numbers of ferrocene units**

## 2.2 Characterization of SAM and doped SAMs with AFM

### 2.2.1 Introduction of AFM

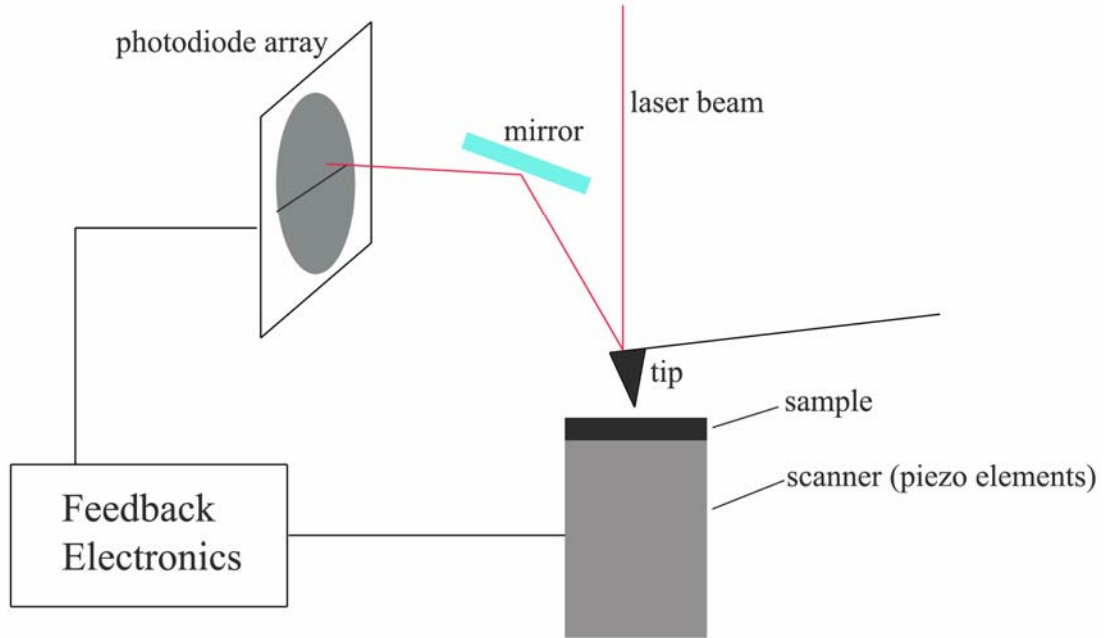


**Figure 14. Illustration of AFM concept**

The concept of Atomic Force Microscope was first proposed by Binnig and co-workers in 1986<sup>85</sup>. The basic idea is shown in Figure 14. A fine tip scans over the sample surface and the force interaction between the tip and the sample is detected and controlled to image the sample surface. Two modes are commonly used for the AFM system in our lab (DI multimode SPM): contact mode and tapping mode. In contact mode, a laser beam is incident on the back of the tip, gets reflected by the tip and a mirror, and projects onto a photodiode array. When the tip approaches the sample surface and makes contact, the cantilever will get bent and change the incident angle of the laser beam. Such change gets magnified after two reflections (by the cantilever and the mirror) and the laser spot on the photodiode array moves accordingly. This change of laser spot position on photodiode indicates the change of

the vertical position of the tip, and thus can be used as feedback signal. When the tip scans on the sample surface in contact mode, the feedback electronics drives the piezoelectric elements to move the sample vertically in accordance to the height change of the sample surface, so that the position of laser spot on photodiode maintains constant. The movement of the piezoelectric elements (scanner) is recorded and plotted to generate the topography of the sample surface.

In contact mode, the tip drags along the surface and certain amount of tip-sample force is needed for feedback electronics to work. Such force may deform the sample surface, and make the sharp tip wear faster. Such effect can be avoided or minimized by the use of tapping mode. In tapping mode, the tip is actuated by a small piezoelectric unit and vibrates freely before approaching the sample. When the tip moves towards the sample surface and senses features on it, the amplitude of its vibration will change and be detected by the photodiode. Similar to the contact mode, the feedback electronics drives the scanner to move the sample to keep the tip vibration amplitude constant. Because the tip contacts the sample surface intermittently, the deformation of the sample surface and tip-sample friction can be much smaller than the contact mode.

AFM can provide sub-angstrom resolution vertically due to (a) the sensitive detection of the tip movement via laser beam reflection and (b) high precision of sample movement by the piezoelectric elements in the scanner. The lateral resolution of AFM is usually limited by the tip size. The tip end radius of normal Si tips is around 20 nm, while sharpened Si tips can give tip radius  $\sim 10$ nm. One promising method of making tips of even smaller tip radius is growing single-walled carbon

nanotube (SWNT) from the conventional Si tip end, because SWNTs have very small radius ( $\sim 2$  nm), high aspect ratio and long lifetime due to their excellent mechanical properties<sup>86-88</sup>. Nevertheless, even with a  $\text{Si}_3\text{N}_4$  tip (typical tip end radius  $\sim 40$  nm), atomic resolution on mica can be achieved in contact mode.

In addition to its high resolution ability, AFM can be performed on virtually all kinds of surfaces, while other microscopes like Scanning Electron Microscope (SEM) and Scanning Tunneling Microscope (STM) require conductive sample surface. AFM can also be conducted in vacuum, ambient and even fluid environments. Since AFM detects the interaction between the tip and sample surface, many properties of the samples, such as elasticity and surface chemical functionality, can be measured.

Before we can measure the conductance of single molecules like those in Figure 13 with the CP-AFM method used by the Lindsay group, a detailed study of the matrix monolayers and the mixed monolayer is necessary.

### **2.2.2 Introduction of self-assembled monolayer (SAM)**

Self-assembled monolayers (SAM) are highly ordered molecular structures formed on solid surface. A SAM film can form on a solid substrate simply by exposing the substrate to an environment which contains surface active molecule species for a certain period of time (Figure 15). The surface active molecules usually have reactive head groups, i.e.  $-\text{SH}$ ,  $-\text{S}-\text{S}-$ , which can form chemical bonds with surface atoms (Au, Ag, Cu, etc.). In molecules like alkanethiols, the Van der Waals interactions between the long linear alkane chains can further stabilize the monolayer and facilitate the formation of SAM. The driving force for the formation of SAM thus is two fold: the chemical bonding between the molecules and the substrate, and the



intermolecular interaction among the molecules. Although studies of monolayers can be traced back to 1920s when Langmuir-Blodgett (L-B) film technique<sup>89,90</sup> was developed, L-B film has a few shortcomings, as compared to SAM. First, it requires special instruments (troughs) to prepare. Second, the driving force for the formation of L-B film is external pressure, so the stability of the L-B monolayers is not as good as SAM once the external pressure is gone because of lacking chemical bonding to the substrate.

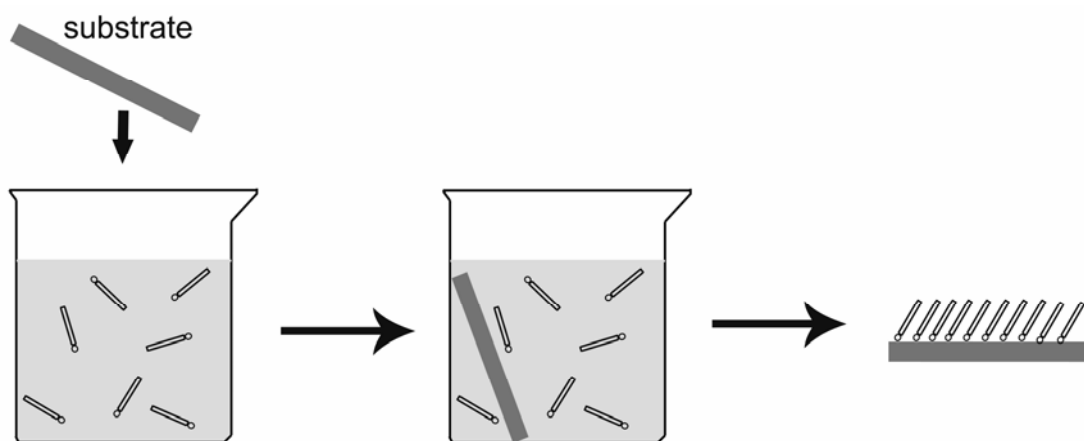


**Figure 15. Illustration of formation of self-assembled monolayer.**

The structure of SAM has been characterized quite thoroughly in the past 20 years<sup>91</sup>. For SAMs from alkanethiols on Au substrate, which is studied most, it is widely accepted that the molecules form highly ordered  $(\sqrt{3} \times \sqrt{3})R30^\circ$  hexagonal structure on the Au surface lattice. This order monolayer structure can change the sample surface property drastically. For example, it can change the surface from hydrophilic (Au surface) to highly hydrophobic (SAM surface).

It is well known that defects like pinholes exist in monolayers. In these defects, the molecules do not bind to the surface well and can be replaced easily by other molecules. Based on this fact, we proposed our idea as in Figure 16.

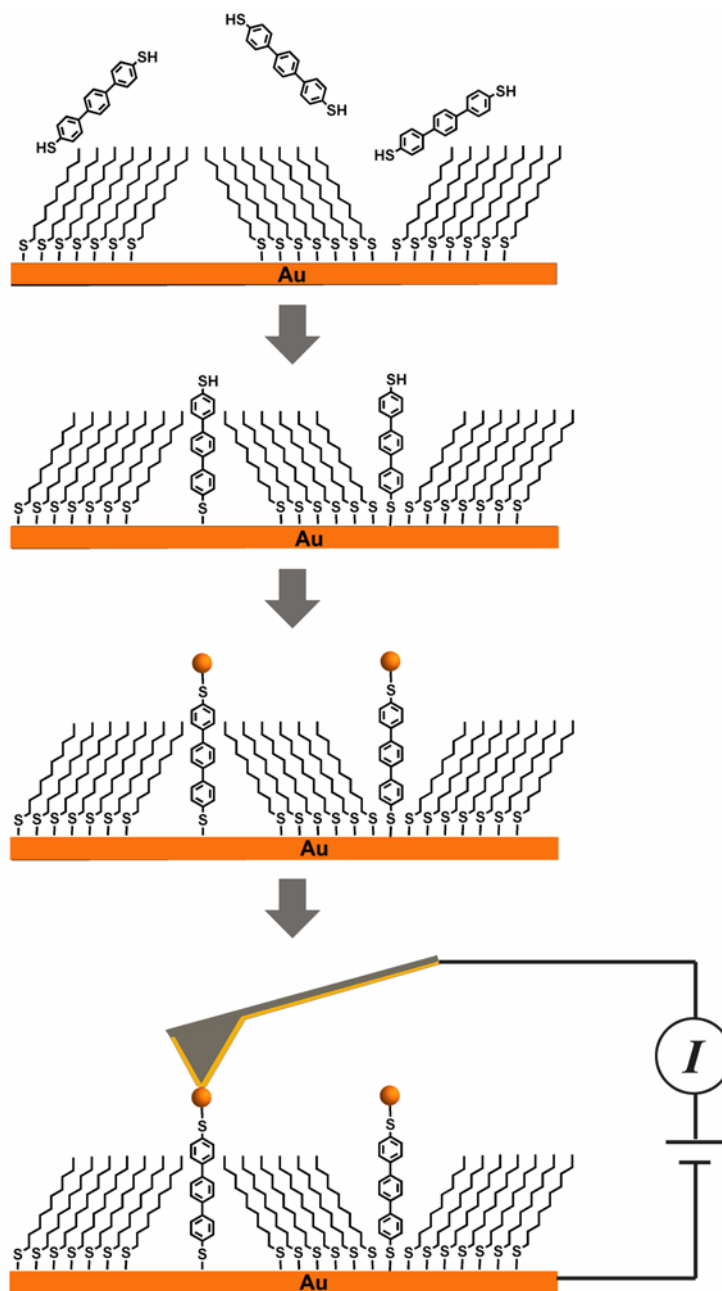


Figure 16. Strategy of conductance measurement of single molecules in a SAM matrix with CP-AFM

Basically we will form a matrix monolayer first from certain alkanethiols, the sample will then be soaked in another solution containing the molecules that we are interested, like the ones in Figure 13, these dithiol molecules should replace some alkanethiol molecules at defect sites and leave thiol groups on the surface. Gold nanoparticle solutions will be used to tether gold nanoparticle to the free thiol group and thus form Au (substrate)-molecule-Au nanoparticle junctions. CP-AFM will be used to attempt to measure the conductance through these junctions.

### **2.2.3 Substrate**

Au film has been the most common substrate since the discovery of SAM. Au is quite inert chemically; it does not oxidize under ambient conditions and it does not react with most chemicals; Au is quite readily available and Au films on various substrates can be made simply by thermal evaporation; Au-S bond is quite strong and thus good monolayers can be formed. All these characteristics make gold popular in SAM and related studies.

We started with Si wafers as substrates for gold films. Si wafers are very flat and are commercially available. The wafers that we used were polished at one side and they had a naturally grown silicon dioxide layer. The interaction between gold and the silicon dioxide layer is not strong enough and thus if gold film is directly deposited onto the wafer surface, the film will be vulnerable to some harsh cleaning process like soaking in the piranha (3:1  $\text{H}_2\text{SO}_4:\text{H}_2\text{O}_2$ , highly oxidative) solution. It is well known that an adhesion layer like thin Cr film between the gold and the  $\text{SiO}_2$  can greatly increase the stability of the Au film. The preparation of the gold substrate is available in the experimental section. Figure 17 shows the change of the surface

morphology when Au/Cr film was deposited onto the Si wafer. Before the deposition, AFM study (Figure 17(a)) showed the SiO<sub>2</sub> surface was very flat, with roughness at 0.108 nm (root mean square value). The surface roughness of Figure 17(b) was 2.192 nm (rms value). Roughness values in the range of 1.5 nm – 2.8 nm was obtained from images of some other Au/Cr coated Si wafer samples. This increase in the surface roughness was simply due to the grainy structure of Au film, which is clearly visible in Figure 17(b). It is well known now that these Au films from thermal evaporation tend to have a dominant (111) surface lattice structure<sup>91</sup>, which enables thiol molecules to form ordered ( $\sqrt{3} \times \sqrt{3}$ )R30° hexagonal structure.

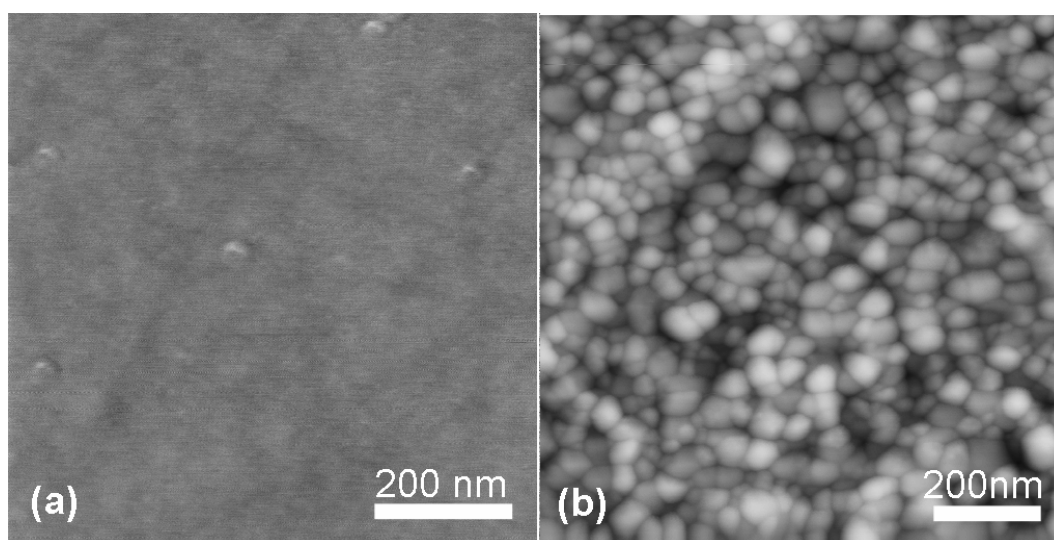


**Figure 17. Surface images of (a) Si wafer (750 nm × 750 nm scan size) and (b) Au film coated Si wafer (1 μm × 1 μm scan size)**

#### **2.2.4 Self-assembled monolayer as the matrix layer**

The Au substrate was stored usually in clean hood and cut into small pieces of around 1 cm × 1 cm or 3 cm × 3 cm. Fresh gold surface is very adsorptive and it adsorbs organic contaminants over time, as well as other particles in the air, thus a thorough cleaning process was carried out to get rid of contaminants (see the

experimental section) before the preparation of self-assembled monolayers. Physisorbed organic molecules and other contaminants from the solution also need to be removed before further characterization and treatment, so careful rinsing was carried out after deposition. Figure 18 shows the surface structure after the Au/Cr/Si sample was soaked in a 1 mM solution of dodecanethiol in ethanol for 24 hours. The surface image looks similar to the bare Au surface in Figure 17(b), with similar surface roughness at 2.137 nm, possibly because the monolayer is so thin (<5 nm) that the change is not noticeable giving the rough nature of the substrate.

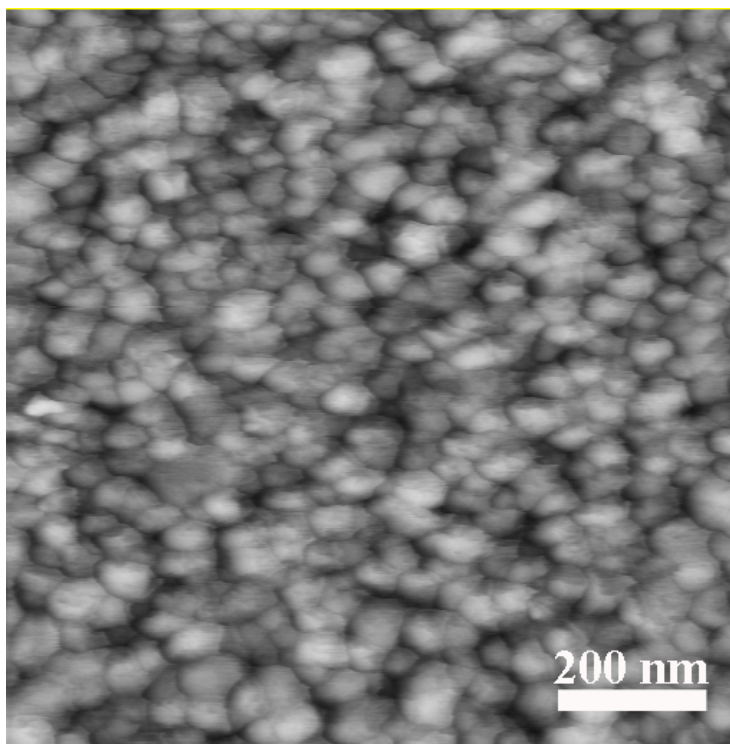


**Figure 18. AFM image of dodecanethiol SAM surface on Au/Cr/Si substrate**

Ellipsometry has proved to be a very convenient way to measure the thickness of thin films. When a beam of polarized light goes through a thin film (SAM in our case) and gets reflected at the interface of the film and the substrate (Au/Cr), the polarization state of the light will be changed by the thin film. The thicker the film,

the bigger the change will be. Table 1 shows the results from dodecane thiol (C10) SAM and hexadecane (C16) thiol SAM.

Sample	Molecules in the SAM	Measured thickness (Å)	Theoretical thickness (Å)
1	Dodecane thiol	$14.6 \pm 0.6$	16.5
2	Dodecane thiol	$12.4 \pm 0.6$	16.5
3	Hexadecane thiol	$15.3 \pm 0.5$	21.2
4	Hexadecane thiol	$16.2 \pm 0.4$	21.2
5	Octadecane thiol	$19.5 \pm 0.5$	23.6

**Table 1. Thickness measurement of the SAMs with ellipsometry**

First of all, the thickness values for the same thiol molecules from different samples are quite close, considering the machine error for the ellipsometer (Gaertner L116C) that we used is  $\sim 3$  Å. Second, the measured thickness for both molecules was lower than theoretical values. The reason can be that the monolayer was not perfect and so the defect density in the SAM may be very high on the grainy gold surface. Because the molecules in these defect sites are not well ordered, the ellipsometry technique tends to give lower value than the theoretically ordered SAM model. Furthermore, early studies by Whitesides and co-workers<sup>92</sup> demonstrated that contaminants on Au substrate was also responsible for the difference between the ellipsometry results and the calculated thicknesses. Nevertheless, these ellipsometry results strongly indicated the existence of the SAM on Au surface.

Electrochemistry can be used to determine the quality of the SAM. The idea is that since alkane thiol is not conductive, a good monolayer of alkanethiol should block the charge transport between the electrolyte and the gold substrate very well. However, the defect site in the SAM can allow charges leak through. Thus, the magnitude of this leaking current qualitatively shows how “good” the SAM is. Figure 19 shows cyclic voltammograms from a C16 alkanethiol SAM in a solution containing 1 M KCl and 1 mM  $\text{K}_3\text{Fe}(\text{CN})_6$ .

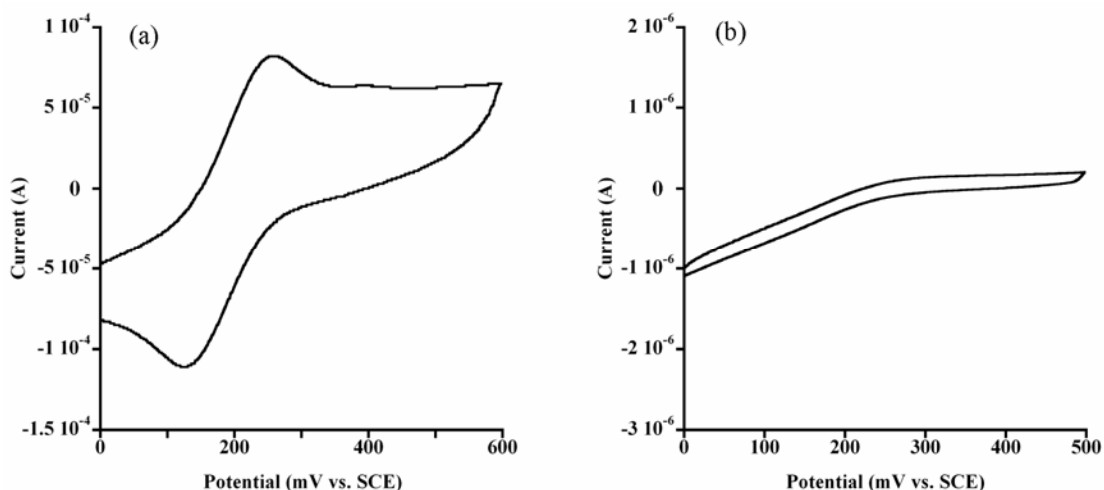


**Figure 19. Cyclic Voltammogram of (a) bare gold surface, (b) SAM of hexadecanethiol on Au in 1 M KCl containing 1 mM  $\text{K}_3\text{Fe}(\text{CN})_6$ .**

The cyclic voltammogram of bare gold surface (Figure 19(a)) shows the reduction and oxidation peaks typically seen in this redox couple on a metal electrode. However, these peaks were not observed on the gold electrode covered with a SAM of hexadecanethiol. Furthermore, the charging current on SAM/Au electrode was significantly smaller compared to the bare gold electrode. These results confirmed that the existence of SAM efficiently blocks charge transfer between the metal electrode and the electrolyte.

In short, although AFM study didn't give convincing evidence of SAM formation on Au surface, partially due to the substrate roughness, the results from ellipsometry and electrochemistry strongly supported the existence of SAM on Au electrode. Further characterization of the crystalline nature of the SAM structure requires other surface techniques like scanning tunneling microscope.

### **2.2.5 Au nanoparticles**

Au nanoparticles with different diameters have been synthesized and studied for quite a long time. One interesting property of Au nanoparticles in solution is that they display different colors according to their sizes. This phenomenon is caused by the surface plasmon absorption of these Au nanoparticles. In our study, Au nanoparticles were used to form Au (substrate)-molecule-Au nanoparticle junction. Considering the hydrophobic property of the sample surface due to the alkanethiol SAM, we prefer that the Au nanoparticles can be dissolved in organic solvent.

Frens<sup>93</sup> successfully made gold nanoparticles with diameters larger than 15 nm by reducing  $\text{HAuCl}_4$  with the presence of sodium citrate in an aqueous solution upon boiling. The citrate acts as both reduction agent and protection ligand for the nanoparticles. The diameter of the gold nanoparticle was controlled by varying the ratio of sodium citrate vs.  $\text{HAuCl}_4$ . Following the same method, Hirai and co-workers<sup>94</sup> developed a method to transfer the gold nanoparticles from the aqueous phase into an organic phase (i.e. n-hexane or cyclohexane). Their results showed the colloidal gold in the organic phase was stable, and TEM images revealed that the size and size distribution of the gold nanoparticles were not affected by the phase transfer process. We adopted the same approach to make gold nanoparticles in hexane. The



detailed procedure can be found in the experimental section. Figure 20 shows TEM images of thus made gold nanoparticles. The average size of the nanoparticles was  $15.2 \pm 1.3$  nm.

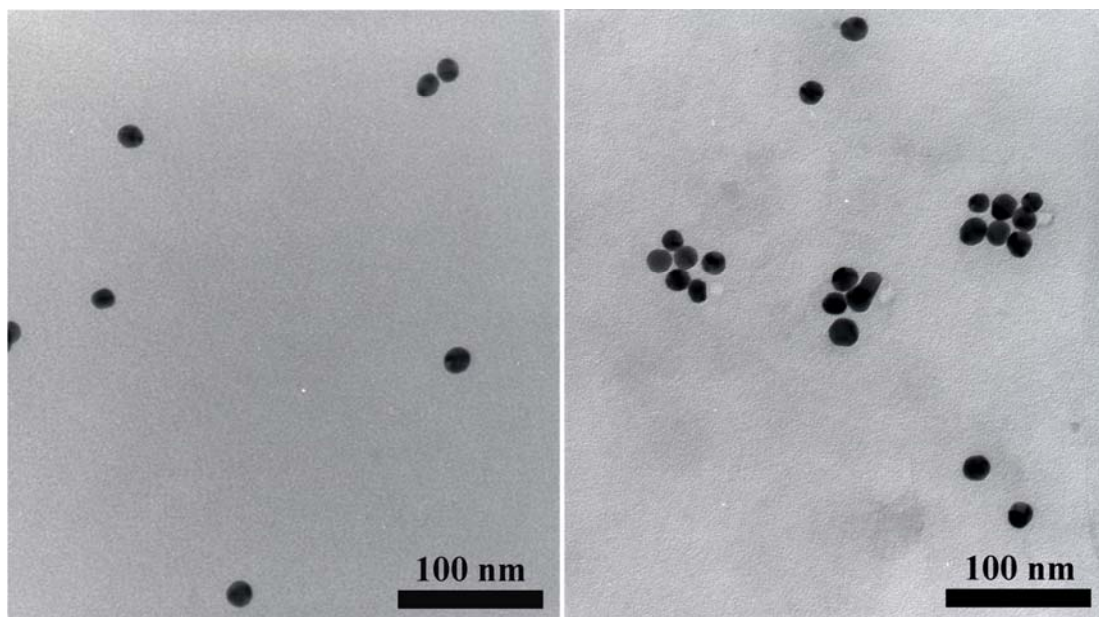


**Figure 20. TEM images of Au nanoparticles.**

### **2.2.6 Au (substrate)-molecule-Au nanoparticle junctions characterized by AFM**

Following the strategies illustrated in Figure 16, we attempted to fabricate Au (substrate)-molecule-Au nanoparticle junction with alkanedithiol molecules doped into an alkanethiol matrix SAM. We started with alkanedithiol molecules because they are readily available, and such experiments would give us first-hand experience in fabricating such molecular heterojunctions, which would be very helpful once we need to study our own conjugated molecules (Figure 13).

Figure 21 shows surface images of a sample which was prepared following the method depicted in Figure 16. In this case we doped hexadecanedithiol(HDT) molecules into decanethiol SAM, followed by tethering gold nanoparticles with the HDT molecules in a gold colloid solution. From the AFM height image (left), the gold nanoparticles, with diameters around 15 nm from TEM study, couldn't be discerned easily, which is mainly due to the rough background. The section analysis in Figure 22 also agrees with our judgment. Furthermore, the rough background prevents us from measuring the actual height of the particles with section analysis.

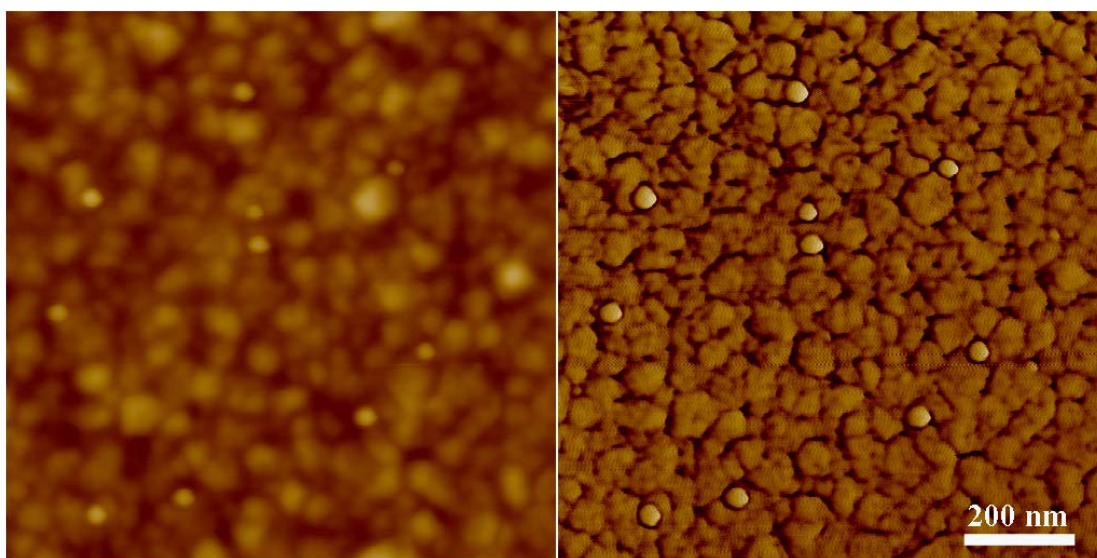


**Figure 21. AFM surface image of gold nanoparticles tethered on hexadecanedithiol in a dodecanethiol SAM, left: height image, right: phase image.**

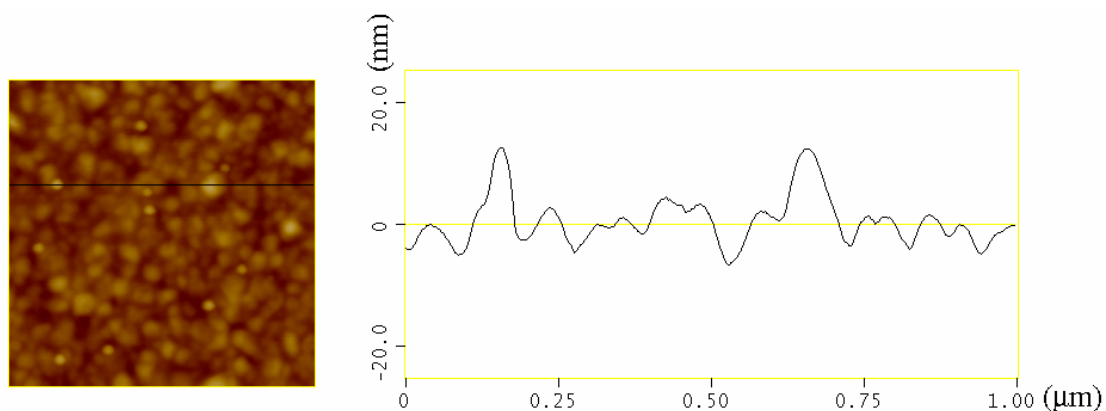


**Figure 22. Section analysis on the AFM height image in Figure 21.**

Despite the difficulties we had in analysis of the AFM height image, the phase image gave good contrast between the gold nanoparticles and the background, where the gold particles appeared to be bright spots on the surface. This is because the phase image was determined by the interactions between the surface features and the tip. Although we don't have convincing evidence, we suppose the protective ligand layer, which was on the gold nanoparticles initially in the colloid, was completely or mostly removed by the rinsing process during sample preparation. Thus in our case, the contrast difference in the phase map comes from difference between the tip-gold nanoparticle and tip-SAM covered Au substrate interaction.

The apparent lateral dimensions of the nanoparticles could be obtained from the phase image in Figure 21. The results were in the range of 35-45 nm, which were much larger than the results from TEM images. The main reason for this difference is the tip convolution, which is due to the finite radius of the tip. Figure 23 illustrates a case when an AFM tip scans over a particle, the apparent size of the particle (dashed line) will appear larger than its actual size. However, if there is no deformation of the

particle during the scanning process, the height of the particle is still accurate on the AFM image.

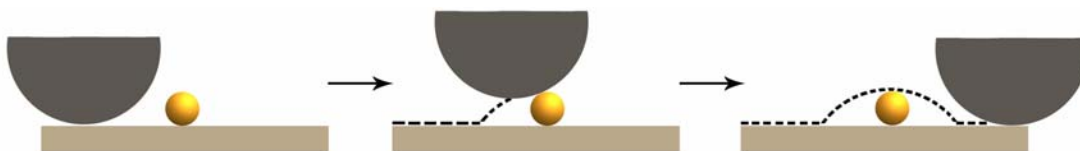


**Figure 23. Illustration of AFM tip convolution which makes small features appear larger in image**

In short, these results demonstrated AFM is an excellent tool to characterize such Au (substrate)-molecule-Au nanoparticle junctions embedded in a SAM. However, a few improvements can be made here. First, a substrate with flatter surface would greatly improve the contrast between the Au nanoparticles and the substrate in the AFM height image. Au film on mica would be a good candidate for this purpose. It is well known that once annealed, the surface of gold film on mica consists of large atomically flat terraces. On the other hand, the current substrate, gold film on Si, has roughness around 2-3 nm, due to the grainy structure of gold that formed during the evaporation process. Second, the size of nanoparticle that we use here ( $\sim 15$  nm in diameter) is quite large, considering the molecule-molecule distance in ordered  $(\sqrt{3} \times \sqrt{3})R30^\circ$  hexagonal structure of SAM is only  $\sim 5$  Å. Even though the dithiol molecules were doped into an alkanethiol SAM and their density on the surface could be quite low, such a big particle still has great possibility to tether with multiple dithiol molecules. As we want to study the relations between the molecular structure and the electronic property, we prefer junctions from single molecules. If a junction contains multiple molecules, any data collected from it will come from the ensemble and properties from single molecule may be averaged out or covered up. The use of

much smaller gold nanoparticles, with diameter in the range of 1-2 nm, will significantly reduce possibilities of formation of junctions from multiple molecules. However, imaging such small particles on the rough surface of Au film on Si will become extremely difficult. And thus again, a more flat substrate is required.

Another important question is whether or not the nanoparticles are all tethered to dithiol molecules. Although the sample underwent careful rinsing during preparation, there was still possible physisorption of nanoparticles on the surface. Moreover, whether or not there are still exposed dithiol molecules on the surface is also questionable. Both cases will complex the future measurement of the electronic characteristics of the junctions. One possible solution would be Scanning Tunneling Microscope (STM), due to its atomic resolution capability.

### **2.3 Characterization of SAM and doped SAMs with STM**

#### **2.3.1 Introduction of STM**

Since its invention at 1982 by Binnig *et al.*<sup>95</sup>, Scanning Tunneling Microscopy (STM) has proved to be a powerful method in characterizing surface features as well as manipulating atoms and molecules at sub-angstrom resolution.

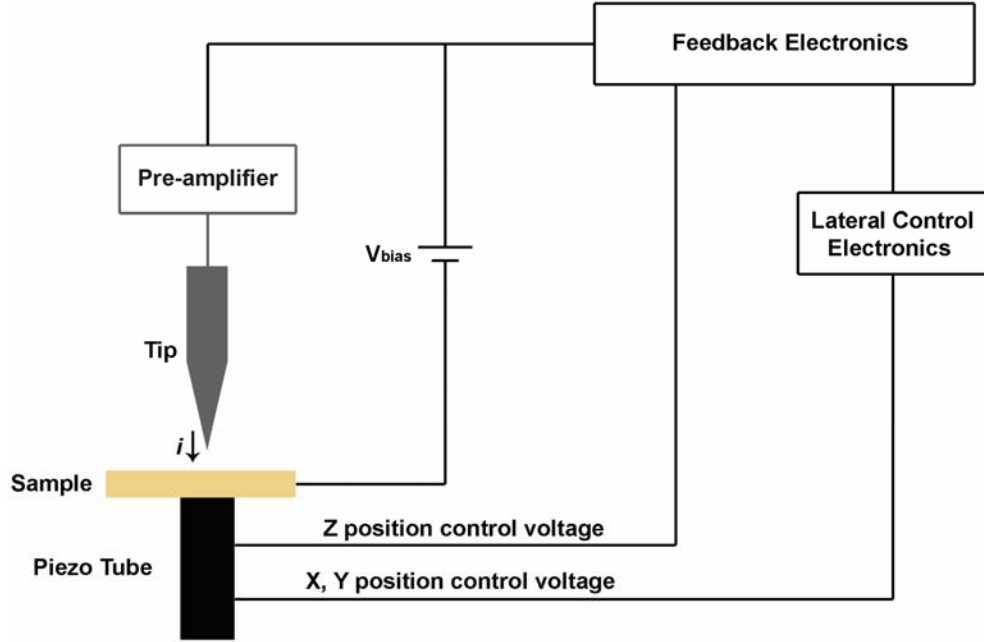


Figure 24. Basic concept of scanning tunneling microscope.

The basic concept of STM is demonstrated in Figure 24. A metal tip, usually made from Pt/Ir or W, is brought close to the sample surface. The tip is biased relative to the sample. When the distance between the tip and the sample is small enough, current can tunnel directly from the tip end to the sample, or vice versa, because of quantum tunneling effect. The gap between the tip and the sample surface serves as a barrier that will prevent electron from flowing through, but if this barrier is thin enough, the electron can tunnel through it. The tunneling current strongly depends on the tip-sample distance as

$$I \propto \exp(-As\phi^{1/2}),$$

where  $A = (4\pi/h)(2m)^{1/2} = 1.025 \text{ \AA}^{-1} \text{ eV}^{-1/2}$  with  $m$  the free-electron mass,  $s$  the tip-sample distance,  $\phi$  the tunneling barrier height between the tip and the sample surface. Note that the current decreases exponentially as tip-sample distance increases. In

particular, with barrier heights of a few eV, a 1 Å increase in tip-sample distance will result in an increase of the tunneling current by around one order of magnitude. It is this high sensitivity in tip-sample distance that enables STM to achieve atomic resolution.

An STM can operate under “constant current mode” or “constant height mode”. In constant current mode, the feedback electronics keeps the tunneling current constant with a constant bias between the tip and the sample. The piezoelectric elements adjust the sample position (or the tip position in some STMs if the piezoelectric elements are connected with the tip instead of the sample) actively to keep the tip-sample distance constant in order to achieve constant current. The change in sample position ( $x, y, z$ ) is recorded to generate the surface image. On the other hand, in constant height mode, the piezoelectric elements move the sample only laterally (in  $x, y$  direction but not in  $z$  direction). As the tip scans over the sample surface, any change in tip-sample distance will cause large change in tunneling current, and such current changes are recorded to generate images. Since the tip needs to be kept close to the sample surface ( $<2$  nm usually) for tunneling to occur, constant height mode is only used on very flat surfaces. Constant current mode, however, can be used on quite rough surface due to the active  $z$  direction feedback control.

### **2.3.2 STM tips**

Tips play an important role in a STM system. The final STM image contains contribution from both the sample surface structure and the tip geometry. Furthermore, any contamination on the tip will complicate or prevent tunneling.

Mechanically cut W or Pt/Ir tips are widely used in STM under high or ultra high vacuum, because of the ease of fabrication. But mechanically cut tips have their own drawbacks. First, it has been proved that mechanically cut tips usually have multiple “mini-tips” at the tip end<sup>96</sup>. Thus these tips will cause artifacts on a rough surface, although they will still work fine on a flat surface. Figure 25 illustrated an imaginary tip with 2 mini-tips scanning on the different surfaces. When such a tip is used on a flat surface, as showed in Figure 25(a), the tunneling current will mainly come from mini-tip 1 because of the high sensitivity of tunneling current on tip-sample separation. In fact, such kind of tip, with one atom protrudes at the tip end, can often be achieved by mechanically cutting. But when the same tip is used on a rough surface, as illustrated in Figure 25(b), mini-tip 2 may dominate the tunneling when it comes close to a high feature (step edge) on the surface. In this particular case, the step edge on the sample surface will be imaged twice by mini-tip 1 and 2, and such artifacts will be shown on the STM images.

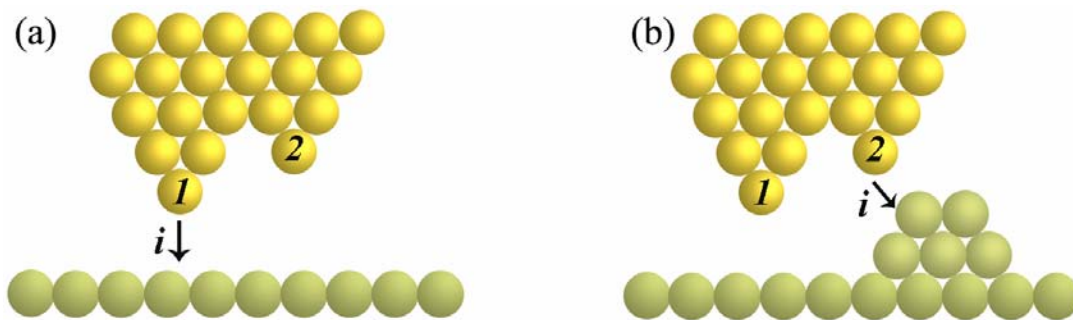


**Figure 25. Illustration of an STM tip, which has two "minitips", scanning over sample surface. (a) On a smooth surface, the tunneling current mainly comes from minitip 1, (b) Minitip 2 may cause artifacts when the surface is not smooth.**

The second drawback of mechanically cut tips is the poor reproducibility. Figure 26 shows SEM images of two mechanically cut tips that we prepared in our



lab. It is impossible to make tips with similar tip radius, aspect ratio and symmetry with this method.

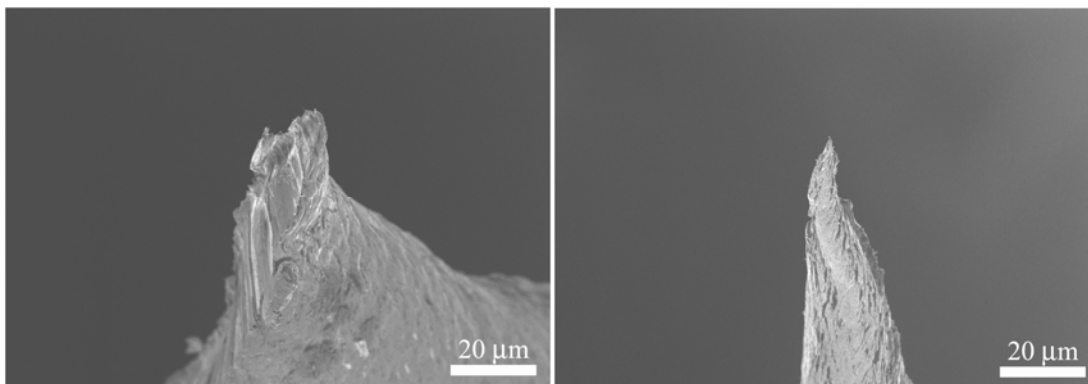


**Figure 26. SEM images of two mechanically cut STM tips**

In our system, we want to visualize the conjugated molecules or Au nanoparticles, which will protrude from the supporting matrix monolayer. We tried to avoid the use of mechanically cut tips due to the above reasons. Electrochemically etched tips came into our sight as they can be made reproducibly with controllable shape<sup>96-98</sup> and such tips are also commercially available. However, the storage of these tips can be problematic because the sharp tip readily absorbs contaminants. In fact, our experience with these commercially available STM tips was not very satisfactory. Further SEM study (Figure 27) also revealed these tips could be heavily contaminated once stored under ambient conditions for a few months.

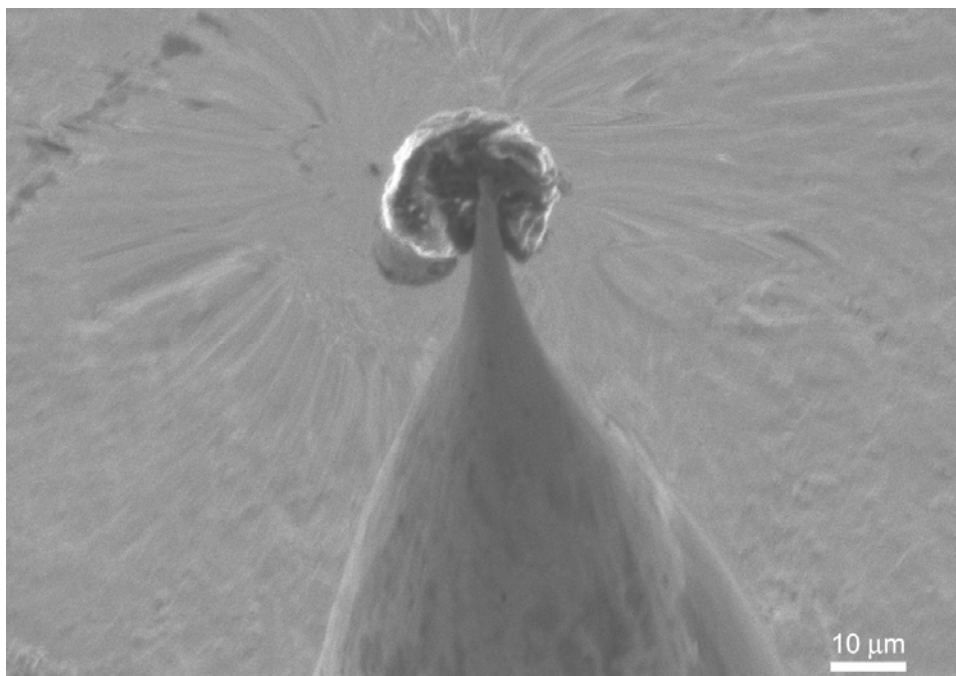


**Figure 27. SEM image of a heavily contaminated STM tip.**

Based on these unsuccessful experience with the mechanically cut tips and the commercially available STM tips, we decided to make our own tips with the electrochemical etching method. A three-step method was developed by Lindahl and co-workers<sup>96</sup> to make sharp STM tips (typical tip radius around 20 Å) with residual oxide layer similar to mechanically cut tips in thickness. We modified this method slightly (details can be found in experimental section) and it proved quite successful. Figure 28 shows SEM images of an electrochemically etched tip. The magnified image of the tip end (right image) demonstrates the tip end radius is smaller than 20 nm. We can't determine the exact tip end radius due to the limited resolution of SEM. Furthermore, the SEM images also showed that the tip has well defined shape, as well as high aspect ratio.

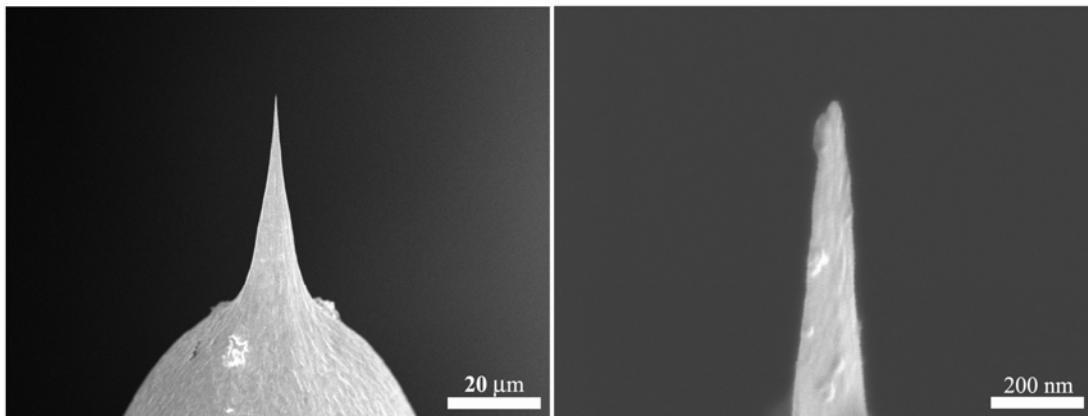


**Figure 28. SEM images of an electrochemically etched STM tip.**

These tips were first tested on Highly Ordered Pyrolytic Graphite (HOPG), which is a common standard for STM and readily available. HOPG has a layered structure; with each layer composed of a planar arrangement of fused hexagonal benzene rings. The layers are bonded to each other by weak Van der Waals interactions. A fresh surface of HOPG, with large atomically flat terraces, can be achieved simply by peeling off the top layer with scotch tapes. Figure 29 was STM images of HOPG obtained with one electrochemically etched tip. The image was filtered to get rid of high frequency noises and make periodic patterns more obvious. Atomic resolution could be achieved as the hexagonal arrangements of C atoms were clearly visible. The inset shows the hexagonal 2D spectrum and the C-C spacing on the image was determined to be around 2.5 Å, which is close to the expected value of 2.46 Å. As our STM system (Multimode SPM, DI, in STM mode) was operated under ambient conditions and we didn't have precise temperature control, thermal drift can affect the final images quite a bit. And indeed, further studies on HOPG with electrochemically etched tips revealed that often the hexagonal pattern of C atoms was not very symmetric and the patterns were either compressed or extended in x or y

direction. The C-C distance value from the 2-D spectrum varies from 2.2 to 2.8 Å. One can minimize the effect of thermal drift by letting the system stabilize over time, but such measure was found to have limited effect in our case as the system will warm up after being used for certain time.

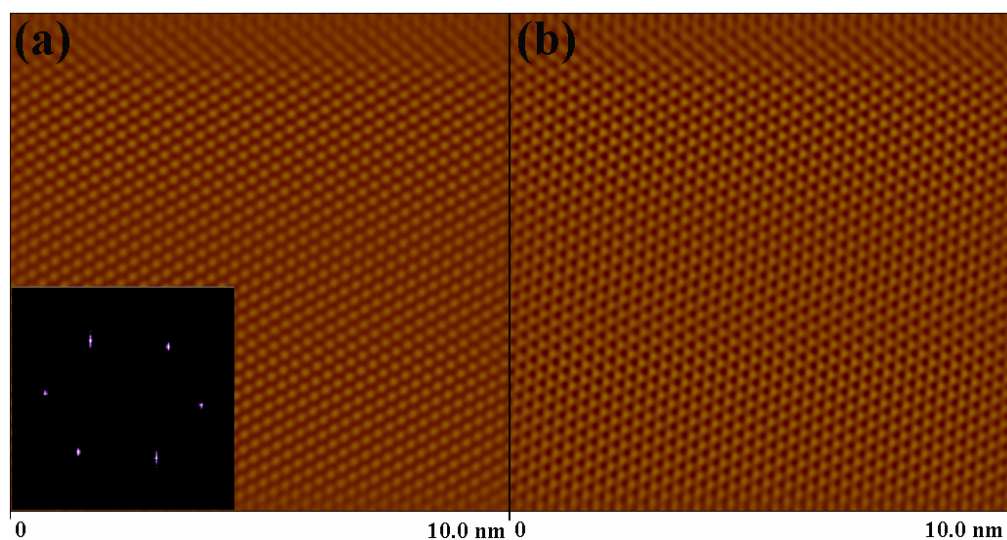


**Figure 29.** STM images of HOPG with an electrochemically etched tip. (a) height image, (b) current image, inset is 2d spectrum of the height image

Nevertheless, these tests of the electrochemically etched tips on HOPG demonstrated that these tips can be used in STM to achieve atomic resolution. And thus they can be potentially useful for STM studies on pure or doped SAMs.

### **2.3.3 Characterization of pure and doped SAMs with STM.**

#### **2.3.3.1 STM on pure SAMs**

Due to the insulating nature of the alkyl chains in alkanethiol molecules, it is generally accepted that STM must work under low tunneling current condition in order to obtain ordered structure of alkanethiol SAMs. When a tip scans above a SAM surface under vacuum, the tunneling occurs between the tip and the gold

substrate. Weiss *et al.*<sup>99</sup> proposed a two-layer tunnel junction model to explain the electron transfer during STM imaging. In this model (Figure 30), the tunneling path consists of two distinct layers: the vacuum gap and the self-assembled monolayer. Each layer has its own transconductance ( $G$ ) and  $G$  is dependent on the thickness of the layer, which can be expressed by

$$G_{gap} = A e^{-\alpha h_{gap}} \quad (6)$$

$$G_{SAM} = B e^{-\beta h_{SAM}} \quad (7)$$

where  $G_{gap}$  and  $G_{SAM}$  are the transconductance for the vacuum gap and the SAM,  $A$  and  $B$  are prefactors,  $\alpha$  and  $\beta$  are decay constants,  $h_{gap}$  and  $h_{SAM}$  are the respective layer thicknesses.

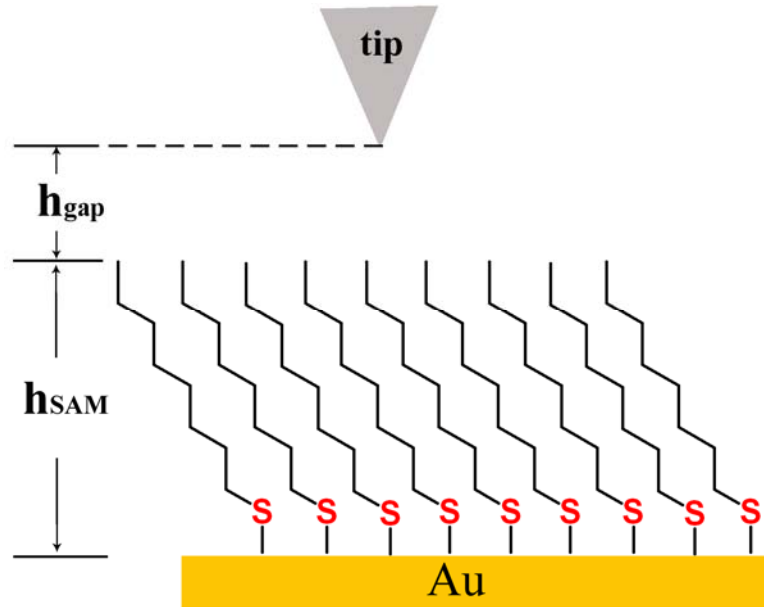


**Figure 30. Illustration of the two-layer tunnel junction model**

Because the transconductance reflects the probability of an electron tunneling through the layer, the total transconductance ( $G_{total}$ ) is the product of the transconductances of the two individual layers,  $G_{total} = G_{gap} G_{SAM}$ .

Figure 31 is a STM topography image obtained on dodecanethiol self-assembled monolayer with one electrochemically etched tip. The image was obtained with tip bias at -1.0 V and tunneling current at 100 pA. The monolayer consists of domains of ordered structure, with defect sites around the domain boundaries. The  $(\sqrt{3} \times \sqrt{3})R30^\circ$  structure was clearly visible on each domain, and the inset 2D spectrum shows the hexagonal periodicity. The closest molecule-molecule spacing ranges from 5.0 to 7.0 nm, which is close to the expected value 4.98 Å, and we believe the difference is from thermal drifting. We couldn't resolve any ordered structure in the defect areas. There are most likely molecules in these defect areas, as the section analysis shows the apparent height difference between the feature inside the defect area and the ordered SAM domain is usually smaller than a few Å. This value is much smaller than the physical height of the dodecanethiol monolayer, which is 16.5 Å.

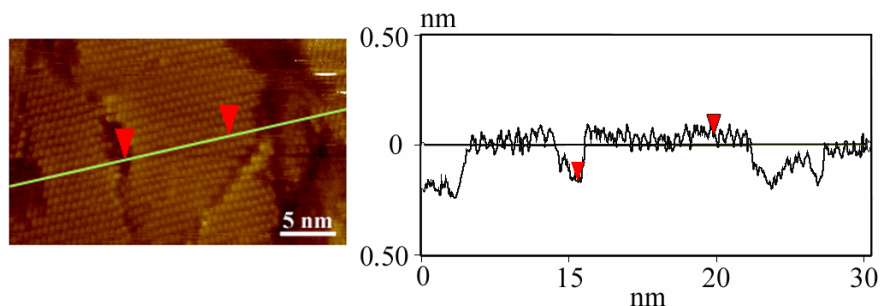
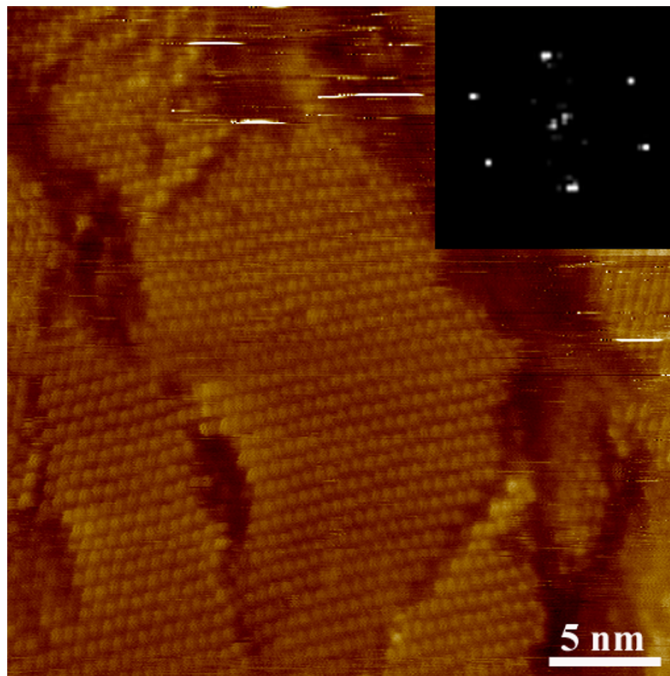


**Figure 31.** (top) STM image of dodecanethiol SAM on Au. Inset is the 2D spectrum of the terrace in the middle of the image; (down) section analysis of the height image.

A recent review paper from Whitesides group<sup>91</sup> talked about different kinds of defects that can exist in SAMs. The defects can result from both intrinsic and extrinsic causes. The extrinsic factors can be contaminants on the substrate surface, purity of the thiol solution, impurity atoms in the substrate, and step edges on the surface. Intrinsic causes may stem from the dynamic process during the SAM formation. One characteristic kind of defect is monatomic vacancy<sup>100</sup>, which on the STM images shows as pit-like defects with depth around 2.4 Å, the monatomic step height of the Au (111) surface. It was proposed that these vacancies come from the

relaxation of the herringbone reconstruction on Au surface, which creates vacancies in the top gold substrate layer and small vacancies may nucleate into larger ones. Furthermore, it is well known that the formation of SAM is a dynamic process, which is accompanied by formation of different phases. Although the  $(\sqrt{3} \times \sqrt{3})R30^\circ$  structure is the most common phase observed on alkanethiol monolayers, other phases also exist under different conditions. For example, Poirier and co-workers studied phase transitions during the alkanethiol monolayer formation on gold substrate with variable-temperature scanning tunneling microscopy (VT-STM)<sup>101-104</sup>. Their study with decanethiol molecules revealed that as the coverage of decanethiol molecules on the Au substrate increases, the first two ordered phases that appeared were striped phases. Further increase of coverage resulted in a liquid (melt) phase and then the final close-packed saturation phase. STM can't identify single molecules in the liquid phase and it is believed that molecules in liquid phase diffuse at high speed. The VT-STM study showed that different phases can coexist and a phase diagram was made based on experimental data.

In our case, some defects in the STM image in Figure 31 appear to be monatomic vacancy, as the section analysis showed the depth of these defects was around 2.5 Å. In other pit-like defects, the bottom seemed not flat and showed irregular morphology based on the section analysis, so these defects may be liquid phase or defects that formed from extrinsic causes.

### **2.3.3.2 STM on doped SAMs**

Defects in SAM reduce the integrity of the monolayer, decrease the mechanical strength, and even reduce the chemical stability of the monolayer. Poirier *et al*<sup>105</sup>



studied the reaction of ozone with decanethiol monolayer on Au(111) with STM and XPS, and it was found that the oxidation reaction initiated at the domain boundaries where defects usually resides.

On the other hand, the existence of defects can be used to our advantage in doping other molecules into a matrix monolayer. It was reported that the replacement of short chains by long chains takes place near the domain boundary<sup>106</sup>. Compared with the ordered crystalline domains, the defect sites usually have lower molecule density and less steric hindrance so that alien molecules from the solution may penetrate and replace molecules in these sites. Thus a strategy depicted in Figure 16 can be used to introduce individual molecules of interest into a preformed SAM, such as the commonly used alkanethiolate monolayer.

Researchers have tried other strategies to make similar heterogeneous monolayers. Chen and co-workers<sup>107</sup> studied the structure of mixed self-assembled monolayers formed by coadsorption from a solution containing asymmetric disulfide  $\text{HO}(\text{CH}_2)_{11}\text{S}-\text{S}(\text{CH}_2)_{11}\text{OH}$  and asymmetric disulfide  $\text{HO}(\text{CH}_2)_{11}\text{S}-\text{S}(\text{CH}_2)_{17}\text{CH}_3$ . Their atomic force/friction force microscopy (AFM/MFM) images showed no phase segregation and crystalline lattice image could be obtained. Noh and Hara<sup>108</sup> monitored the adsorption process of pure  $\text{HO}(\text{CH}_2)_{11}\text{S}-\text{S}(\text{CH}_2)_{17}\text{CH}_3$  molecules onto Au surface with STM. The STM images clearly showed that during the early SAM growth stage, two phase-separated domains with different periodicities could be observed. Kelly *et al.*<sup>109</sup> also used STM to study monolayers formed from asymmetric disulfide  $\text{CH}_3(\text{CH}_2)_n\text{S}-\text{S}(\text{CH}_2)_{n+1}\text{NC}_{60}$  ( $n=5$  or  $10$ ,  $\text{C}_{60}$ =fullerene), and the STM image exhibited high coverage of fullerene without phase-segregation.

Besides the method of forming heterogeneous monolayers from asymmetric disulfides, it was also proposed to form such monolayers from mixed solution containing two different thiol molecules. Chen and co-workers<sup>106</sup> studied monolayers from mixed solutions of alkanethiols of different chain lengths. It was found that when prepared at room temperature the mixed SAMs exhibited phase segregation if the difference of the chain lengths of the two alkanethiol molecules is greater than 4 carbon atoms, while mixed monolayer prepared at 50°C from octanethiol/tetradecanethiol (chain length difference =6 carbon atoms) mixed solution didn't show phase segregation. The authors believed that phase segregation was a kinetically controlled process. When the temperature was low, the formation of ordered domains was slower and the size of the domains was much smaller than those formed at higher temperature. Thus at the early stage of SAM formation, a lot of defects exist at domain boundaries, where the steric hindrance is low and the short chain molecules at these sites can be replaced by long chain molecules. The driving force for molecule exchange is determined by van der Waals interaction between molecule chains, and the general order of favorability of chain pairs is long-long > short-short > long-short. So at low temperature, the long chain molecules will accumulate near the defect sites by molecule exchange, leading to phase segregation. Cygan *et al.*<sup>43</sup> studied the possibility of making mixed monolayer of alkanethiolate and certain phenylene-ethynylene oligomer from mixed solution of the two molecules. The STM images didn't show any ordered structure, and it was believed that the phenylene-ethynylene oligomer molecules disturbed the ordering process of the alkanethiolates. On the other hand, the same investigators tried the insertion method

(Figure 16) and it turned out to be quite successful. The phenylene-ethynylene oligomer molecules were found to be in or near the defect sites, and the crystalline lattice of the alkanethiolate domains can be resolved.

Considering the molecules that we are interested (Figure 13) also contain phenylene-ethynylene backbones, we believe the insertion method is the most promising one based on the reported results. The preparation of the sample is quite straightforward. (see experimental section) The STM experiments were conducted in a glove box filled with nitrogen to minimize the formation of water film on the surface. The STM was in constant current mode with tip bias at -1.0V and current set point at 1 pA. Figure 32 shows a STM image of dodecanethiol SAM with inserted ferrocene oligophenylethynyl dithiol (Fc-OPE) molecules. The first thing we noticed was some bright spots scattered on the surface. We assign these spots as Fc-OPE molecules, as they were absent in pure dodecanethiol SAM by previous STM study. Also we noticed that these bright spots all appeared at domain boundaries, just as we expected. The second feature we noticed is that the crystalline lattice structure of the domains can be resolved. These results suggest that the Fc-OPE molecules can be successfully doped into the dodecanethiol matrix monolayer with the insertion method, and the crystalline structure of the matrix monolayer was preserved.

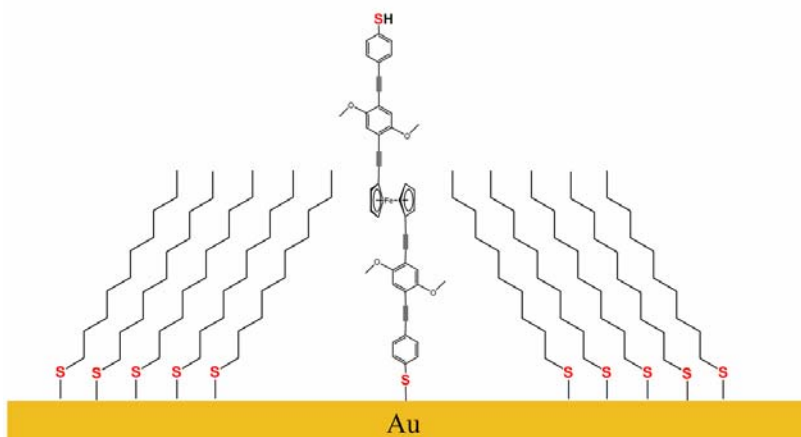
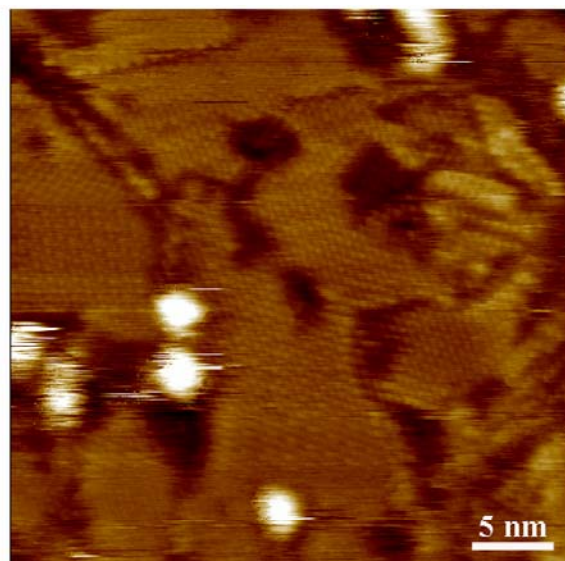


**Figure 32. STM height image (top) and schematic representation (bottom) of dodecanethiol SAM with inserted Fc-OPE molecule.**

The bright spots on the STM image in Figure 32 appeared much larger than the size of single molecules like those dodecanethiol molecules in the domain area. But most spots have relatively uniform size and they are quite scattered on the surface. Based on these facts, we believe these bright spots are really individual Fc-OPE molecule. The larger apparent size on the STM image is probably due to the tip convolution. The physical length of Fc-OPE molecule is around 3.5nm, which is much larger than the thickness of dodecanthiol monolayer ( $\sim 16.5 \text{ \AA}$ ), so the Fc-OPE

molecule will protrude  $\sim 1.8$  nm from the surrounding dodecanethiolate SAM if the Fc-OPE molecule is perpendicular to the substrate as depicted in Figure 32. As the STM tip scans over the individual Fc-OPE molecule, tip convolution will happen due to the finite size of the tip end. In fact, the small size of Fc-OPE molecule makes it act like a “molecular tip” and image the STM tip end when the STM tip passes over it. Thus the size of the bright spots on the STM images reflects the area of the STM tip end that was scanned by individual Fc-OPE molecule. This size depends on the aspect ratio near the STM tip end and will vary with different tips.

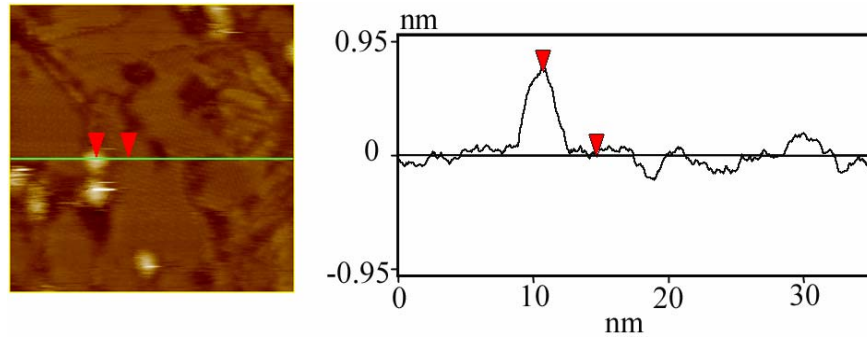


**Figure 33. Cross section analysis of STM constant height image of dodecanethiolate SAM with doped Fc-OPE molecule.**

One interesting note is the apparent height of Fc-OPE molecule relative to the dodecanethiolate matrix monolayer. As we discussed above, the Fc-OPE molecules protrude out of the surrounding monolayer by  $\sim 1.8$  nm if the molecular backbones of Fc-OPE are perpendicular to the substrate surface. However, the cross section analysis (Figure 33) showed the apparent height difference between Fc-OPE molecule and the matrix dodecanthiolate SAM was only  $\sim 7$  Å. As we discussed in **2.3.3.1**, the total transconductance from the STM tip to the gold substrate is

$$G_{total} = G_{gap} \cdot G_{molecule} = A \cdot B e^{-(\alpha h_{gap} + \beta h_{molecule})} \quad (8)$$

Since the STM was under constant current mode, the total transconductance  $G_{\text{total}}$  was controlled to be constant. Thus if dodecanthiolate molecule and Fc-OPE have same transconductance,  $G_{\text{gap}}$  will be the same when the tip scans over both molecules, which as a result will make the apparent height difference between the two molecules be the same as the actual physical height difference. In our specific case, if the conformation of Fc-OPE molecule is as described in Figure 32, the vacuum gap for the case when the tip is above Fc-OPE molecule is  $\sim 1.1$  nm smaller than that when the tip is above dodecanthiolate molecule (Figure 34), which means the transconductance of the gap is much smaller when the tip is above Fc-OPE molecule. Since the total transconductance remains the same for both cases, the transconductance through Fc-OPE molecule must be significantly smaller than dodecanthiolate molecule.

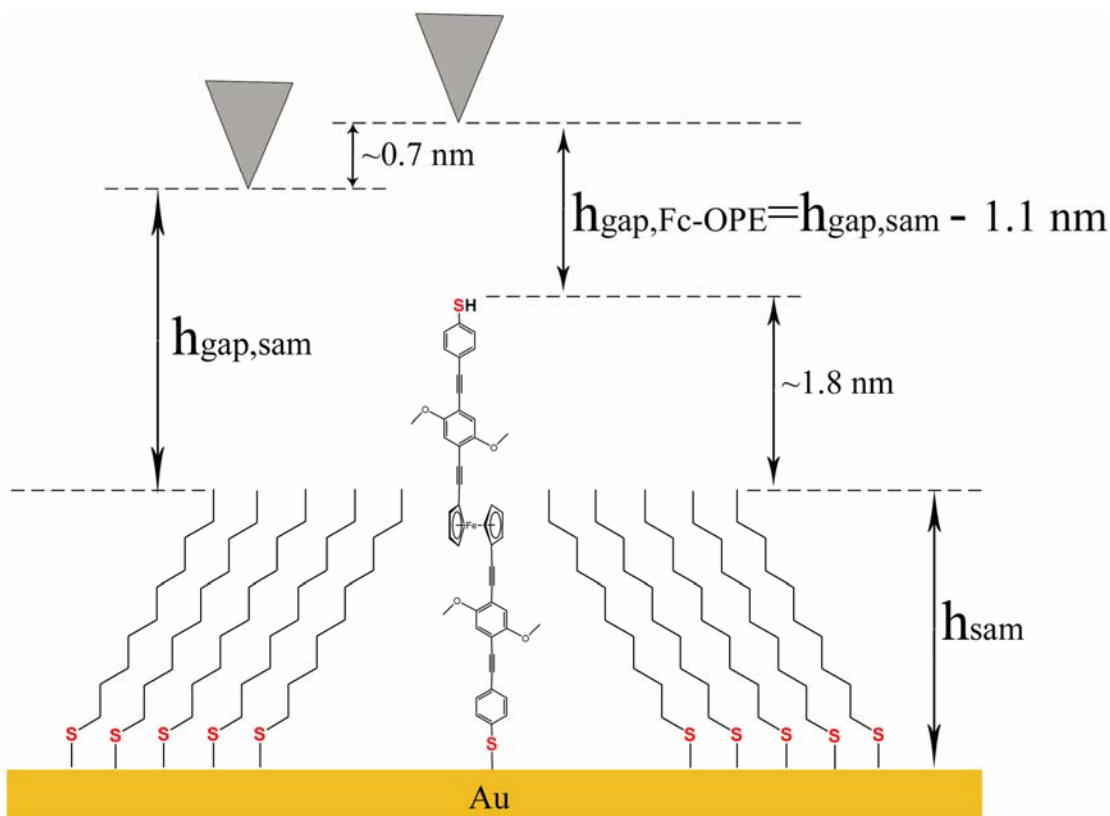


**Figure 34. Analysis of the STM image in Figure 32, assuming each Fc-OPE molecule is perpendicular to the substrate.**

Dunbar and co-workers studied the insertion of some phenylethynyl oligomers (Scheme 2) into alkanethiolate SAM<sup>45</sup> with STM, ellipsometry and infrared spectroscopy. The results indicated the phenylethynyl oligomer molecules were tilted in the host alkanethiolate SAMs. More specifically, for molecule III in Scheme 2, it was found the molecular axis approaches alignment with the host SAM, as the fraction of molecule III decreases in the mixed monolayer. In our case, since Fc-OPE molecule has similar structure with molecule III in Scheme 2, it is possible that it also tilts in the matrix dodecanethiolate SAM. However, even if we assume the molecular axis of Fc-OPE tilts 30°, which is typical for alkanethiolate molecules, the physical height difference between Fc-OPE and dodecanethiolate SAM is still more than 1 nm.

According to apparent height analysis of the STM image, the gap spacing between the STM tip and Fc-OPE molecule is still smaller than that between the tip and dodecanethiolate SAM, and thus the transconductance of Fc-OPE is still much smaller than dodecanethiolate molecules.

The unique molecular structure of Fc-OPE molecule can make analysis even more complicated. First, one of the interesting properties of ferrocene is that the cyclopentadienyl (Cp) rings can rotate around the Cp-Fe-Cp bond axis. It is well known that the barrier of such rotation is quite low, approximately 0.9 kcal/mol for pure ferrocene. So it is highly possible that Fc-OPE molecule is bent around the ferrocene moiety, while the bottom half of the molecular chain can still be normal to the substrate surface or tilt  $30^\circ$  (Figure 35). The direct result of such bent conformation of Fc-OPE molecule is the physical height difference between Fc-OPE and dodecanethiolate SAM is possibly very small, depending on (1) the bent angle around the ferrocene unit and (2) the tilt angle of the bottom half molecular chain of Fc-OPE relative to the substrate surface. If the physical height difference is smaller than  $7 \text{ \AA}$ , the transconductance through Fc-OPE molecule can be higher than the dodecanethiolate molecules.

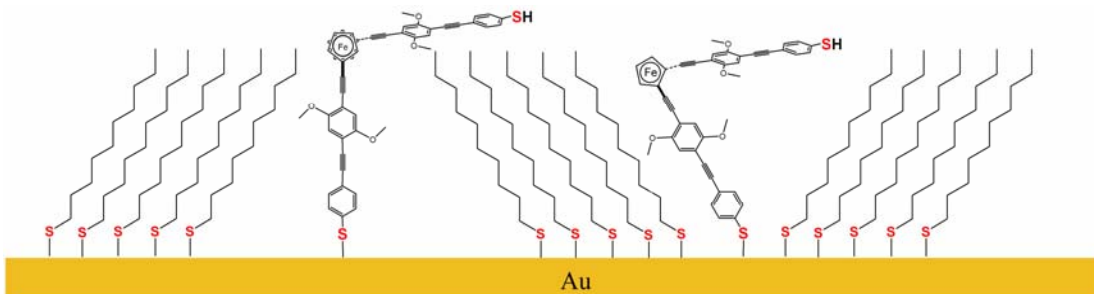


**Figure 35. Possible conformations of Fc-OPE molecule in dodecanethiolate matrix SAM. Fc-OPE molecule may be bent around the ferrocene unit.**



Second, Fc-OPE molecule has two thiol groups at the ends, so it can form two S-Au bonds with the substrate. Figure 36 gives two possible conformations of Fc-OPE molecule where it forms double S-Au bonds to Au substrate. There are other possible conformations, but the one in Figure 36 (a) provides the highest height. With this conformation, Fc-OPE molecule is physically  $\sim 1$  Å higher than the dodecanthiolate SAM. Thus if in the STM image (Figure 32) all molecules of Fc-OPE were in this conformation, we can infer that the tip-(Fc-OPE) transconductance was much smaller than the tip-dodecanthiolate SAM transconductance, which indicates that transconductance through Fc-OPE molecule is higher than dodecanethiolate molecule.

In short, based on the STM results, Fc-OPE molecule can be much more conductive or much less conductive than the surrounding dodecanethiolate molecules, depending on the actual conformation of Fc-OPE in the matrix SAM. More detailed characterization is required before further conclusions can be made.

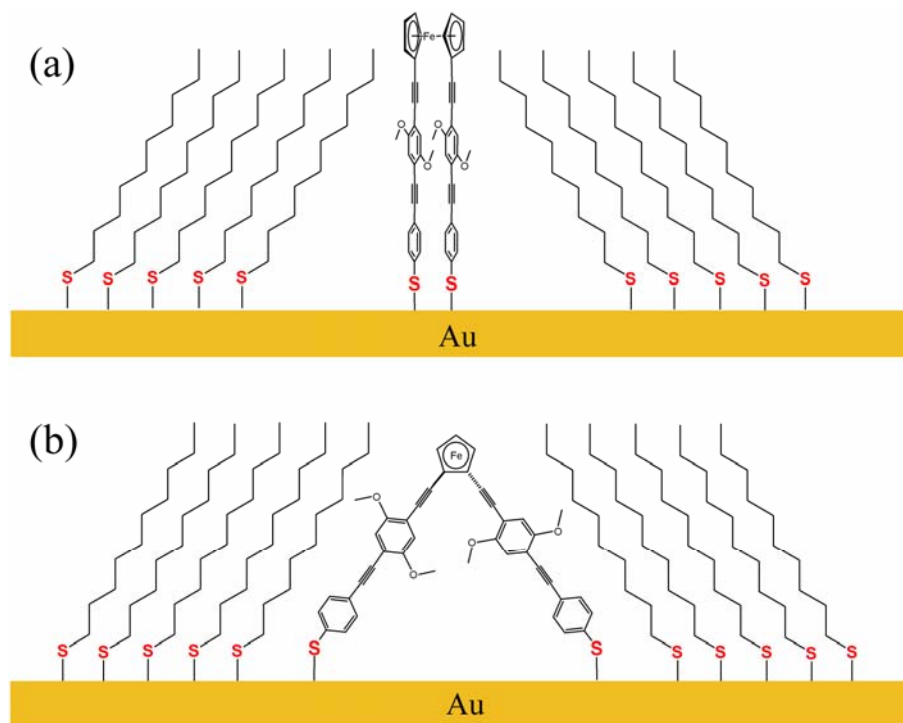


**Figure 36. Possible conformations of Fc-OPE molecule in dodecanethiolate SAM with both ends bonded with the Au substrate.**

#### **2.4 Fabrication of Au(substrate)-molecule 1-Au(nanoparticle) junctions.**

It would be of interest to see if the Au(substrate)-(Fc-OPE)-Au(nanoparticle) junctions can be made by soaking a dodecanethiolate SAM doped with molecule 1 in a Au nanoparticle solution. Although the conformation of Fc-OPE can't be determined decisively from STM study, it is possible that there will be free thiol groups on the SAM surface. Even if each Fc-OPE molecule forms double S-Au bonds to the Au substrate, the molecules may diffuse in the defect sites, which means the S-Au bond may break and form S-Au bond with gold nanoparticles from the solution.

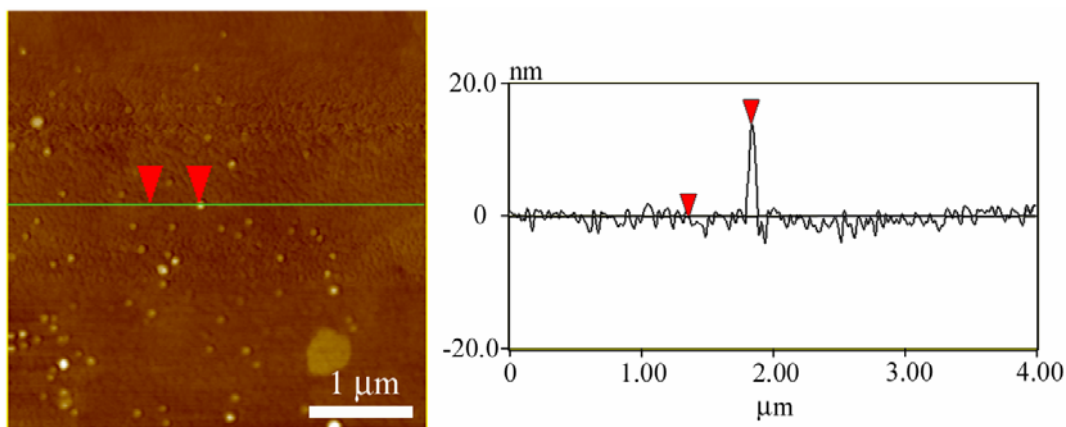


**Figure 37. AFM image of Au nanoparticles on dodecanethiolate SAM with inserted Fc-OPE molecules, and cross section analysis over one particle.**

Based on this idea, a sample was made by putting a doped dodecanethiolate SAM in solution of Au nanoparticle (~15 nm in diameter) for 1 hour. The sample was characterized by AFM and one image was shown in Figure 37. Nanoparticles are clearly visible on the surface, and the cross section analysis revealed the height of the particles was in the range of 7- 17 nm. The average diameter of the nanoparticles derived from this cross section analysis is lower than that from TEM images. One possible reason is that when the AFM tip scans over the nanoparticles, it deforms the

nanoparticles and makes them appear shorter on the AFM images. Another possible reason is that smaller particles may bind better to the molecules, and thus they can more likely survive the rinsing process than the bigger particles, which will result in more small particles on the surface.

These results demonstrated that such Au(substrate)-(Fc-OPE)-Au(nanoparticle) junctions can be successfully fabricated following the method described in Figure 16. And thus we can carry out I-V measurements once we set up the electrical circuit and instruments.

## **2.5 I-V measurements of self-assembled monolayer with conductive probe AFM (CP-AFM).**

### **2.5.1 Some considerations about CP-AFM measurements**

To measure conductance of individual molecules or molecular devices, good insulation from the environment is critical, especially when the current signal is weak, such as current signal at pico- or nano-amp range. In our case, the normal sample holder and tip holder were made of steel and couldn't be used (Figure 38(a) and (b)). A new sample holder was fabricated which isolates the sample from the steel plate with a Teflon layer (Figure 38(c)). It was found that the tip holder used for fluid cell experiment (Figure 38(d)) serves our project well since the main body is made of plastics and the resistance is high enough to insulate the tip well from the rest part of the AFM system.

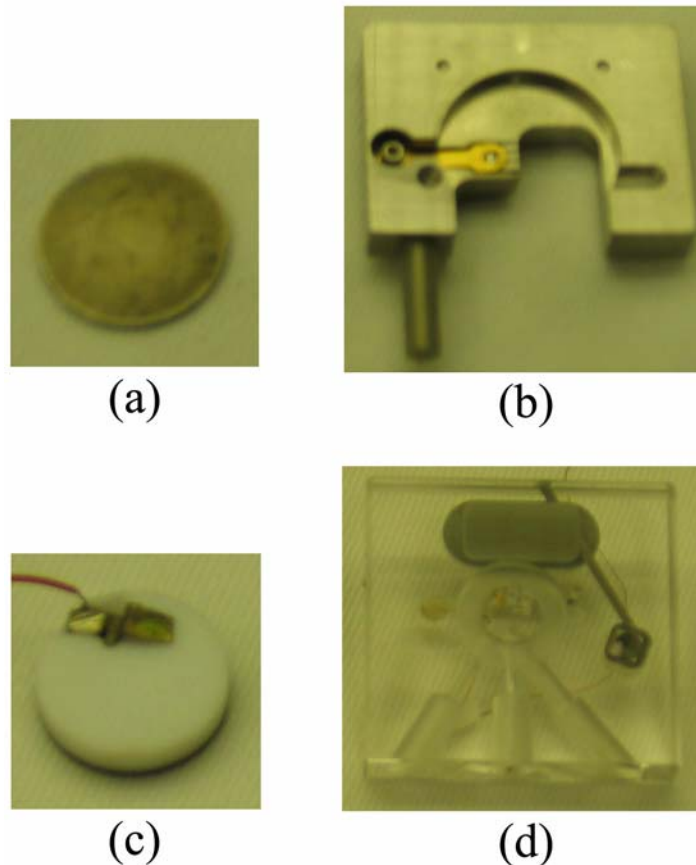


**Figure 38. Normal sample holder (a) and tip holder (b), in contrast to the home-made sample holder (c) and the tip holder for fluid cell (d).**

The tip is also very important for our set up and two aspects need to be considered. First, the tip needs to be highly conductive. This can be easily realized by metalizing the tip through thermal evaporation of certain metal. Noble metals such as Au and Pt are usually chosen due to their availability and chemical inertness. Pt coated tips are commercially available, while the Au coated tips were made in our lab. Usually an adhesion layer of 5 nm Cr was first evaporated, followed by evaporation of 50 nm Au. A typical SEM image of such Au/Cr coated tip was shown in Figure 39. The grainy surface of Au film could be observed (Figure 39(c)), but the film was continuous even at the end of the tip (Figure 39(b)).

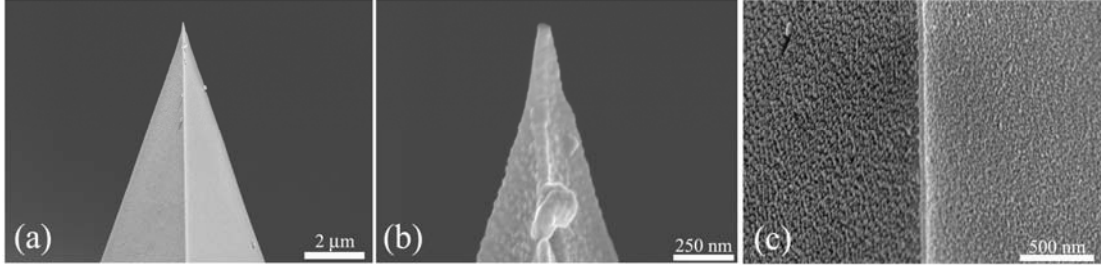


**Figure 39. SEM images of an Au/Cr coated Si tip**

The second concern is the force constant of the tip. It is desired that the deformation of the monolayer be minimized when in contact with the tip, so that the perturbation to the electronic properties of the monolayer will be small enough. A tip with small force constant is easier to manipulate when small contact force is required. The force constant of a tip is dependent on the cantilever dimensions and can be estimated by the following equation:

$$k = \frac{Ewt^3}{4l^3} \quad (9)$$

where  $k$  is the force constant,  $E$  is the elastic modulus of the cantilever,  $w$  is the width,  $t$  is the thickness,  $l$  is the length of the tip cantilever. Since  $k \propto l^{-3}$ , smaller force constants can be obtained simply by increasing the cantilever length, which is widely used in commercial manufacturing.

The tip-sample interaction can be complicated when the measurement is conducted under ambient conditions. It is well known that a thin water layer usually forms on the sample surface. When a tip approaches close enough to the surface, a meniscus will form between the tip and the surface (Figure 40). The capillary force caused by this meniscus will pull the tip towards the surface. This capillary force is difficult to predict, as it depends on many factors, such as the shape of the meniscus,

the thickness of the water layer and the tip surface material. One efficient way to avoid such capillary force is to immerse the whole tip and sample surface in certain inert liquid, thus the possibility of meniscus formation can be eliminated. This can be demonstrated by force plot, which measures the tip deflection when the scanner moves the sample vertically.

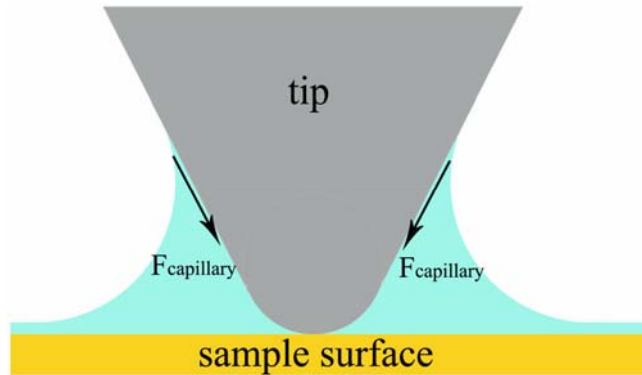


**Figure 40. Illustration of capillary force caused by formation of meniscus between tip and sample surface.**

Figure 41 shows force plots that were obtained with normal Si tips. Under ambient conditions (Figure 41(a)), initially the tip is quite far away from the sample surface, so the force curve is almost flat because the tip-sample interaction is negligible. When the tip is close to the surface, a meniscus forms between the tip and sample surface, and the tip gets pulled down to touch the surface. This shows on the force plot as a small sudden decrease of the tip deflection, where the small increase prior to that point may due to the repulsion force from the surface tension of the water layer. After the tip touches the sample surface, the tip deflection usually increases linearly with the vertical increase of the sample surface. When the sample retracts vertically, the deflection curve decreases linearly first, but when the tip reflection reaches the initial point where there is no force exerted on the tip and continue

retracting, the capillary force is strong enough to pull down the cantilever, which on the force plot shows as the curve keeps decreasing. At certain point the capillary force can't hold the cantilever anymore and the cantilever bounces back to the initial position. Such hysteresis in the force plot during one extending-retracting cycle is direct result from the meniscus formation. No hysteresis was observed on the force plot where the tip and sample surface were both under fluid of dodecane (Figure 41(b)). The capillary force caused by the meniscus can be estimated from the force plot by calculating the force needed to overcome the capillary force. The tip used in Figure 41(a) has force constant at 0.5-1.0 N/m according to the data sheet from the manufacturer. Since the tip retracted extra  $\sim 25$  nm before the tip pulled off the meniscus, the total capillary force on the tip is around 12-25 nN. Considering the contact area between the tip and sample is very small due to the sharpness of the AFM tip, such capillary force will result in huge pressure on the surface. For instance, capillary force of 20 nN on a 20nm-radius circular area will give pressure more than  $1 \times 10^7$  Pa. Such high pressure may deform the monolayer, destroy the crystalline structure and induce defects. Conducting the experiments under inert fluid would eliminate such capillary force and maintain the integrity of the monolayers.



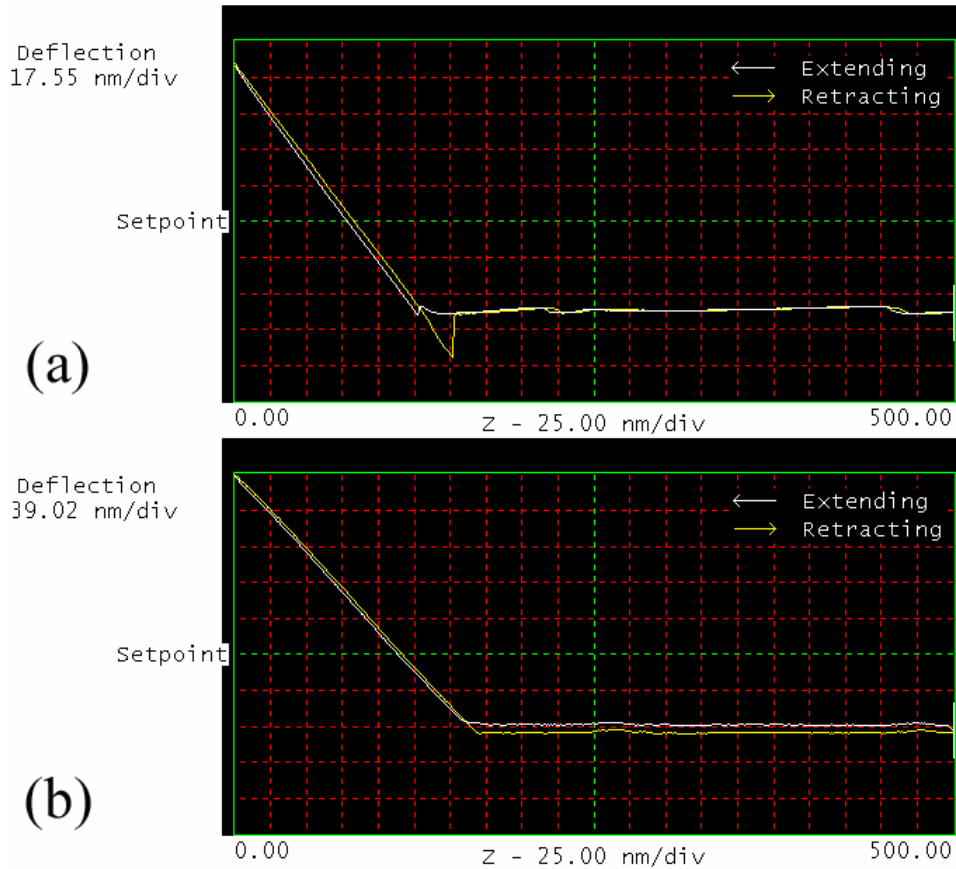


**Figure 41. Typical force curves under (a) ambient condition and (b) organic fluid (dodecane).**

### 2.5.2 CP-AFM set-up

The basic concept of CP-AFM is illustrated in Figure 4. In particular, a multimode AFM (Nanoscope IIIa, DI) was utilized to fabricate the Au-monolayer-Au junctions, and a few drops of inert organic fluid such as dodecane were used on the sample surface so that the tip would be completely immersed in liquid and thus avoid the formation of meniscus between the tip and sample surface. The tip and sample substrate (Au) were connected to a Keithley 236 Source-Measure unit, which provides bias to the circuit and also measures the current in the circuit with high precision. To avoid damage to the instrument by possible electrical short between the tip and gold substrate, a 1.0 M $\Omega$  resistor was inserted between the tip and the Source-

Measure unit. The whole measurement was conducted on a computer which is connected to the source measurement unit through a GPIB interface card. The measurement software was developed in our group with Labview. Figure 42 shows the set-up for I-V measurements.

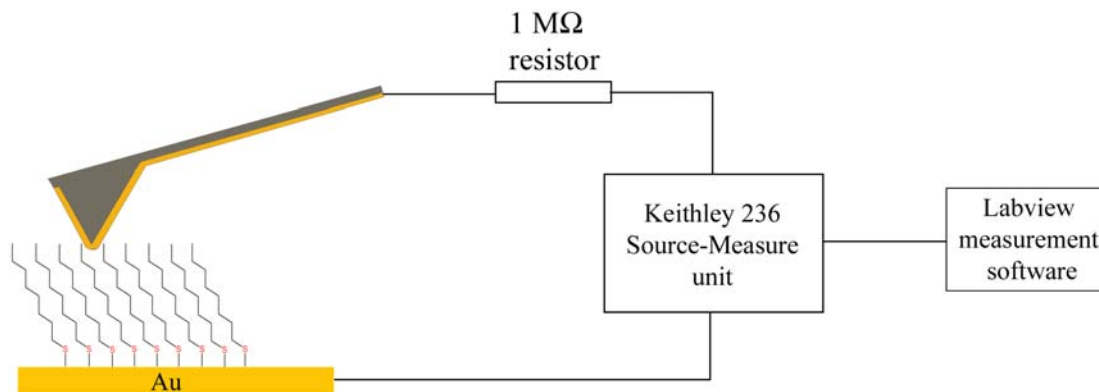


**Figure 42. Diagram of general set-up for CP-AFM measurement.**

Before the I-V measurement, the force curve of the tip was taken to determine the slope, which will be used to determine the actual z-direction bending of the tip according to the laser reflection. The contact force will be decided and controlled by precisely tuning the z-direction bending. Both the tip and the Au substrate were grounded at first. The tip was then brought down to get in touch with the SAM surface under certain load (usually 2 nN). Finally the voltage on the tip was controlled by the software to sweep in a range and the current was measured simultaneously.

### **2.5.3 Results and discussion**

To avoid any possible random event that could happen during the measurement, several I-V measurements on the same spot were usually taken to check the reproducibility of the results. Figure 43 demonstrated three I-V curves taken from the

same spot on a dodecanethiol SAM sample. The experiment was carried out under dodecane with a gold coated Si tip (Nanosensors, force constant 0.15 N/m, with a 5 nm Cr adhesion layer and 50 nm Au layer). The three I-V curves from Figure 43(a) showed poor reproducibility from each other, especially at high bias regions (bias > 0.4 V). Large discrepancy was observed among these three I-V curves when we zoomed into low bias region of -0.3 V~ 0.3 V. This result indicates that strong perturbations existed during the measurements of I-V characteristics.

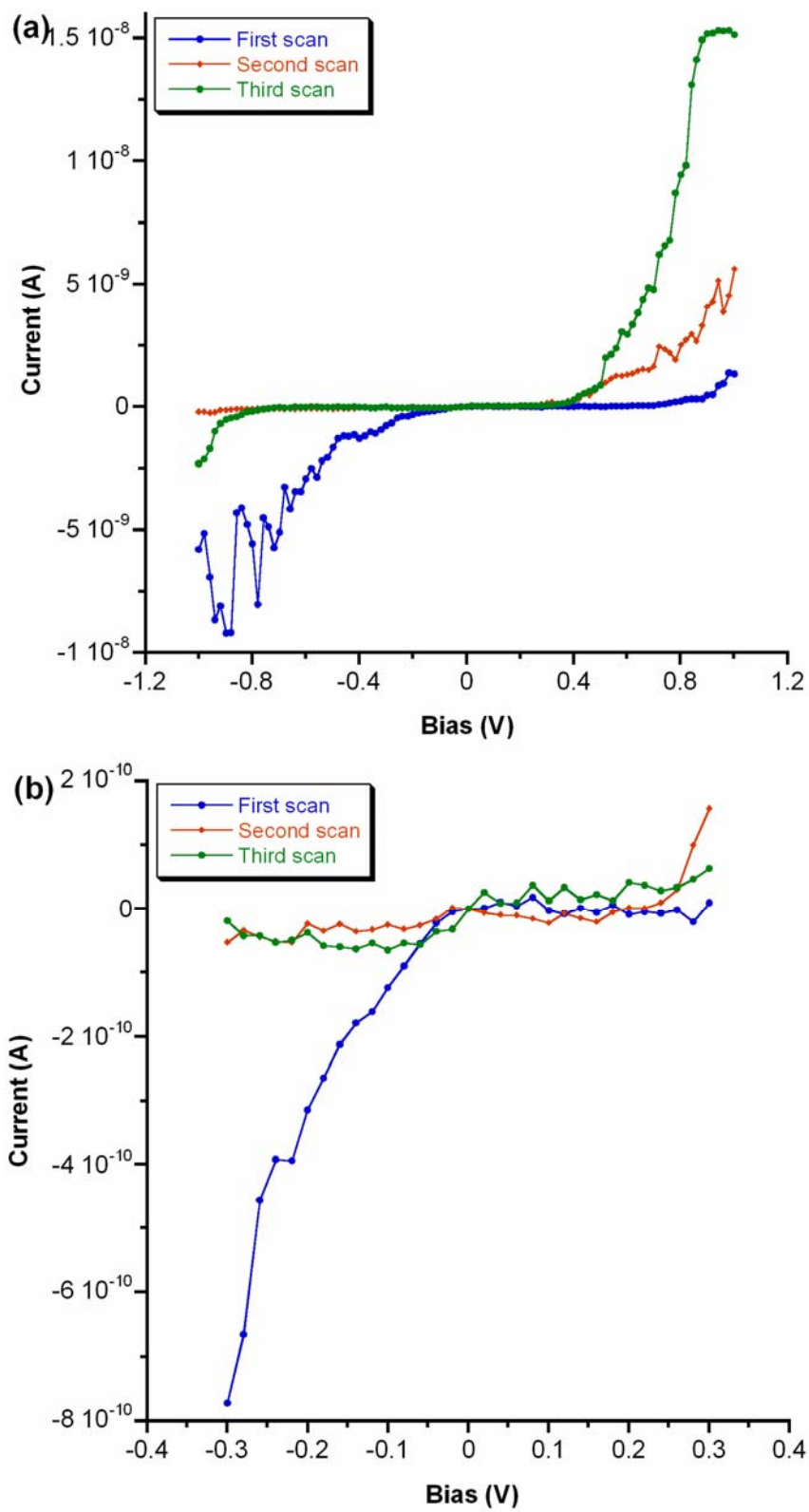


Figure 43. Consecutive three I-V scans on the same spot with CP-AFM on one dodecanethiol SAM, (a) scan range -1.0~1.0 V, (b) zoom in at -0.3~0.3 V.

To check the possibility that the poor reproducibility resulted from certain defects in our electrical circuit setup, two test experiments were conducted. One is I-V measurement on a known resistor, and the other is noise measurement for the open circuit.

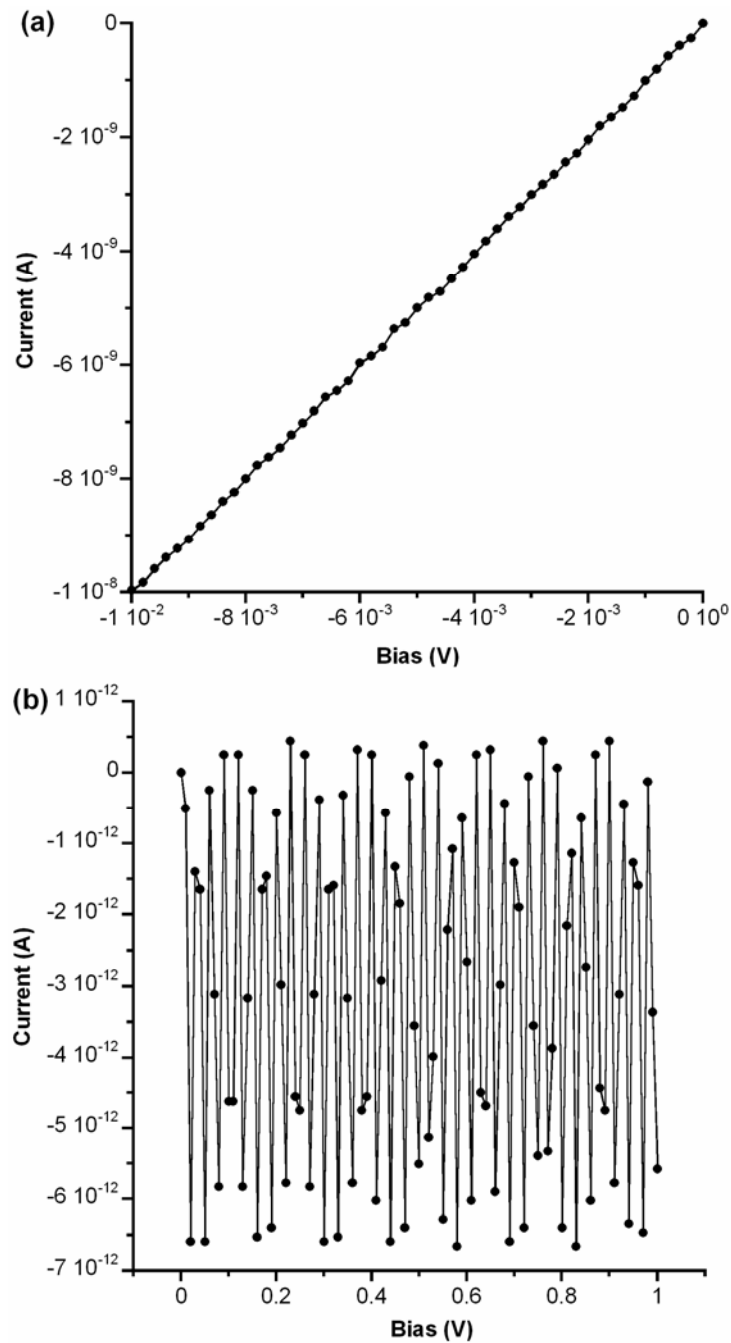


Figure 44. (a) I-V curves of a 1 M resistor, (b) noise measurement of the open circuit.

The first experiment was carried out by simply shorting the conductive tip and the Au substrate. To achieve this, the load on the tip was controlled to be much higher than what was used in I-V measurements on the dodecanethiol SAM, such that the tip can penetrate the SAM and contact directly with the gold substrate. The threshold load varies with different tips, probably due to the variation of tip sharpness, but the loads we used were usually greater than 20 nN. Once the tip was shorted with the gold substrate, the resistance of the circuit is mainly from the  $1\text{M}\Omega$  resistor. Thus the I-V curve of the whole circuit should show the I-V characteristics through a normal resistor. Figure 44(a) shows the typical I-V curve of such experiment. The linear relationship between the current and the bias was obvious and the resistance derived from the slope of the I-V curve was exactly  $1\text{M}\Omega$ , just as we expected. During the experiment, the bias was carefully controlled so that the current would be mainly in the nA region, which is the region we would expect from the I-V curve of a SAM sample, and the smooth I-V curve demonstrated that data acquisition in the nA region is fine with our electrical set up.

In the second experiment we left the electrical circuit open by keeping the tip far away from the sample, and measured the current while sweeping the bias from the source measurement unit. Such measurement should give us a crude idea of the noise level in our set up. Figure 44(b) shows the I-V characteristics of the open circuit and we can see the noise level is on the order of  $10^{-12}\text{A}$ , or pA level, which we believe is low enough for our measurements.

These two test experiments clearly show that the poor reproducibility in our I-V measurements was not caused by any defects in the design of electrical set-up, and

it must come from other sources. One possible source is the thermal drift during the CP-AFM measurements. Such drift occurs not only in the x-y plane, but also in the z-direction. Drifting in the x-y plane means that the conductive tip constantly moved on the sample surface during measurements. Since the surface of the SAM is not uniform and there are sites with structures different from the bulk crystalline SAM, such as domain boundary, lattice vacancy and possible contaminants, the I-V characteristics over these sites can be drastically different from that on bulk SAM. So if the tip drifted over these sites, drastic change would be observed in the I-V curve. Drifting in the z-direction, however, is probably not a big concern during the measurement, as the feedback loop can compensate the drift quickly.

Another possible source of poor reproducibility may come from the deformation of the tip end. Even under small loads of a few nN, the pressure at the very end of the AFM tip can be quite considerable due to the small contact area, which can make the Au layer deform over time. The existence of friction between the tip and sample surface during thermal drifting can exacerbate such deformation. Moreover, the SAM is usually thinner than a few nm, thus the electrical field between the tip and gold substrate can be quite large. The surface gold atoms may flow along the surface under high electrical field during the measurement, which can change the morphology of the tip end as well as the contact area over time. According to the widely accepted tunneling model for charge transfer through alkanethiol monolayers, such deformation at the tip end will increase the tunneling paths and thus change the I-V characteristics obtained from the experiment. To verify such tip deformation during the experiments, three conductive tips with different histories were examined by SEM

and the results were shown in Figure 45. The first tip was a freshly coated tip, and the nice sharp tip end can be observed in the SEM image (Figure 45(a)) The second tip was also a Au coated tip but was slightly used with a few I-V measurements under low bias (in the region of -1.0 V to +1.0 V). The SEM image (Figure 45(b)) clearly showed the deformation at the tip end. The third gold coated tip was used for a long period of time and sometimes under high bias (-5.0 V to +5.0 V). Severe deformation, or damage, of the tip end can be seen in the image (Figure 45(c)). These results demonstrated the vulnerability of a metal coated tip under the conditions of our I-V measurements, which may explain the poor reproducibility of the I-V curves.

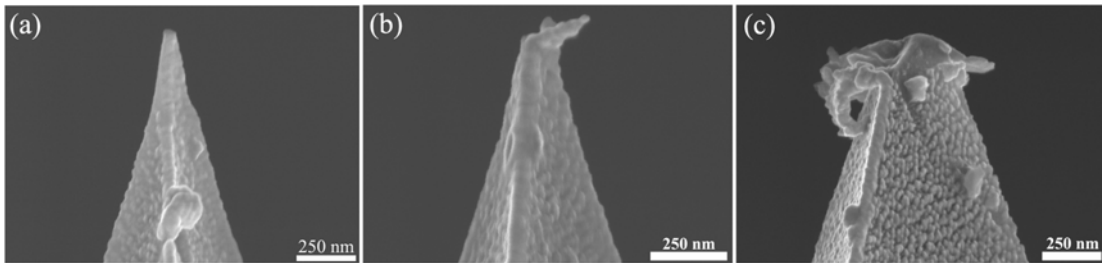


**Figure 45. Au coated AFM tips. (a) a fresh one (b) under low bias for a few sweeps (c) after long time use**

To solve the problems of thermal drift and tip deformation may turn out to be quite difficult. Operating the experiment under low temperature can reduce the effect of thermal drift, but measures have to be taken to avoid water condensation on the AFM system under ambient conditions. Furthermore, as we used organic liquid to avoid meniscus formation, the temperature can't be lowered close to the freezing point of the organic liquid. Putting the AFM system under high vacuum can avoid both the use of liquid and the meniscus formation, but that requires a complete redesign of the experimental set-up. Similarly, it's almost impossible to eliminate tip deformation completely during the experiment, but there are approaches that may



help to help minimize it. One natural thought is to reduce the load of the tip so that the extent of deformation will also decrease. However, it is difficult to control forces lower than 1 nN both consistently and accurately, considering that the external perturbations can be comparable in magnitude. A more feasible method is to increase the tip radius, so that the pressure at the tip end will be much smaller under the same load compared to a sharper tip (smaller tip radius). But this approach doesn't decrease the deformation caused by thermal drift, and the friction force can be much larger with a dull tip since it increases with contact area under the same load. Furthermore, regarding the test structure depicted in Figure 16, a conductive tip with much larger radius will greatly increase the chance of contacting multiple nanoparticles simultaneously, which is not desired for I-V measurement of single molecular junctions. Considering these difficulties, along with the reported charging problem caused by the gold nanoparticles, the CP-AFM technique for characterization of single molecular junctions is likely very difficult, from both the experimental and theoretical views. Thus the other option that we planned originally: break junction through electromigration, may prove to be a better test structure, which will be discussed in the next chapter.

## **2.6 Experiments**

### **Sample preparation**

The substrate was initially gold film (150 nm in thickness) on mica (Molecular Imaging, Inc.). To obtain large atomically flat terraces, the substrate was annealed in a hydrogen flame following the online procedures from Molecular Imaging Inc (website: [www.agilent.com](http://www.agilent.com)). Generally, the substrate was placed on a piece of quartz

in a clean hood (Microvoid Model 4F fume hood, Air Control, Inc.). A quartz-tube torch connected to a H<sub>2</sub> tank was used as the hydrogen flame source. Because the color of hydrogen flame is very light blue, the annealing was done in darkness to make sure the flame is visible. The flow rate of hydrogen was adjusted so that the length of the flame was around 4 cm. The quartz plate around the sample was heated gently first until no water vapor condensed on the plate. The flame tip was then brought to the sample at a 30 degree angle. The distance between the quartz tip end and the sample surface was controlled at around 3 cm. The flame was moved from side to side across the sample surface at a rate of around 1 Hz for 30-60 seconds. Then the sample was allowed to cool for another 30-60 seconds naturally. Propane flame annealing was also mentioned in some papers but hydrogen flame annealing was preferred because the byproduct (water) evaporates and leaves no residual organic contaminants.

The annealed gold substrate was then inserted into corresponding alkane thiol solution for 18-24 hours. The sample was then taken out and rinsed carefully.

### **Preparation of Au/Cr/Si substrate via thermal evaporation**

Gold/chromium film was prepared in a home-made metal evaporator equipped with a Pfeiffer vacuum pump station (TSH 071). Silicon wafers (6 inches in diameter, orientation (111), polished one side, Silicon Sense) were soaked in piranha solution (3:1 H<sub>2</sub>SO<sub>4</sub>:H<sub>2</sub>O<sub>2</sub> mixture) for 15min to remove residual contaminants, rinsed thoroughly in deionized water (resistivity > 18.0 MΩ-cm, Barnstead NanoPure) for 10 min and then flash dried in refluxing isopropanol vapor. One gram of gold wire

(99.99+%, Goodfellow) was wrapped around a tungsten filament coil (R.D. Mathis). A new chromium plated tungsten filament and the gold wrapped w coil were then soaked in hot concentrated nitric acid for 6 hours, rinsed in Nanopure water for 10min and then dried. The cleaned silicon wafer, gold wrapped W coil and Cr plated W filament were installed in the evaporator, and then the evaporator was pumped down immediately to avoid possible particle contaminants on the Si wafer. Base vacuum of around  $1 \times 10^{-5}$  torr could be reached overnight. An adhesion layer of 60 Å Cr was evaporated first at 1 Å/sec rate, followed by 110-150nm gold evaporated at 2-3 Å/sec. Once the evaporation was complete, the wafer was cooled down in vacuum for another 10 min, and then the evaporator was vented with N<sub>2</sub> before the wafer was removed and stored in clean hood.

### **Substrate cleaning and SAM preparation**

The Au/Cr/Si substrates were first soaked in hot Piranha solution for 5 min, rinsed thoroughly with deionized water for 10 min, and then electrochemically cycled from -0.1 V to -0.8 V vs SCE in 1 M NaCl solution for 5 min to strip off any gold oxide. The substrate was then rinsed carefully with deionized water, put on a spin-caster and further rinsed with water, isopropanol, 1-hexane and methylene chloride at 3000 rpm for 2 min. If we wanted to measure the thickness of the monolayer, the substrate was measured first on the ellipsometer (Gaertner model L116C) first to get the parameters like reflective index for the substrate. The substrate was then soaked in the adsorbate thiol solution for 24-48 hours. (Note: Try to let the substrate be perpendicular to the liquid surface to minimize possible particle precipitation from

the solution onto the sample surface). The sample was then rinsed thoroughly with the solvent used in the thiol solution (usually ethanol) and spun dry on the spin caster with isopropanol, 1-hexane and methylene chloride.

### **Preparation of Au nanoparticles with 15 nm in diameter:**

We followed the methods developed by Frens<sup>93</sup> and Hirai<sup>94</sup>. All the following experiments were conducted under ambient conditions.

#### **1. Preparation of Au colloid in water.**

HAuCl<sub>4</sub>·3H<sub>2</sub>O (6.7 mg, 0.017 mmol, Aldrich) was first dissolved in 58 ml Nanopure water, and the solution was heated in oil bath until boiling. A solution of sodium citrate (14.8 mg, 0.050 mmol) in 1.3 ml water was then added to the boiling HAuCl<sub>4</sub> solution. The color of the solution changed to light black in about 5 sec, and after ~30 sec it gradually turned to dark red.

#### **2. Phase transfer of the Au colloid.**

20 ml of aqueous Au colloid, 20 ml hexane and 20 mg sodium oleate were mixed together and emulsified by vigorous stirring. 2.14 g MgCl<sub>2</sub>·6H<sub>2</sub>O was dissolved in 9 ml Nanopure water, and 3 ml of the solution was taken out and added into the emulsion. After 30 min of stirring, the whole mixture was transferred into a separation funnel and sit overnight. The system separated into two phases and the top organic phase was collected.

### **Preparation of Au nanoparticles with ~1.5 nm in diameter:**

We followed the method developed by Weare and co-workers<sup>110</sup>. H<sub>2</sub>AuCl<sub>4</sub>·3H<sub>2</sub>O (1.00 g, 2.54 mmol) and tetraoctylammonium bromide (1.60 g, 2.93 mmol) were dissolved in a mixture of water/toluene (50 ml/65 ml) under nitrogen. The golden color transferred into the organic phase after ~5 min stirring. Triphenylphosphine (PPh<sub>3</sub> 2.32 g, 8.85 mmol) was added and the solution was stirred vigorously until the color changed to white. Aqueous sodium borohydride (NaBH<sub>4</sub>, 1.41g, 37.3 mmol) solution in 10 ml water was freshly prepared and added rapidly. The color of the system changed to dark black immediately, accompanied with vigorous bubbling. After another 3 hours of stirring, the toluene phase was separated with a separation funnel and washed with water (2× 100 ml). The volatiles were then removed *in vacuo*.

The crude product was suspended in 100 ml hexane and placed on filter paper in a Buchner funnel. The following series of washes was performed:

1. 100 ml hexane followed by 100 ml water
2. 5× (100 ml hexane followed by 100 ml methanol: water (2:3) mixture)
3. 5× (100 ml hexane followed by saturated aqueous NaNO<sub>2</sub>)
4. 5× (100 ml hexane followed by 100 ml methanol: water (2:3) mixture)
5. 5× (50 ml hexane followed by 100 ml saturated aqueous NaNO<sub>2</sub>)
6. 5× (50 ml hexane followed by 100 ml methanol: water (2:3) mixture)

The solid was then collected, dissolved in ~30 ml chloroform and filtered through glass wool. The nanoparticles were precipitated by slow addition of pentane (~180 ml). The solid was collected with a Buchner funnel. This precipitation process was repeated twice.

### **Preparation of Au/Cr coated AFM tips**

Gold/chromium coated AFM tips were prepared in the home-made metal evaporator equipped with a Pfeiffer vacuum pump station (TSH 071). One gram of gold wire (99.99+%, Goodfellow) was tightly wrapped around a tungsten filament coil (R.D. Mathis). A new chromium plated tungsten filament and the gold wrapped W coil were then soaked in hot concentrated nitric acid for 6 hours, rinsed with Nanopure water for 10min and then dried. Several new AFM tips were attached to a copper plate by copper wire clips. The copper plate, gold wrapped W coil and Cr plated W filament were installed in the evaporator, and then the evaporator was pumped down immediately to avoid possible particle contaminants. Base vacuum of around  $1 \times 10^{-5}$  torr could be reached overnight. An adhesion layer of 50 Å Cr was evaporated first at 1 Å/sec rate, followed by 50nm gold evaporated at 2-3 Å/sec. Once the evaporation was complete, the tips were cooled down in vacuum for another 10 min, and then the evaporator was vented with N<sub>2</sub> before the tips were removed and stored in clean hood or a desiccator.

### **Preparation of STM tips:**

We used a 3-step approach which is similar to the one developed by Lindahl *et al.*<sup>96</sup> Figure 46 demonstrated the experimental set up for step 1. In an electrolyte solution of CaCl<sub>2</sub>(sat.)/H<sub>2</sub>O/HCl (60/40/4 ml), a short piece of Pt/Ir wire (Pt 80%, Ir 20%, ~1.5 cm in length and 0.25 mm in diameter, Goodfellow) was used as working electrode, with one end immersed about 1.5 mm into the electrolyte. A carbon rod (99.997%, 5 mm in diameter, Goodfellow) acted as the counter electrode. An ac

voltage of 25  $V_{\text{rms}}$ /50 Hz was applied and the current was monitored with a multimeter. The initial current was controlled at  $\sim 250 \text{ mA}_{\text{rms}}$  by carefully adjusting the length of wire under the electrolyte surface. Vigorous etching was visible, and the color of electrolyte slowly changed to green. The current decreases as the etching continues, which is due to the decreasing contact area between the Pt/Ir wire and the electrolyte. The etching was stopped once the current dropped almost a factor of 10, around  $30 \text{ mA}_{\text{rms}}$ . A droplet shape usually formed at the wire end after step 1. (see Figure 46). The wire was then rinsed carefully with deionized water and air dried.

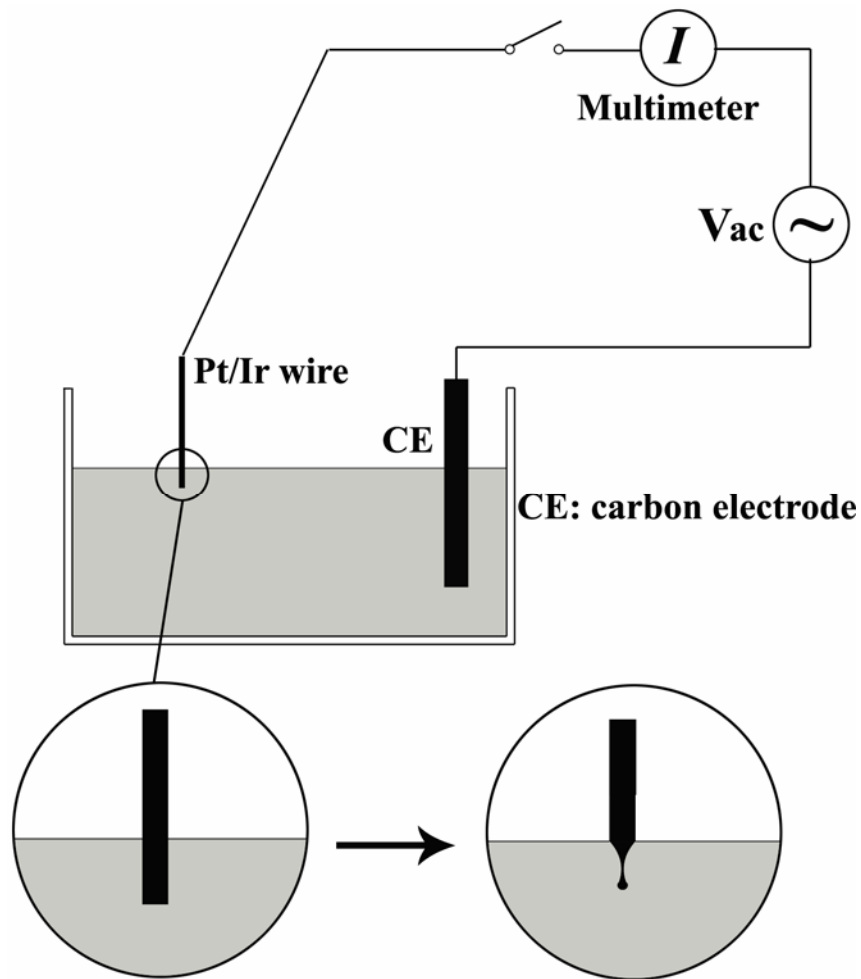
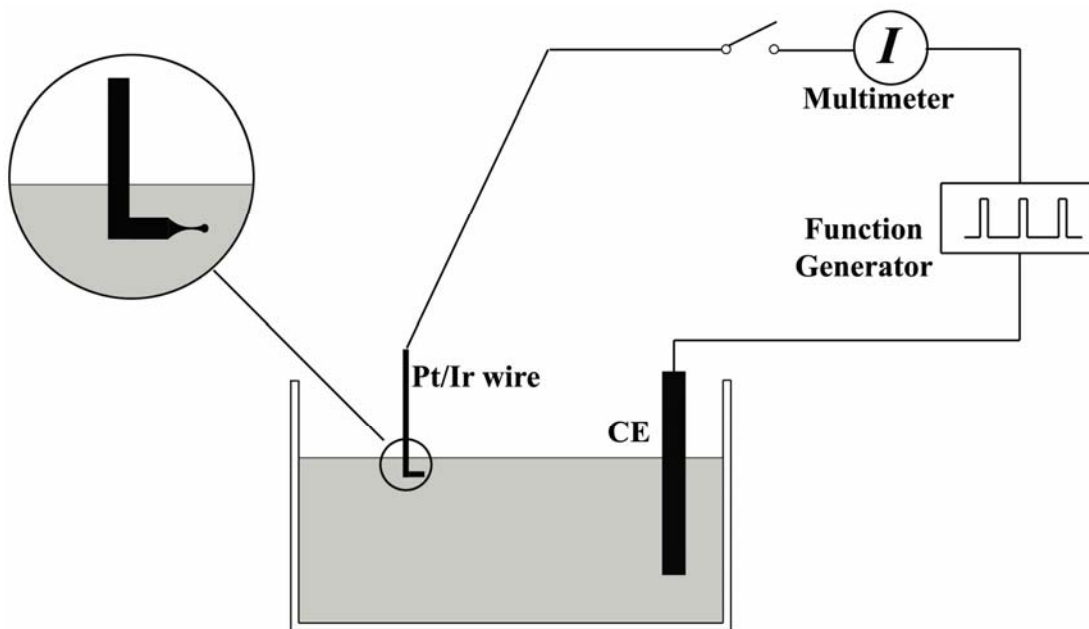


Figure 46. Fabrication of STM tips, Step 1.

In the second step (Figure 47), the droplet shaped wire end was bent 90° about 4-5 mm above the droplet, and immersed about 2 mm below the electrolyte surface. The electrolyte was changed to H<sub>2</sub>SO<sub>4</sub>/H<sub>2</sub>O (90/10 ml) and a function generator was used to generate a square wave at 40 kHz with maximum at +10 V for 40 μs and minimum at -0.5 V for the rest of each period. The purpose of step two is to thin down the wire neck near the droplet until the droplet falls off. The pulsed square wave was used to assure slow etching rate. Once the droplet falls off, the etching continues for another 10 sec. It is believed that the tip sharpens during this 10 sec period<sup>96</sup>. The whole etching time of step 2 varies in the range of 5-10 min depending on the thickness of the neck. After step 2, the tip was grounded (by turning off the function generator) to stop further etching.



**Figure 47. Fabrication of STM tips, Step 2.**

For step three, the etched wire and carbon electrode were transferred to another container with fresh electrolyte (H<sub>2</sub>SO<sub>4</sub>/H<sub>2</sub>O, same as that in step two). The etched



Pt/Ir wire was held at  $-1.1 V_{dc}$  (from function generator) for 2 min to reduce possible oxide that was formed previously in step one and two. The etched tip was rinsed carefully with deionized water and dried.

## **Chapter 3: I-V measurement on ferrocene-based molecules with break junction test structure.**

This chapter will present the collaborative study of our group with Dr. Stephanie A. Getty, Prof. Michael S. Fuhrer in Department of Physics, and Rui Liu, San-Huang Ke, Prof. Harold U. Baranger, Prof. Weitao Yang in Department of Chemistry and Department of Physics, Duke University. The experimental part, including fabrication of gold wires, breaking the wires by electromigration and measurements of the junctions, was mainly carried out by Dr. Stephanie A. Getty. The computational part was mainly carried out by Rui Liu, San-Huang Ke, Prof. Harold U. Baranger, Prof. Weitao Yang. For more details, please refer to our published paper<sup>111</sup>.

### **3.1 Fabrication of Au-molecule-Au test structures in break junctions via electromigration.**

The whole fabrication process of molecular test structure contains three steps: (a) the fabrication of patterns containing thin gold wires for electromigration, (b) formation of molecular monolayer on the gold wires through self-assembly and (c) breaking the thin gold wires for molecular junction formation by electromigration under low temperature. The detailed procedures were described below.

#### **(a) fabrication of patterns with thin gold wires for electromigration**

This process is to make a test pattern on Si wafer with thin gold wires for future electromigration process. Multiple steps of e-beam lithography were used to make such patterns. Due to the complexity and time cost for each e-beam lithography step, a pattern with dozens of thin gold wires was designed so that multiple molecular

junctions can be made on each pattern. The final layout of such pattern was illustrated in Figure 48. The big square pads on the outer side of the pattern (Figure 48(a)) are electrodes for future external electrical connections. Each gold thin wire (Figure 48(c)) is 30 nm thick and the width is smaller than 50 nm. These gold wires were fabricated on top of a common Al gate electrode (the U-shaped structure around the center of Figure 48(b)), and each wire was connected to a common electrode at one end, either source or drain, while the other end was connected to a corresponding big pad.

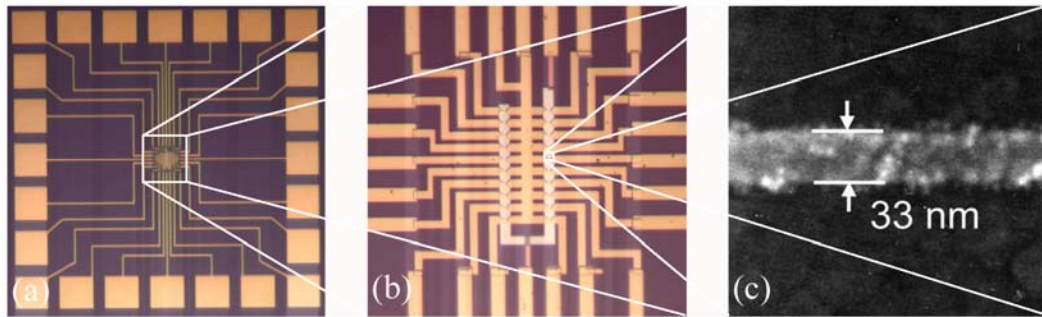


**Figure 48. A complete test pattern on Silicon wafer. (a) overview, (b) magnified image of the thin gold wire array on top of the common Al gate electrode, (c) one gold thin wire with width of 33 nm.**

To fabricate such a pattern, usually four steps of e-beam lithography were required, with sequence of (1) aligning marks, (2) Al gate electrode, (3) thin gold wire array, and (4) large pads and corresponding connection paths to the thin gold wires. The whole pattern was fabricated on a piece of Si wafer with 500 nm of thermally grown SiO<sub>2</sub> at the surface. For each e-beam lithography step, the Si wafer sample was first cleaned and a thin layer of PMMA photoresist was spin-casted onto it. The sample was then transferred into a SEM chamber. The e-beam of the SEM was employed to write patterns in the photoresist layer with controlled dose. The written pattern was developed in isopropanol afterwards. A layer of gold, with controlled

thickness, was deposited on the sample in a metal evaporator, and the PMMA photoresist was subsequently removed with acetone. The sample was dried and ready for the next step of e-beam lithography.

After the whole pattern was fabricated, a quick check was performed on a home-made 4-probe station to find out if there are any broken wires, by measuring the I-V curves across the thin gold wires to see if the curve was ohmic.

**(b) Formation of molecular monolayer on the gold wires through self-assembly.**

A solution of 0.1 M interested dithiol molecules (ferrocene oligophenylethynyl dithiol (Fc-OPE) or pure oligophenylethynyl dithiol (OPE), see Figure 13) was prepared in methylenechloride, and the solution was purged with pure nitrogen gas for several minutes to remove dissolved oxygen. The Si wafer sample with pre-made pattern was cleaned by rinsing with high purity organic solvent. If the sample has been sitting in air for days, O<sub>2</sub> plasma treatment was carried out first to remove possible organic contaminants on the sample surface. The cleaned sample was then immersed in the prepared thiol solution for 24 hours for monolayer formation. After the sample was rinsed carefully in organic solvents, it was dried and glued to a home-made sample holder, where wire bonding was carried out. The sample was then introduced into a sample-in-vapor <sup>4</sup>He cryostat and the system was pumped down to its base vacuum. We tried to minimize the exposure time of the sample to air during this process, since it is well known that the S-Au bonds can be oxidized under ambient conditions.

**(c) Breaking the thin gold wires for molecular junction formation by electromigration.**

Electromigration was performed under low temperature to avoid the formation of large gaps due to fast melting down of the gold wires upon breaking. Fabrication of gaps that are only a few nm wide was believed to be critical for successful formation of Au-molecule-Au test structure. Once the system was cooled down to the base temperature, which is 1.3 K, the bias across the gold wire was ramped up slowly, while the current flowing through the gold wire was carefully monitored. The bias usually stops at 0.5 V so that the breaking process wouldn't happen too fast (under higher voltage). Electromigration took place when the current decreased, and a gap was believed to form when a sudden, large drop in current was observed, upon which the bias was removed immediately.

Figure 49(b) is a SEM image of the top view of a nanogap made from electromigration process. The inset was a demonstration of a ferrocene oligophenylethynyl dithiol (Fc-OPE) molecule bonded to both electrodes inside the nanogaps. The side view of cross section along the gold wire was illustrated in Figure 49(a). The whole configuration was very similar to a field effect transistor, with the Au-molecule-Au test structure lying on top of an Al gate electrode.

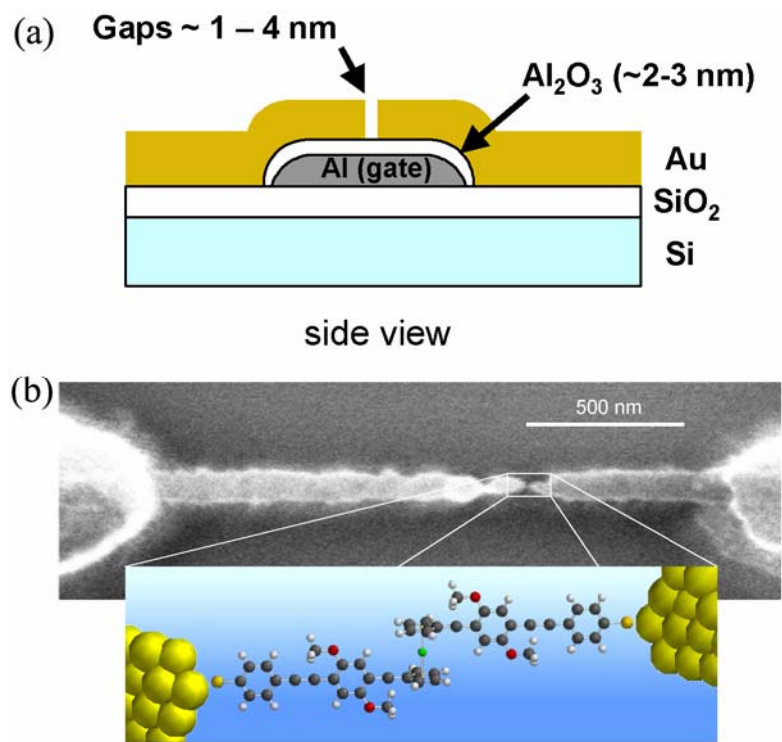


**Figure 49. Illustration of nanogaps formed by electromigration. (a) imaginary side view of the nanogaps, (b) SEM image of a nanogap, inset is illustration of a molecule of ferrocene oligophenylethynyl dithiol bonded to both electrodes inside the nanogap.**

### **3.2 I-V characterization of nanogaps by electromigration without molecules**

To date, the exact details of formation of Au-molecule-Au junction during the electromigration process are still unknown to researchers. The widely accepted hypothesis is that molecules near the nanogap might migrate when electromigration occurs, and a few molecules may diffuse into the gap and bond with both electrodes to form Au-molecule-Au junction. As mentioned before, one critical factor for the Au-molecule-Au junction formation is the size of the nanogaps. It's impossible to form an Au-molecule-Au junction if the nanogap is wider than the length of the molecule in fully extended conformation. While for a nanogap narrower than the molecule length, the molecule may tilt or bend inside the gap to bond to both

electrodes and such conformation change may affect the I-V characteristics of the junction. Unfortunately, there hasn't been any report about precise control of the size of the nanogaps formed by electromigration, since the technique is relatively new. As a consequence, it has been reported that the success rate of formation of Au-molecule-Au junction through electromigration technique is less than 20%<sup>59,61</sup>. Because of this low success rate, it is helpful to measure the I-V characteristics of open nanogaps without molecules, so that we can identify I-V curves of Au-molecule-Au junctions from those of open junctions in the future.

Over 75 nanogaps were formed by electromigration in the absence of any molecules and these nanogaps were characterized by measuring the I-V curves. The curves showed the conductances through these nanogaps range from pS to nS, and the conductance increases with voltage for each nanogap, which is consistent with the expected tunneling behavior in electron transport. Occasionally Coulomb blockade behaviors were observed in some nanogaps, with Coulomb charging energies of a few meV. Such behaviors may result from accidental formation of a gold island inside of or near to the nanogap during the electromigration process, thus the whole junction behaves as a single electron transistor.

### **3.3 I-V characterization of the Au-molecule-Au test structure.**

I-V curves were measured right after the formation of nanogaps following the procedures described in 2.6.1 while the base temperature of 1.3 K was maintained during the measurements. We first studied the nanogaps formed in the presence of Fc-OPE molecules (Figure 50(a)). Over 50 junctions were fabricated and characterized, and only 5 of them exhibited significant conductance, as showed in Figure 50(b)-(f).

The rest junctions showed conductances consistent with those open nanogaps formed without any molecules. During the measurements, we noticed that the I-V curves that obtained from these 5 nanogap junctions are quite stable and reproducible. For example, five measurements were carried out and plotted in Figure 50(b), and these curves are almost identical. In all five plots, broad peaks at  $V < 100$  mV were observed in the conductance vs bias curves, which we believe is due to resonant tunneling when the electron energy in one electrode aligns with certain molecular energy state. Some of the conductance peaks showed high conductances compared with the conductance quantum  $G_0$ , such as  $0.6G_0$  in Figure 50(b),  $0.7G_0$  in Figure 50(d) and  $1.4G_0$  in Figure 50(e). Three plots showed multiple pairs of peaks in conductance curves, and we measured the dependence of these curves on gate voltage changes, as shown in Figure 50(c), (e), (f). The results exhibited profound effect of gate voltage on the charge transport behavior, especially in Figure 50(c) and (e), where in Figure 50(c) the two peaks move in opposite directions with increased gate voltages, and in Figure 50(e) it seems one peak moves through the other as gate voltage increases. Another common feature in these five plots is the finite conductance at  $V = 0$  V, and the insets showed a local minimum near zero bias in each conductance curve.



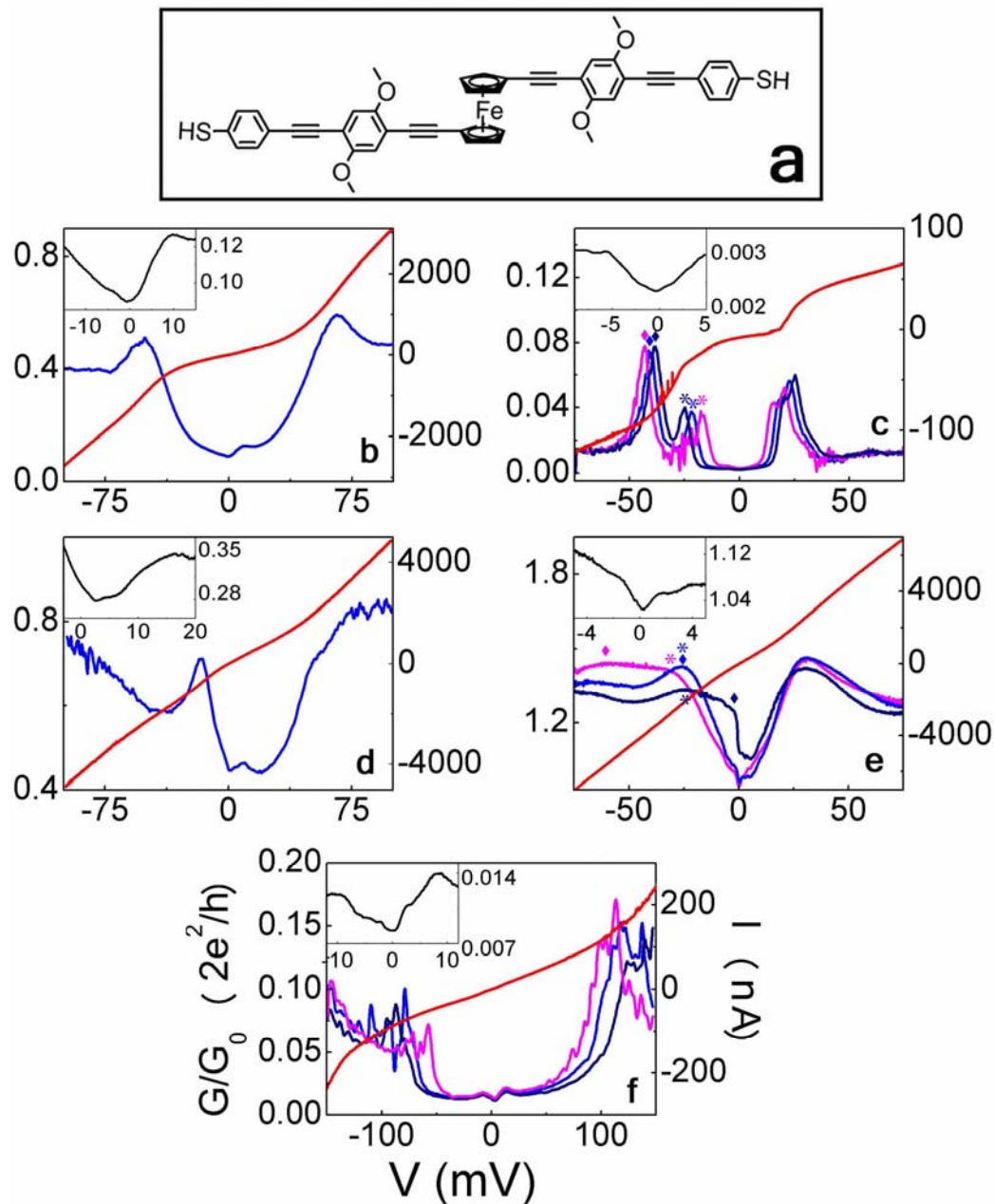


**Figure 50.** I-V characteristics of five nanogap junctions formed in the presence of Fc-OPE. (a) Fc-OPE molecule, (b)-(f): Current (red) and conductance (dark blue, light blue or purple) vs. bias curves. The insets are conductance curves under low bias regions. Gate voltages are: (c) dark blue: -5 V, light blue: 0 V, purple: +5 V (e) dark blue: -1V, light blue: 0 V, purple: +1 V (f) dark blue: +1.1 V, light blue: +1.4 V, purple: +1.7 V.

One most important question to us is: Do these curves show characteristics caused by individual molecules or ensemble of large number of molecules in the

junctions? We believe that these five plots are from junctions with only one or two molecules inside the nanogaps, based on the following reasons.

First, as we pointed out previously, the success rate to make Au-molecule-Au junctions is quite low, from both our experience and the literature. This low success rate resulted from poor control of the nanogap size and possibly short diffusion time for molecules. With current electromigration technique, the size control of the nanogaps is still a challenge for researchers because the detailed mechanism and kinetics are still unknown. On the other hand, if the hypothesis of molecular diffusion is true, such diffusion can be very slow due to the low temperature during the experiment. The transient temperature near the nanogap can be higher than the base temperature when electromigration occurs, and thus the mobility of nearby molecules may also be higher. Unfortunately the electromigration time in our experiments is usually quite short (~10 sec). It is difficult for molecule to diffuse to the “good site” where it can bond with both leads in that short period of time before the nanogap cools down and molecular mobility becomes very slow. These two difficulties suggest that the junctions we fabricated consists more likely very limited number of molecules, and chances to fabricate a junction with large number of molecules can be extremely low.

Second, Cui and coworkers found the I-V curves that they obtained from alkanedithiol molecules with CP-AFM technique can be normalized into a “basic” curve by dividing the I-V curves with different integers<sup>21</sup>, which they believed to be because different number of molecules were measured in each measurement. While in our case, the curves in the five plots of Figure 50 can't be normalized into such a

“basic” curve, since the conductance peak positions are different in each plot. We believe the difference among these conductance peaks is due to different bonding and electrostatic environment of individual molecules in each junction. As we mentioned previously, since the geometry and width of the nanogaps are not well controlled, the molecule inside the nanogap may have to tilt or even bend to bond to both leads. Also the molecular states can be perturbed by the electrostatic potential of the gate if the molecule is close to the gate electrode<sup>112</sup>. As a result, such conformational changes and electrostatic perturbation can affect the charge transport behavior through the molecule and cause the shift of conductance peaks. Two pairs of peaks were observed in Figure 50(c) and (e), which we believe is because two molecules existed inside the nanogap, but they bonded to the leads differently and/or they are in different distances from the gate.

Finally, the different behavior of the peak positions in response to the gate voltage changes (Figure 50(c) and (e)) also suggest these two pairs of peaks are from two molecules instead of from two states in a single molecule.

With these arguments, we believe that the current and conductance curves in Figure 50 are characteristics of Au-molecule-Au junctions with only one or two molecules in the nanogaps. And the nanogaps from electromigration technique turned out to be a successful test structure for fabrication of metal-molecule-metal junctions, albeit the success rate is quite low (<20%).

The conduction peaks in Figure 50 were ascribed to be resonant conduction due to the discrete energy states caused by the Fc-OPE molecule. Although a more strict way to describe the electronic properties of the Au-molecule-Au junction

requires considering the junction as a whole instead of only the molecule, it is very possible that the electronic states of the whole junction are still discrete and these states can be considered as a result from perturbation of the molecular states of Fc-OPE molecule through bonding to both gold leads. Thus resonant tunneling can still occur when the electron energy in the bulk gold aligns with some electronic state of the junction.

The total conductance through the molecular junction can be described as

$$G(V) = \frac{2e^2}{h} \sum_{ij} T_{ij}(E, V) = G_0 \sum_{ij} T_{ij}(E, V) \quad (11)$$

where  $T_{ij}$  is the transmission probability for each conduction channel. During resonant conduction, the transmission probability through resonant state increases sharply and becomes dominant over all conduction channels, which exhibits as peaks in the conductance curves. The conductance near resonant conduction thus can be expressed as  $G(V) = G_0 T_{res}$ , where  $T_{res}$  is the transmission probability through the resonant state. So when  $T_{res}$  is high, the conductance of the molecular junction may exhibit conductance close to the conductance quantum  $G_0$ . Conductance peaks with values of  $0.6G_0$  and  $0.7G_0$  were observed in Figure 50(b) and (d), which agrees with the theory quite well. To our knowledge, this is the first time where the experimental results agree with theoretical predictions in a single-molecule based junction. In Figure 50(e), conductance value greater than  $G_0$  was observed, but we believe it's due to overlapping of two peaks from two molecules inside the same junction.

Near resonant conduction, the transmission coefficient can be written as

$$T_{res} = \frac{\Gamma_1 \Gamma_2}{\Gamma} \frac{\Gamma}{(E - E_m)^2 + \Gamma^2} \quad (12)$$

where  $\Gamma_1$  and  $\Gamma_2$  are coupling parameters at the molecule/gold interfaces of both ends,  $\Gamma = \Gamma_1 + \Gamma_2$ , and  $E_m$  is the energy of the  $m$ th resonant state. If we suppose the coupling parameters  $\Gamma_1$  and  $\Gamma_2$  are constant once the junction was formed, we can tell from the above equation that each resonant state will result in a pair of Lorentzian peaks in conductance curve centered at  $\pm 2E_m/e$  with half-width  $2\Gamma/e$ , since the resonant state can align with electron energy in either electrode when the bias sweeps in both positive and negative regions.

Lorentzian fits thus were carried out in conductance curves in Figure 50(b) and (c), as shown in Figure 51.

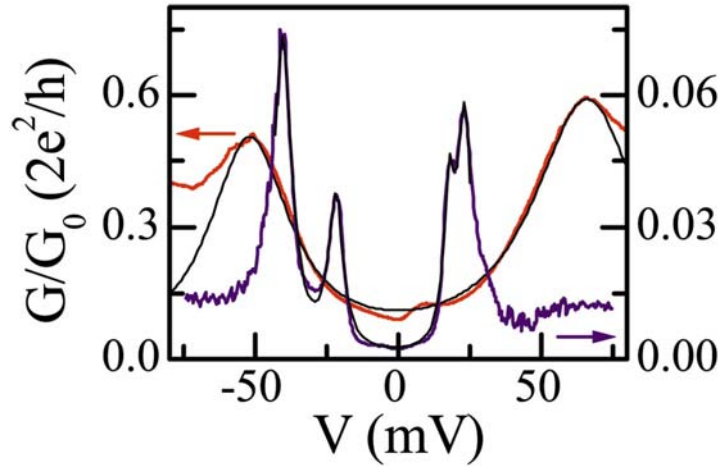


**Figure 51. Lorentzian fits for conductance curves from Figure 50(b) and (c). The red curve and purple-blue curve are experimental results, and the black curves are Lorentzian fits of the data.**

The results of the Lorentzian fitting are very encouraging. The fitted curves agree with the experimental ones fairly well, and the overlapping of the Lorentzian peaks at 0 V clearly explains the zero-bias conductance. It is noticed that the

experimental curves deviate from the fitted curves at higher biases, which is possibly due to the existence of inelastic conduction channels. From the Lorentzian fitting, we also obtained half-width of all the peaks, thus the coupling parameter  $\Gamma$  can be extracted according to our theory. It was found that  $\Gamma$  varies from 1.2 to 12 meV, much larger than the thermal energy under the experimental conditions ( $k_B T \approx 0.11 \text{ meV}$  at 1.3 K), which suggests that the coupling between the molecule and the leads is quite strong and stable.

To study the effect of ferrocene moiety on the charge transfer behavior of the molecular junctions, we also measured I-V curves from junctions in the presence of oligophenylethynyl dithiol (OPE) (Figure 52(a)). The OPE molecule has similar structure to Fc-OPE, but has a phenyl group in the center instead of a ferrocene unit. The junctions were fabricated in the same way as those with Fc-OPE molecules. Out of 50 junctions we made, 4 junctions demonstrated significant conductance and they were showed in Figure 52(b)-(e). Two significant differences were noticed compared with those I-V curves in Figure 50 where Fc-OPE molecules were used. The first is the low conductivity of these junctions, which showed as much lower current under the same bias compared with those I-V curves in Figure 50. The second is that zero-conductance gaps over several hundred mV were observed in these I-V curves, which were absent from those in Figure 50. Since the I-V curves in both figures were obtained under similar experimental conditions, we believe the difference in the molecular structures between Fc-OPE and OPE should account for the huge differences of the results.

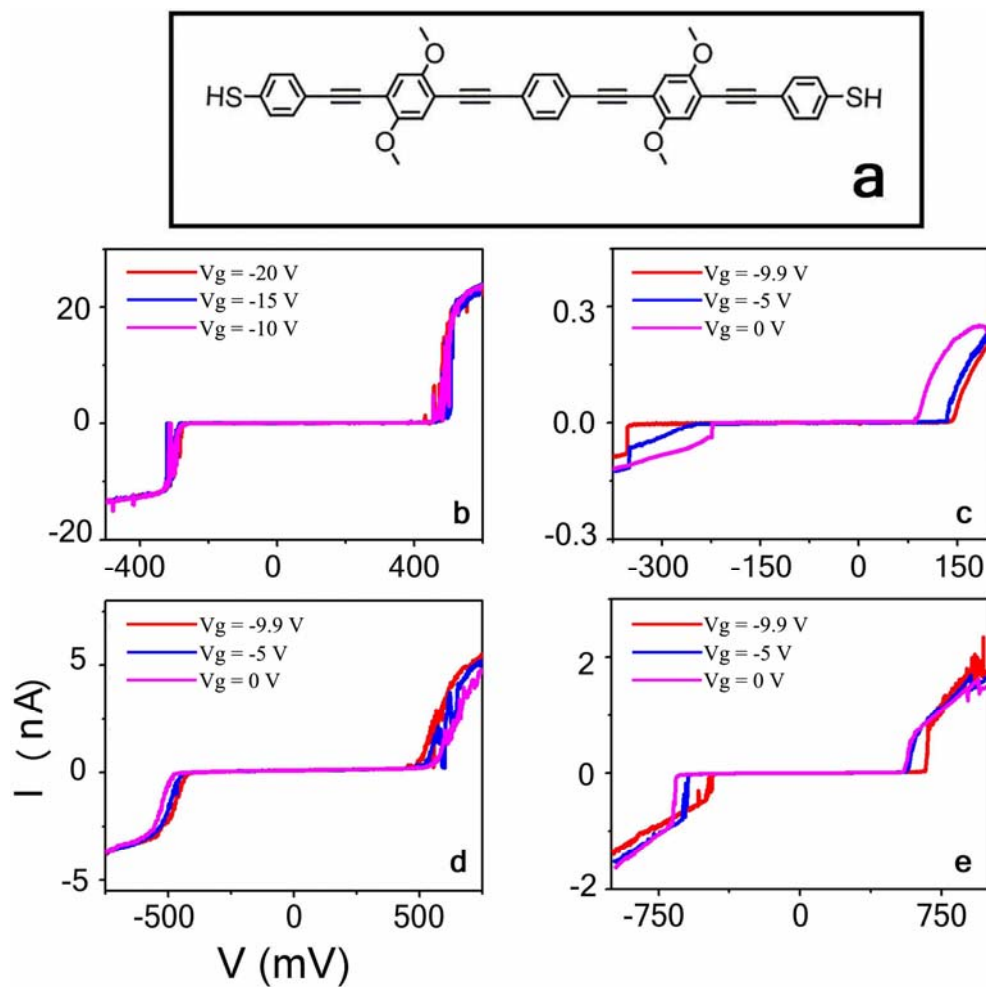


**Figure 52. I-V characteristics of four nanogap junctions formed in the presence of OPE molecules.**

Our collaborators in Duke University also carried out computational calculations for our Au-(Fc-OPE)-Au and Au-OPE-Au junctions. Density functional theory (DFT), combined with non-equilibrium Green's function (NEGF) was used to calculate electron transport through such junctions. Figure 53 shows the results of the calculations.

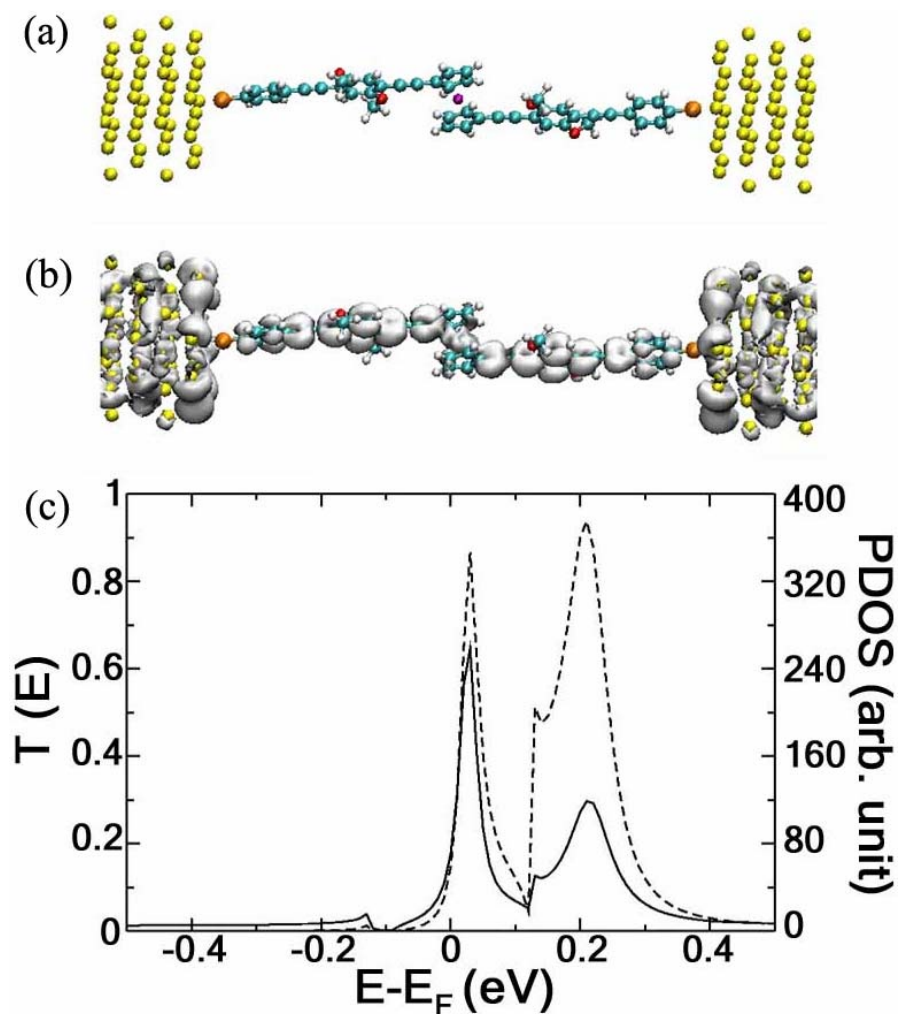


**Figure 53. (a) Relaxed configuration of Fc-OPE molecule between two gold (001) leads. (b) The surface of local density of states (LDOS) of the junction at resonant transmission. (c) Transmission between the gold leads (dashed line) and the density of states projected onto the molecule (solid line) at zero bias.**

The configuration of the Fc-OPE molecule at the lowest energy was depicted in Figure 53(a), with fully extended backbone and coplanar phenyl rings. The plot of  $T(E)$  in Figure 53(c) shows a clear resonance peak 30 mV above the Fermi energy, with near-perfect transmission ( $T > 0.8$ ). The local density of states (LDOS) of the junction at resonance energy was also shown in Figure 53(b), where a conjugated level traversing the whole junction can be observed. These results agree very well with our experiments.



As for the Au-OPE-Au junctions, the theoretical calculations show that for the configuration where the five phenyl rings are coplanar, the conductance should be high, which is in sharp disagreement with the experiments. Such discrepancy between theory and experiments for conjugated molecules is a well-known problem in the field of molecular electronics. The possible causes in our case will be discussed below.

The exact role of ferrocene moiety in the electronic property of these junctions is still not clear to us. But it's clear to us that the ferrocene unit should account for the huge enhancement in conductivity of Au-(Fc-OPE)-Au junctions over Au-OPE-Au junctions. One possible reason is that the existence of ferrocene enhances the coplanarity of the phenyl rings in Fc-OPE molecules, while the phenyl rings in OPE molecules tend to be noncoplanar, which greatly reduces the conductance of the junction because of the broken conjugation. Another possible reason is the introduction of ferrocene unit also makes the molecule more flexible as the backbone of the molecule can bend around the ferrocene unit. Such increased flexibility may play a big role in the experiments. The theoretical calculations always suppose a perfect junction where the width of the nanogap is exactly the length of the molecule, which is in fact very difficult to achieve with the immature electromigration technique. The introduction of ferrocene unit into the molecule can increase the error tolerance in junction formation, as for some imperfect nanogaps, the molecule may bend to fit in to form Au-molecule-Au junction. Also the computational calculation showed that bent Fc-OPE has a conductance lower than a linear one, but of the same order. OPE molecules, on the other hand, have very stiff backbones and thus have

more difficulties in junction formation. The OPE molecules may bond poorly to the leads in some junctions, which in return can greatly reduce the conductance through the junctions. Both of the reasons listed here may account for the disagreement in conductance between the theoretical calculations and experiments for conjugated molecules.

### **3.4 Conclusion and future plans**

We have tried two test structures for molecular junction formation and subsequent measurements. One is formed by insertion of certain dithiol molecules into an alkanethiol self-assembled monolayer (SAM), followed by tethering the free thiol end with gold nanoparticles. The test structure can then be measured with CP-AFM. We have successfully fabricated such test structures using alkanedithiol molecules. The matrix SAM, mixed monolayer with inserted dithiol molecules, and final test structure with gold nanoparticles were characterized by ellipsometry, AFM and STM. However, the CP-AFM measurements were very irreproducible, even on an alkanethiol SAM. We believe the problem comes from two possible causes, namely thermal drift and deformation of the metalized tips.

The other test structure was from insertion of molecules into nanogaps made by electromigration technique. Although the success rate is quite low (<20%), such Au-molecule-Au junctions were fabricated and the I-V characteristics were measured. Two molecules were tested and drastically different properties were observed from junctions with different molecules. For Fc-OPE molecules, near perfect conductance peaks ( $>0.6G_0$ ) were observed in some junctions and we also found the junctions we made usually contain only one or two molecules inside the nanogaps. We ascribe the

peaks in the conductance curves to resonant conduction through certain discrete states of the junctions. From Landauer formula and some assumptions, we predicted that theoretically for each resonant state, a pair of Lorentzian peaks should be observed in conductance curves. The subsequent fittings showed that the observed peaks agreed with Lorentzian fitting quite well. Computational calculation also predicted high conductance through such junctions and the existence of resonant peaks, which also agree well with experiments. The junctions with OPE molecules, however, showed poor conductance. It is possible that the ferrocene unit inside Fc-OPE enhances conduction through the molecular junctions because (a) it enhances the coplanarity of the phenyl rings and (b) it makes the molecule more flexible, which helps the formation of Au-molecule-Au junction under current experimental conditions.

Since the nanogap from electromigrations showed to be a successful test structure for characterization of single molecular junctions, more molecules will be tested with such test structure in the future. In particular, we have synthesized molecules with two ferrocene units in the backbones and we are interested in the I-V characteristics of junctions with such molecules. Will the additional ferrocene unit further enhance the conductance of the junction? We also want to verify if our concept of molecular diode that depicted in Scheme 2 is true or not. These experiments will bring more exciting results, and more theoretical calculations will be carried out for better understanding of the details in such molecular devices.

## **Chapter 4: Growing Pd nanowires on Highly Ordered Pyrolytic Graphite (HOPG).**

### **4.1. Introduction.**

Metal nanoparticles and nanowires attract much attention as they can be model systems for 0- and 1-dimensional structures<sup>113-116</sup> in solid-state physics and they also have potential applications in nanoscale devices such as interconnects<sup>117,118</sup>, sensors<sup>119-125</sup> and magnetic storage media<sup>126,127</sup>. Numerous methods<sup>128,129</sup> have been developed to prepare nanoparticles and nanowires in controlled fashion. Among these methods, template assisted growth has been shown to be a clean and convenient way. In this method, a sample with certain patterns, such as arrays of metal nanoparticles and nanopores in a membrane, is first fabricated. These patterns serve as templates for the following metal nanowire or nanoparticle growth. The final shape and property of the nanowires usually depend on, or is determined by the template that was fabricated originally. The templates can be positive, negative or surface templates based on their geometrical shapes and fabrication techniques. The following section describes these three kinds of templates and related nanowire growth methods individually.

#### 1. Positive templates

Positive templates for metal nanowire growth are usually wires or wire-like objects with diameter at nanometer scale. Metal material is first deposited on the

surface of the template wires with physical or chemical approaches, and metal nanowires can be subsequently obtained by removing the template wires.

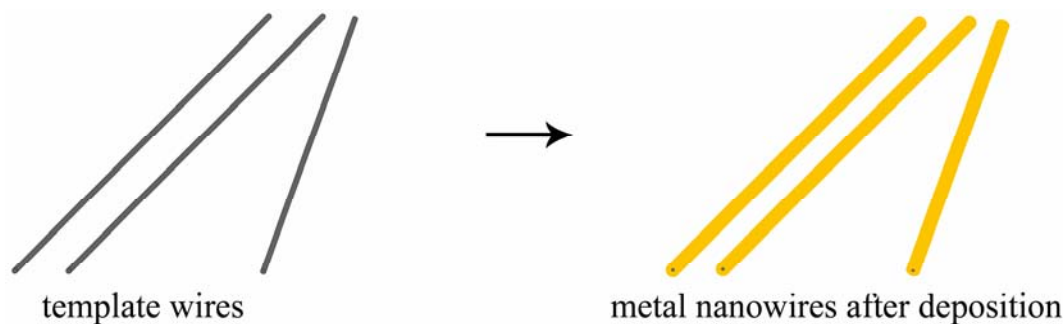


**Figure 54. Metal nanowires from deposition of metal onto positive template wires.**

Carbon nanotube<sup>130</sup> (CNT) was found to be a good positive template, due to its small feature size and unique physical properties. The deposition methods of metal onto CNTs vary among different research groups. Fullman *et al.*<sup>131</sup> carried out self-assembly of Au nanocrystals onto CNTs in solution, followed by thermal annealing at 300°C in air for a short period of time. Continuous polycrystalline Au nanowires up to 10 μm in length can be obtained<sup>131</sup>. It was reported that Mo-Ge superconducting nanowires can be successfully fabricated by sputter deposition of the metal material onto CNTs.<sup>132</sup> However, studies by Zhang *et al.*<sup>133</sup> demonstrated that such sputter deposition method only work on a limited number of metals that have strong interaction with the CNT surface. Instead of forming homogeneous coatings on CNTs, some metals (Au, Fe, Al, Pb) form discrete particles on CNTs with sputter deposition method. It was found that by using a buffer layer of Ti, these metals (Au, Fe, Al, Pb) can also form continuous coatings on CNT.<sup>133</sup> Choi and co-workers reported a spontaneous reduction approach to deposit Pt and Au onto CNTs.<sup>134</sup> They found Pt<sup>2+</sup>

and  $\text{Au}^{3+}$  can be reduced on CNT surfaces because the reduction potentials of  $\text{Pt}^{2+}$  and  $\text{Au}^{3+}$  are lower than the Fermi energy of the single-walled CNTs.

DNA and polymer molecules can also serve as templates for metal nanowire fabrication, because both can be very small in diameter and very long in length. One way to make metalized DNA is to simply soak the DNA molecules in a solution containing metal nanoparticles<sup>135,136</sup>. This approach uses electrostatic attraction between the negatively charged DNA backbone and positively charged metal nanoparticle as the driving force. Electroless deposition is another important method to coat the DNA molecules with metal<sup>137-140</sup>. This method usually consists of two steps. First the DNA molecules absorb certain metal cations  $\text{M}_1^+$  in a solution, followed by reduction of these cations to metal atoms  $\text{M}_1^0$ . In the second step, the metal-decorated DNA molecules are put in another metal cation  $\text{M}_2^+$  solution, where the metal atoms  $\text{M}_1^0$  act as catalyst for the reduction of  $\text{M}_2^+$  to  $\text{M}_2^0$  and thus induce growth of a continuous layer of  $\text{M}_2$  on the DNA. Metalizing DNA molecules can also be realized by directly evaporating metal onto suspended DNA molecules in a vacuum environment<sup>141</sup>. Gold nanowires as thin as 10 nm were prepared with this method.<sup>141-143</sup>

There are also some studies of using polymer molecules as positive templates. Poly(2-vinylpyridine) (PVP), for example, was reported to make Pd nanowires on Si or mica surface.<sup>144</sup> PVP was first dissolved in an acidic solution where the polymer chains form a wormlike conformation because of Coulomb repulsion among the charges along the polymer backbones. This conformation was trapped when the polymer molecules were attached to the solid surface (Si or mica).  $\text{Pd}^{2+}$  can then

adsorb to the PVP backbones by ion exchange, and Pd nanowires were obtained by reduction of  $\text{Pd}^{2+}$  to  $\text{Pd}^0$ . A similar approach to make Pd nanowires was also realized with poly(methacryloyloxyethyl dimethylbenzylammonium chloride) molecules.<sup>145</sup> Djalali *et al.* reported fabrication of Au nanowires using core-shell cylindrical polymer brushes as template.<sup>146</sup> The polymer brush contains a PVP core and a polystyrene shell, where Au salt ( $\text{HAuCl}_4$ ) was adsorbed into the PVP core first and then reduced to form Au nanowire.

## 2. Negative templates

Negative templates are usually patterned cylindrical pores in a membrane or just cylindrical tubes. Metal material can be deposited into these cylindrical pores or tubes, and metal nanowires can be obtained after removal of the templates.

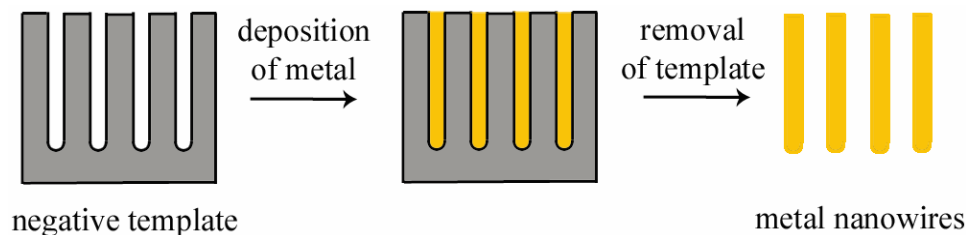


**Figure 55. Fabrication of metal nanowires from a negative template.**

Two most commonly used negative templates are anodic porous alumina and track-etched membranes. The anodic porous alumina technique was first developed in the 1950's by Keller *et al.*<sup>147</sup> High density of nanopores ( $\sim 10^{11}$  pores per  $\text{cm}^2$ ) is achieved by anodizing aluminum films in acidic electrolyte. The diameter and depth of the pore can be controlled by the anodization conditions (time, voltage etc.). With the original one-step anodization method, the pores are not so well ordered, but near perfect, long-range hexagonally patterned pores can be made by pre patterning the Al

surface with array of concaves through mechanical molding process, followed by normal anodization.<sup>148,149</sup> These arrays of concaves will guild the pore development and thus the order of the concaves is preserved. There are several methods of depositing metal into the pores of the anodic porous alumina templates, such as electrochemical deposition, chemical vapor deposition (CVD) and electroless deposition. To date, nanowires of pure metal<sup>150-152</sup>, metal alloy<sup>153-156</sup> and multi-segment<sup>157,158</sup> have been successfully made using anodic porous alumina as templates.

Track-etched membranes also contain large amount of pores in the membrane. These pores come from tracks in the membrane, which were left behind when high energy charged particles pass through the membrane (e.g. mica, polycarbonate film). These tracks can be further developed by selective etching in certain reagents like hydrofluoric acid to make them larger. The final diameter of the pores can be controlled by the etching time. The density of pores ( $\sim 10^9$  pores per  $\text{cm}^2$ ) in these membranes is not as high as those in anodic porous alumina, and they don't have high packing order in general. Nevertheless, metal nanowires can be made from this kind of template with similar deposition techniques, and fabrication of nanowires of pure metal<sup>159-161</sup>, alloy<sup>162</sup> and multi-segment<sup>163,164</sup> have been reported.

Block polymer film can also be a good choice of negative templates to make metal nanowires. The idea comes from phase separation in some block copolymers. Thurn-Albrecht *et al*<sup>165</sup> annealed a polystyrene-b-poly(methyl methacrylate) (PSt-b-PMMA) film under an applied electric field, which induced phase separation in the block polymer film with PMMA cylinder phase hexagonally packed in PSt matrix. The PMMA phase was then decomposed by deep ultraviolet irradiation, and rinsed



away with acetic acid, with porous PSt film left behind. Co and Cu nanowires were then grown in the pores by electrodeposition. Further studies of these Co nanowires revealed interesting properties like anisotropic magnetoresistance and giant magnetoresistance.<sup>166</sup>

Attempts to fill carbon nanotubes (CNT) with metal to form metal nanowires were also studied recently. Pb and Bi were first introduced into CNTs through capillary action<sup>167</sup>, as both metals have low melting points. Different transition metals, such as Ti, Cr and Mn, can also be encapsulated in CNTs by arc-discharge method.<sup>168,169</sup> A one-step chemical vapor deposition (CVD) process to make Fe- and Co-filled CNT was also reported<sup>170,171</sup>, where the metal precursors ( $\text{Fe}(\text{CO})_5$  or  $\text{Co}(\text{CO})_3\text{NO}$ ) serve as source for both the encapsulated metal and carbon nanotube. Metal-filled CNTs can also be synthesized by direct deposition of metal precursors into CNTs from solution or melt phase, followed by subsequent reduction.<sup>172</sup> Due to the small size of CNT, filling CNTs with metal may produce metal nanowires with diameter as small as a few nanometers.

### 3. Surface templates

Step-edges are the most abundant defects on a crystalline surface, and the atoms on the step-edges usually have dangling bonds which make them very reactive. When an alien atom diffuses on the surface, it will bind to one of these atoms on the steps to lower the energy of the whole system. As a result, the step-edges often serve as the nucleation sites during physical vapor deposition (PVD) processes. Under proper conditions, the nucleation and subsequent growth process can be controlled to mainly

occur on the step-edges. This growth method, also called step-flow growth method, has been studied by many research groups to make quasi 1D nanowires.<sup>173-182</sup> This method, however, usually requires high vacuum environment. Moreover, the nanowires thus made adhere to the substrate very well, and usually can't be transplanted to another substrate for further fabrication, which may strongly limit the application of this step-flow growth method.

Recently the Penner group showed that metal nanowires can be selectively grown at the step edges on the surface of highly ordered pyrolytic graphite (HOPG) through electrodeposition. For metals that can form stable conductive oxide, direct electrodeposition is adopted to form continuous nanowires of metal oxide at the step edges of HOPG, and then metal nanowires can be obtained by a subsequent reduction process (Figure 56). For metals that do not form stable conductive oxide, a triple-pulse method (Figure 57) has been developed to form continuous metal nanowires at step edges.

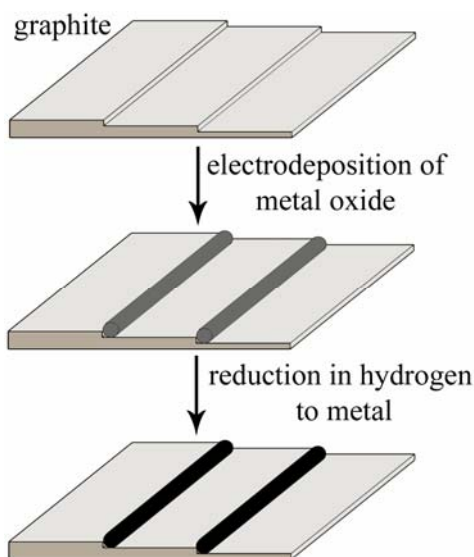


**Figure 56. Illustration of metal nanowires fabricated by electrodeposition of metal oxide nanowires followed by reduction.**

Take Mo nanowire fabrication for example<sup>183,184</sup>. First continuous MoO<sub>2</sub> nanowires were fabricated by electrodeposition from a MoO<sub>4</sub><sup>2-</sup> plating solution. The MoO<sub>2</sub> nanowires were then reduced to Mo nanowires by annealing at 500 °C under a hydrogen atmosphere. Due to the density change from MoO<sub>2</sub> to Mo, the nanowires shrink in diameter after reduction, which was confirmed by SEM images. Cu and Fe nanowires can be prepared similarly, since Cu<sub>2</sub>O and Fe<sub>2</sub>O<sub>3</sub> nanowires can form through electrodeposition first.

Attempts to prepare nanowires of some noble metals (Au, Pt, Ag) by direct deposition from electrolytes failed to produce continuous metal nanowires. Instead, discontinuous nanowires with individual nanoparticles along the step-edges were produced.<sup>185</sup> The reason for not forming continuous nanowires was ascribed to insufficient nucleation centers initially. Thus the triple-pulse method<sup>186</sup> was proposed by Penner group (Figure 57). For the first step, a high oxidation pulse ( $E_{ox}$ ) is applied, which is believed to oxidize the carbon atoms on the step-edges to form functional groups like -C=O and -COOH. The second step involves a large nucleation potential ( $E_{nucl}$ ) pulse to reduce a small amount of metal and nucleate at the step edges. The functional groups on the step-edges have better ability to bind with metal atoms than bare C atoms, which greatly increases the density of nucleation sites along the step-edges. Step three is a normal growth potential ( $E_{grow}$ ), which allows slow growth of the nucleation sites into large particles and further merge into nanowires. With this method, nanowires of Pd, Cu, Ni and Au have been successfully fabricated.<sup>186</sup>

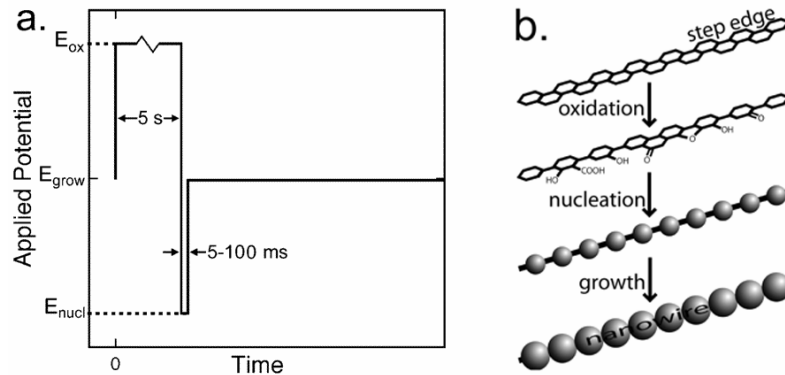


**Figure 57. Triple-pulse method for nanowire growth.<sup>186</sup> (a) pulse diagram, (b) proposed mechanism.**

Template assisted methods for metal nanowire growth have attracted increasing interests among researchers. Of the three template assisted methods, negative template method is the most popular one. One big advantage of this method is the maturity of negative template fabrication, especially the anodic porous alumina and polycarbonate porous membranes. These two porous membranes with various pore sizes are commercially available. The second advantage lies in the fact that the nanowire size (diameter) is controlled by the pore size of the template. Finally, the high density of pores in the membranes allows the fabrication of large quantities of metal nanowires at the same time. In contrast, the fabrication of positive templates is far from maturity. Many reported methods include one step to deposit dispersed CNTs, DNA or polymer molecules onto certain substrate like mica or Si<sup>134,135,137</sup>, which result in both low density and poor order of the template molecules and subsequent metal nanowires. Direct PVD deposition of metal onto CNTs or DNA molecules also requires fabrication of suspended CNTs or DNA molecules first, which means only limited number of metal nanowires can be produced at the same time<sup>132,133,141-143</sup>.

Surface step-edge template method is relatively new among the three template methods. Although it also suffers from low density of metal nanowires that can be fabricated on the substrate due to the low density of step-edges on the surface, this method, especially after the discovery of using HOPG as template, has demonstrated some advantages over the positive and negative template methods. First of all, the metal nanowires that are made from the other two template methods are usually shorter than 20  $\mu\text{m}$ . The length of metal nanowires is limited by the dimension of the templates, such as the length of template CNTs/DNA and the thickness of the anodic porous alumina membrane. However, the step-edges on HOPG can be much longer, so theoretically, longer nanowires can be fabricated by surface step-edge template. In fact, metal nanowires with length of 500  $\mu\text{m}$  or even longer have been fabricated on HOPG.<sup>184,187</sup> Second, the Van der Waals interaction between the metal nanowires and the HOPG substrate is believed to be quite weak, thus the metal nanowires can be more easily removed. This unique property can greatly facilitate post fabrication of the metal nanowires in practical applications. For instance, a convenient process of making  $\text{H}_2$  sensors from Pd nanowires has been described<sup>119</sup>, where the Pd nanowires were removed from the HOPG surface with the help of a cyanoacrylate film (super glue), followed by deposition of two silver electrodes. The sensors thus made showed some interesting properties, including fast response time, very small power consumption and resistance to reactive gases such as  $\text{O}_2$  and  $\text{CO}_2$ .

## **4.2 Growth of Pd nanowires on HOPG from a Cu sacrificial film.**

### **4.2.1 Motivation.**

Dryfe and coworkers<sup>188</sup> reported growth of metal nanowires and nanoparticles on HOPG by galvanic displacement, where metal ions in the dilute electrolyte solution were reduced through the coupled oxidation of insoluble crystals of a ferrocene derivative, i.e. n-butyl ferrocene (*n*Bu-Fc) or decamethyl ferrocene ( $\text{Cp}^* \text{Fe}$ ,  $\text{Cp}^* = \eta^5\text{-C}_5\text{Me}_5$ ), on the HOPG substrate. Compared with other fabrication methods, such as the triple-pulse growth method, this one-step method with galvanic displacement greatly simplifies the process to make metal nanowires. One challenge for researchers in nanoelectronics is how to make desired nanostructures or devices reproducibly and cost-effective. The galvanic displacement method provides a cheap and reproducible way for metal nanowire fabrication. Furthermore, the simplicity of this method can also find application in large scale production of nanowires, which can be essential for future commercialization of products from metal nanowires.

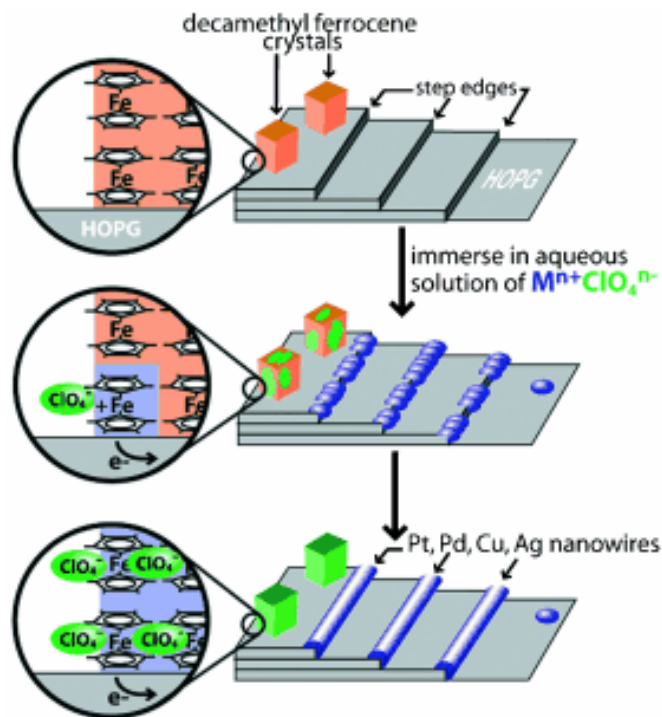


**Figure 58. Proposed mechanism of galvanic displacement method for metal nanowire fabrication. Reproduced from Dryfe's paper<sup>188</sup>, with permission; copyright 2004, Wiley-VCH Verlag GmbH & Co. KGaA.**

Figure 58 illustrates the mechanism proposed by Dryfe *et al.* In their experiments, drops of *n*-butyl ferrocene or decamethyl ferrocene solution in 1,2-dichloroethane (DCE) were deposited onto HOPG surface and dried first. The spontaneous deposition of metal nanowires was carried out by immersion of the ferrocene derivative modified HOPG into electrolyte solution that contains certain metal ions. Because metals like Au and Pt have higher standard reduction potentials than *n*Bu-Fc and  $Cp^*_2Fe$  (Table 2), the ferrocene derivative crystals on the HOPG surface will get oxidized while metal ions get reduced. The charge flow was believed to happen through the graphite layers. The reduced metal atoms will selectively nucleate at the defect sites (step edges and surface point defects) and further grow

into larger structures. The growth continues until all *n*Bu-Fc or Cp\*<sub>2</sub>Fe crystals are oxidized.

Reduction half-reaction	E°/V (vs NHE)
$\text{Cp}^*_2\text{Fe}^+ + \text{e}^- \rightarrow \text{Cp}^*_2\text{Fe}$	0.07
$n\text{Bu-Fc}^+ + \text{e}^- \rightarrow n\text{Bu-Fc}$	0.56
$\text{Cu}^{2+} + 2\text{e}^- \rightarrow \text{Cu}$	0.34
$\text{PdCl}_4^{2-} + 2\text{e}^- \rightarrow \text{Pd} + 4\text{Cl}^-$	0.64
$\text{Ag}^+ + \text{e}^- \rightarrow \text{Ag}$	0.80
$\text{AuCl}_4^- + 3\text{e}^- \rightarrow \text{Au} + 4\text{Cl}^-$	1.00
$\text{PtCl}_4^{2-} + 2\text{e}^- \rightarrow \text{Pt} + 4\text{Cl}^-$	0.76

**Table 2. Standard reduction potentials of some metals and ferrocene derivatives.**<sup>188,189</sup>

Interestingly, it seems that this galvanic displacement method doesn't agree with the theory for the triple-pulse method proposed by Walter *et al.*<sup>186</sup> In fact, the galvanic displacement method is very similar to direct deposition method that used to deposit MoO<sub>2</sub> nanowires on HOPG.<sup>183,184</sup> The difference lies in the fact that the deposition potential is driven by a potentiostat in direct deposition method, while in galvanic displacement method the deposition potential is provided by the reduction potential of the ferrocene derivatives. Walter *et al.* claimed that the direct deposition method didn't work for the nanowire fabrication of noble metals like Pd, Ag and Au, because the density of nuclei along the step edges is too low for continuous nanowire preparation. The problem was solved by the triple-pulse method, in which the first two pulses E<sub>ox</sub> and E<sub>nucl</sub> were purposely introduced to increase the nuclei density on the step edges. There are no such pulses used in the galvanic displacement method,



where the reduction potential of ferrocene derivative is the only driving force during the whole process. So how can the problem of low nuclei density along step-edges be solved in the galvanic displacement method?

One possible reason is that the reduction potential may vary during the deposition process. The oxidation of ferrocene derivative is a heterogeneous reaction which involves mass transfer. Take  $\text{Cp}^*_2\text{Fe}$  for example, the oxidation reaction  $\text{Cp}^*_2\text{Fe} \rightarrow \text{e}^- + \text{Cp}^*_2\text{Fe}^+$  generates  $\text{Cp}^*_2\text{Fe}^+$  cations, which require counter ions to neutralize them. Thus the counter ions need to diffuse from the electrolyte solution to the cations generated inside the insoluble crystals. Such diffusion can be easier at beginning when the cations are generated near the surface of the crystal, and become much harder when counter ions need to diffuse deep into the crystal. Thus it's highly possible that the driving force for the oxidation reaction of  $\text{Cp}^*_2\text{Fe}$  tend to be high (lower reduction potential) at the beginning and become lower (higher reduction potential) very quickly. One proof is the transient current vs time plot during the deposition process. The experiments were conducted by Dryfe *et al.* using a two-compartment cell in which two HOPG electrodes, connected by a copper wire, were immersed in separate half-cells, which contained different electrolytes. The two half-cells were connected by a salt bridge. With this set-up, the oxidation of ferrocene derivative and the reduction of metal ions took place in separate half-cells, and the electron transfer could be monitored and recorded. The transient current vs time plot demonstrated that usually the current was high initially and then decreased rapidly, which indicates the driving force (reduction potential of the ferrocene derivatives) changed from large (low reduction potential) to small (high reduction potential) very

fast. Thus the initial low reduction potential acts similarly to  $E_{\text{nucl}}$  in the triple-pulse method, which generates lots of nuclei along the step edges, while the reduction potential becomes small quickly and acts like  $E_{\text{grow}}$  for further particle growth. The minimum width of the metal nanowires from this galvanic displacement method was reported to be 200nm, which is much larger than that from triple-pulse method (~60 nm). This is probably due to lack of pretreatment of  $E_{\text{ox}}$  with HOPG in the galvanic displacement method, which result in lower density of nuclei along step edges than the triple-pulse method. So on average each nanoparticle has to grow larger before it can merge with adjacent particles.

Nevertheless, the galvanic displacement method opens the door of fabricating metal nanowires from macroscopic organometallic compound solids in a simple one-step process. Potentially nanowires from a wider range of metals can be prepared with the same method. Different reduction potentials can be achieved by modifying the substituents on ferrocene, or just synthesizing new organometallic molecules. On the other hand, it is well know in general chemistry that galvanic displacement can take place between two metals. For example, putting an iron wire in an aqueous  $\text{CuCl}_2$  solution can result in deposition of Cu onto the iron wire. So instead of spending time and effort in synthesis of new organometallic molecules, can we use some cheaper and more readily available metals in preparation of nanowires? We will try to explore such possibility in the rest of this chapter. Theoretically a metal with lower reduction potential can be used as reducing agent for another metal with higher reduction potential. However, the process of making nanowires of one metal from another sacrificial metal can be quite complicated, since such process is kinetically controlled

and can be affected by many factors, such as the choice of metals, the type and concentration of the electrolyte, etc.

#### **4.2.2 Preparing Pd nanowires from Cu sacrificial films.**

Pd and Cu were the first pair of metals chosen for the attempts of nanowire fabrication on HOPG. There are several reasons for choosing Pd and Cu. First of all, the difference between the standard potentials of these two metals (0.64 V for Pd and 0.34 V for Cu, according to Table 2) is fairly large. If the difference is too large, there could be too many nuclei on the basal planes other than the step edges<sup>185</sup>. But it is also not desirable if the difference is too small, because that would cause low nuclei density on the step edges, which is not desired for nanowire growth. Secondly, Pd nuclei are well known for their catalytic activity and thus widely used in electroless deposition for other metals. Such property may also benefit the Pd nanoparticle growth and the subsequent formation of Pd nanowires. Finally, Cu is commonly used in industry and can be obtained at fairly low cost. The unique color of Cu can also make it easier to monitor the displacement reaction visually.

The experimental procedure can be found in the experimental section. Briefly, a thin layer of Cu was first deposited on one side of a piece of HOPG, and then the HOPG piece was immersed in Pd(OAc)<sub>2</sub>/HCl mixture solution where the displacement reaction and Pd nanostructure growth would take place. The deposition of Cu film was achieved by electroless deposition method. First, a freshly peeled piece of HOPG was soaked in a Pd(OAc)<sub>2</sub>/HCl mixture solution for 1 min, then it was rinsed with deionized water and dried in air. The purpose of this step is to adsorb trace amount of Pd compound onto the HOPG surface. Then the HOPG piece was

immersed in Cu plating solution (mixture of  $\text{CuSO}_4$ ,  $\text{NaOH}$ , sodium potassium tartrate, and formaldehyde) for 5 min, during which the Pd compound was first reduced to  $\text{Pd}^0$  and then acted as catalyst for reduction of  $\text{Cu}^{2+}$  to  $\text{Cu}^0$ . A purple red Cu film would grow around the whole HOPG piece after this electroless deposition process. The top and bottom surfaces were peeled with Scotch<sup>TM</sup> tape to give fresh HOPG surface for Pd nanostructure growth. The Cu on the three sides of the HOPG piece was also removed with the help of a piece of sand paper, leaving only one HOPG side with Cu film, which was found to be enough quantity of Cu for the next replacement reaction step. The piece was then immersed in  $\text{Pd}(\text{OAc})_2/\text{HCl}$  mixture solution for 5min for the growth of Pd nanostructures and then rinsed with deionized water. The proposed mechanism was shown in Figure 59.

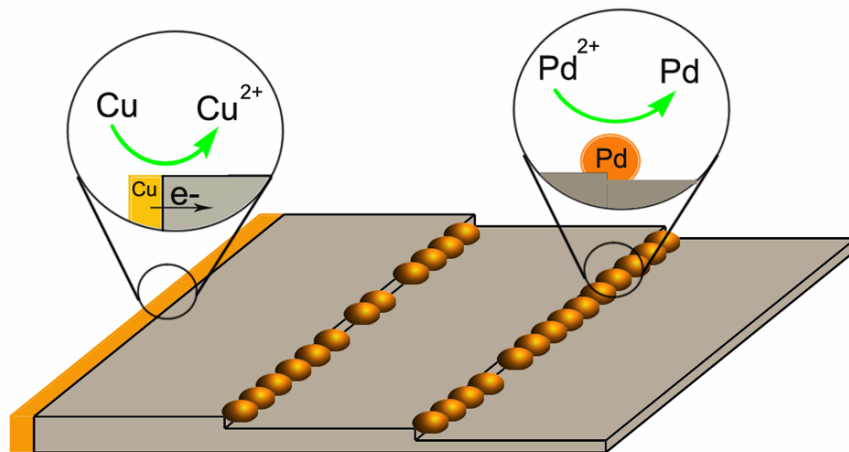


**Figure 59. Proposed mechanism for growth of Pd nanowire from the sacrificial Cu film on the edge.**

The morphology and structure of the synthesized nanoparticles and nanowires were characterized by tapping mode AFM (Digital Instruments, multimode) and SEM (Hitachi S-4700). Figure 60(a) shows an SEM image of the HOPG sample surface. A large quantity of wires with length up to  $10\mu\text{m}$  can be clearly seen. Further

examination shows that each wire is made up of small grains (Figure 60(b)) with width around 100nm. We also observed particles on basal planes of HOPG, which we believe is caused by nucleation on the defect sites on the surface. The AFM images reveals similar morphology of Pd nanostructures on the HOPG surface (Figure 61(a) and 61(b)), but we can not resolve the grain structure in the wire due to the convolution of the AFM tip.

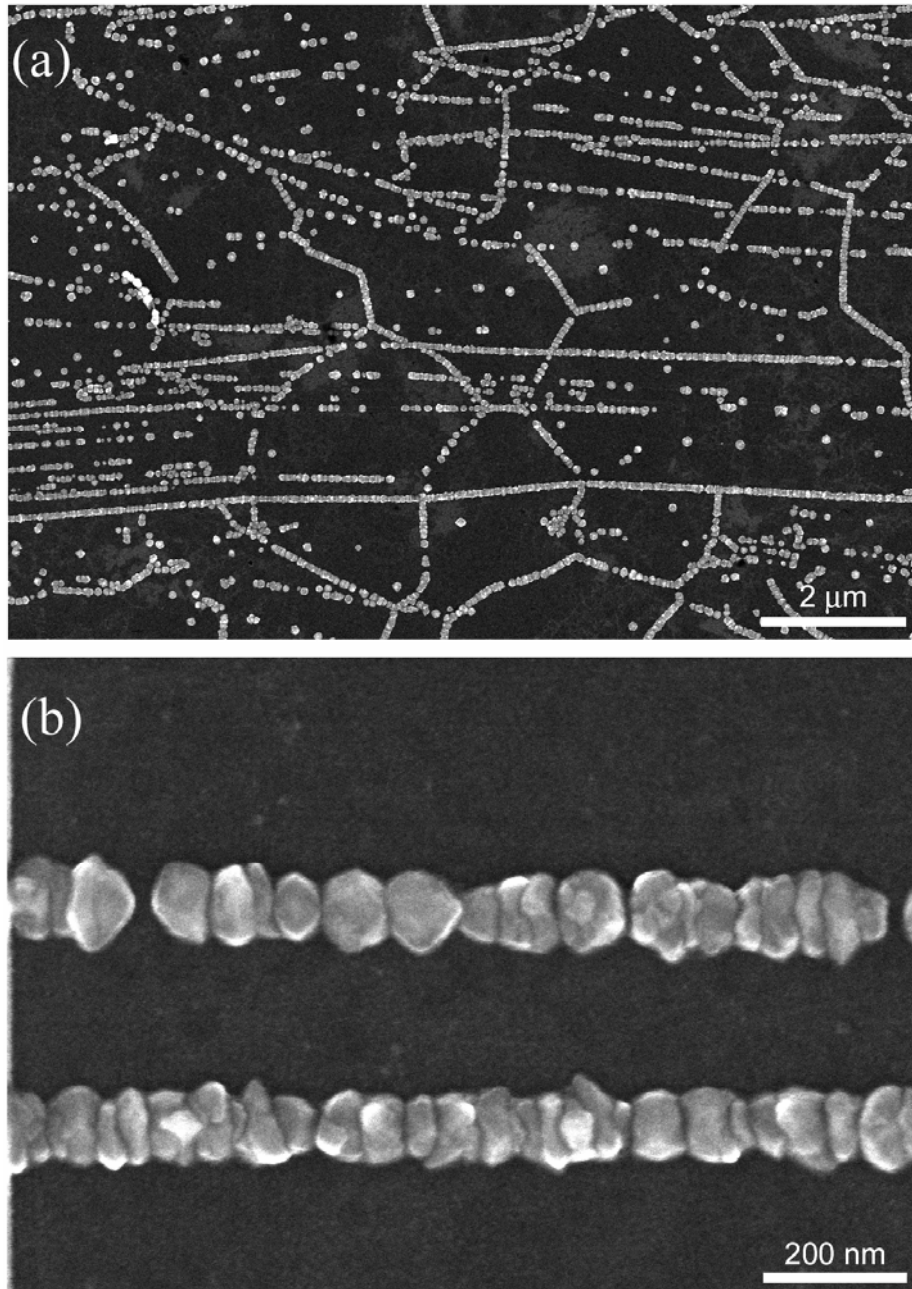


Figure 60. SEM images of Pd nanostructures on HOPG.

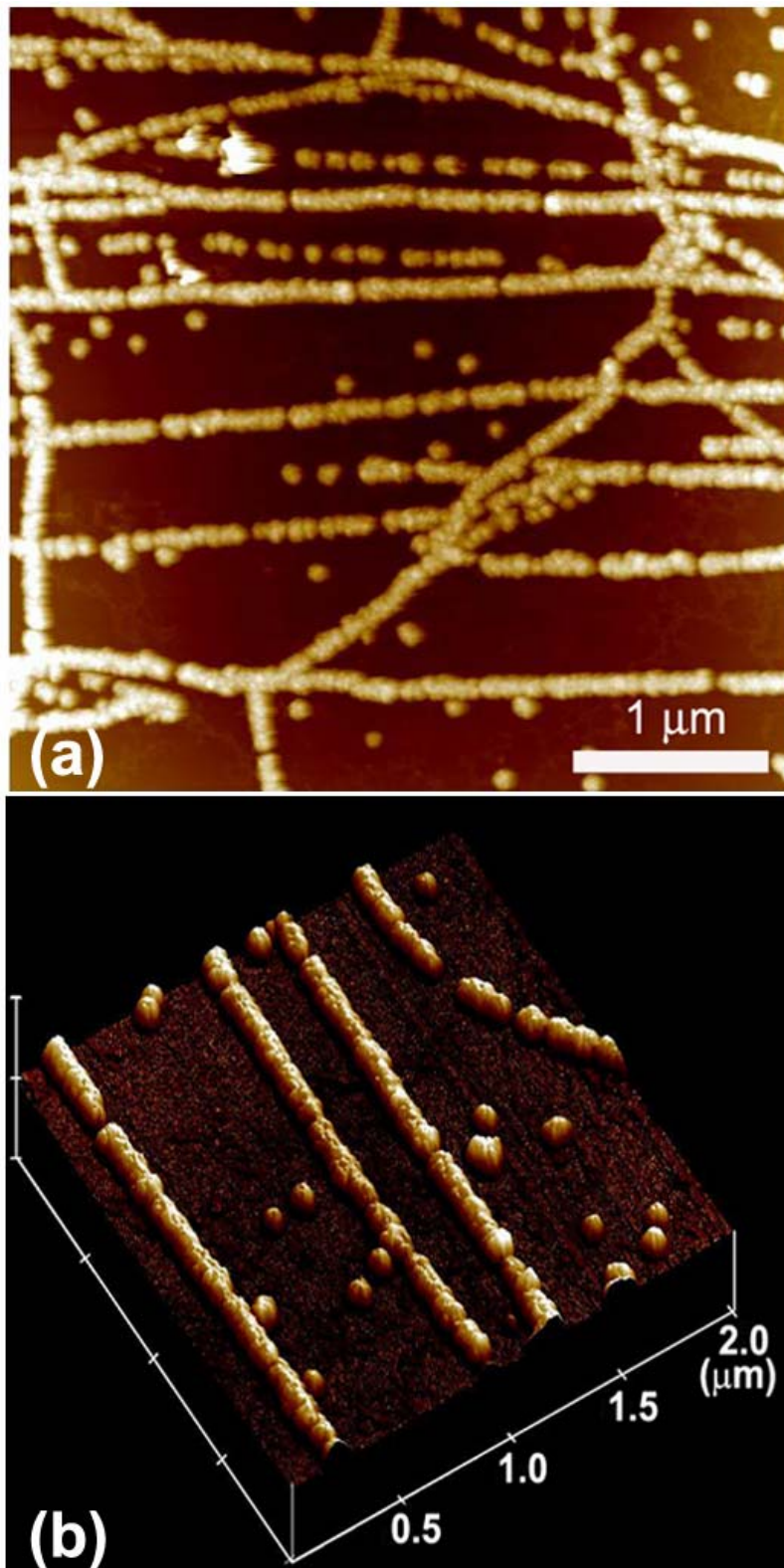
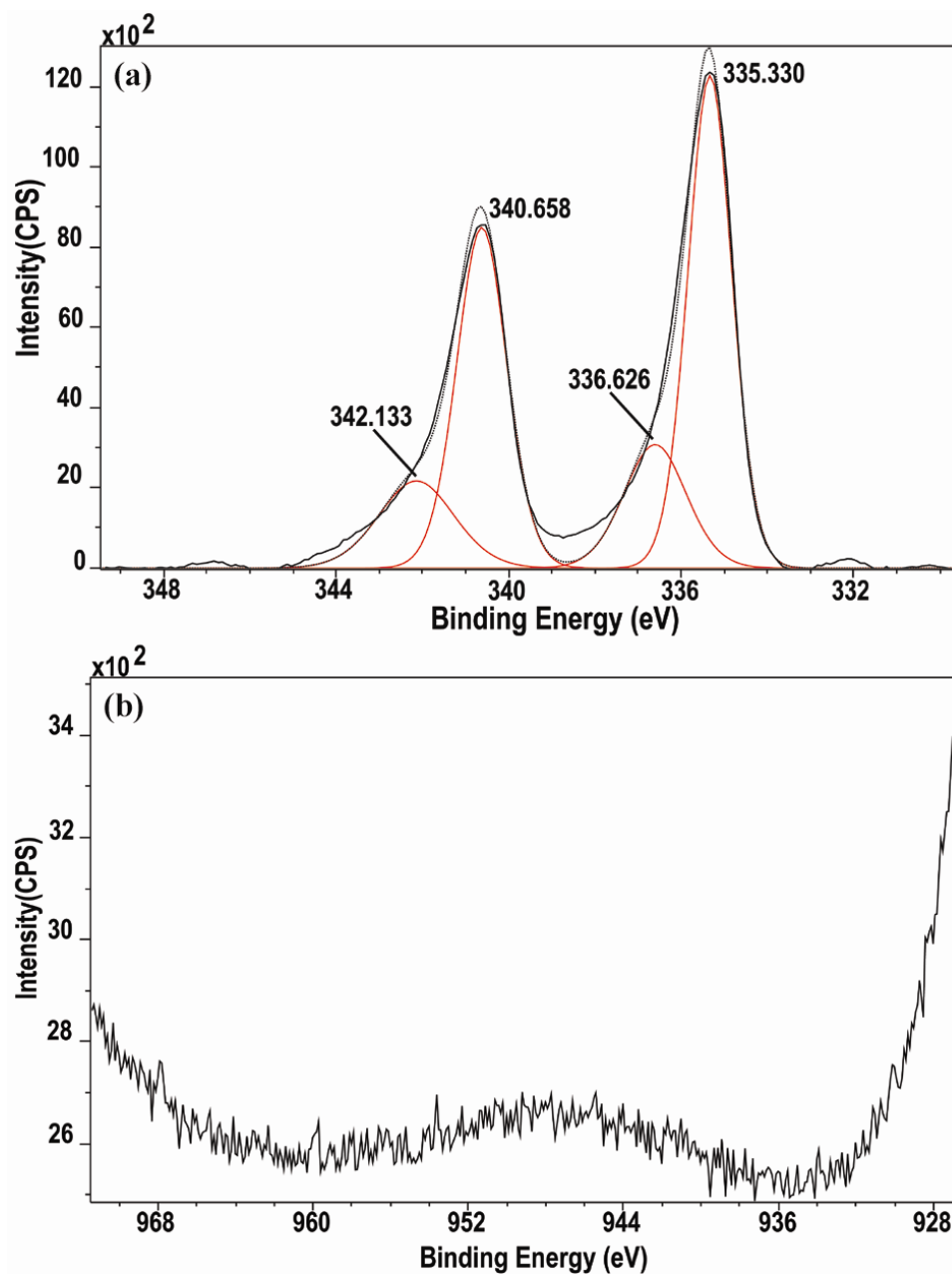


Figure 61. TM-AFM images of Pd nanostructures on HOPG.

XPS was used to identify the actual composition of the nanoparticles and wires. Figure 62(a) shows strong peaks of Pd species. Two species of Pd can be identified, as we saw two sets of Pd  $3d_{5/2}$  and  $3d_{3/2}$  peaks. The one set with binding energy (BE) at 335.330 eV and 340.658 eV are typical peaks of Pd(0), while the other set with BE at 336.626 eV and 342.133 eV corresponds to Pd(II) species, probably from the oxidation of Pd nanoparticles upon exposure to air. The curve fitting of the spectrum shows around 73% of Pd on the surface is Pd(0). The fact that we did not see any strong Cu peaks (Figure 62(b)) in the typical BE range of Cu (930-955 eV for Cu  $2p_{1/2}$  and  $2p_{3/2}$ ) also supports the mechanism in Figure 59.





**Figure 62. XPS spectra for (a) Pd and (b) Cu analysis.**

The XPS spectra and the SEM, AFM images demonstrated that we have successfully fabricated Pd nanowires on HOPG surfaces. The method is simple, fast and reproducible. The grainy structure on the nanowire surface agrees with the proposed mechanism that the nanowires came from metal nanoparticles merging

together. However, more studies need to be done to verify the proposed mechanism. Also, some important questions came up naturally ever since our first successful attempt of Pd nanowire fabrication, such as whether the nanowire size can be controlled through certain parameter, and whether this method can be applied to other metals such as Au and Ag. These issues will be discussed in the following sections.

#### **4.2.3 Further mechanistic study of Pd nanowire formation.**

In the proposed mechanism, the formation of Pd nanowires takes place via the coupling oxidation of Cu film. The reaction of Cu film can be observed by the change of the color. The Cu film was originally purple red, and this characteristic color disappeared completely after immersion in the Pd(OAc)<sub>2</sub>/HCl mixture solution. Usually some silver-ish metallic color can be seen in the place where the Cu film was initially deposited, which we believe is because some Pd deposited on the side. Such color change was only observed on the Cu film side and no silver-ish color was visible on the other three sides where no Cu film was deposited at first, indicating the presence of Cu film can also induce the deposition of Pd, probably because the Cu-Pd interaction is quite strong so that Pd can nucleate on Cu film and grow.

A comparison experiment was also conducted to show that the deposition of Pd nanowires was driven by oxidation of Cu film. A bare HOPG sample was immersed into the same Pd(OAc)<sub>2</sub>/HCl mixture solution for 5 min and then examined by AFM. No particles or wires were observed on the HOPG surface, just as expected.

It is proposed that these Pd nanowires mainly formed on the step edges of graphite surface. We tried to confirm this idea by AFM images but turned out not very successful. The main reason is that most step edges are only one or a few layers

thick. Considering the distance between adjacent graphite layers is only  $3.35\text{\AA}$ , most step edges are no higher than 1 nm, and such features can be covered by noise when the AFM tip was scanning over a sample surface with lots of high features (the height of the nanoparticles and nanowires are mostly larger than 30 nm). One solution is to image some tall step edges together with Pd nanoparticles or nanowires on them. It turned out difficult to use AFM to search for these tall step edges, mainly due to the slow scan speed and limited scan size (maximum  $14\ \mu\text{m} \times 14\ \mu\text{m}$  with a “J” scanner) for AFM. On the other hand, SEM turned out to be suitable for such task with its high imaging speed and variable scan size, although its sensitivity in z direction is not as good as AFM. Figure 63 is a SEM image where multiple Pd nanoparticles formed along one tall step edge. We saw no nanoparticles on the basal plane in the SEM image, which suggests that the step edge is indeed preferred during the nucleation stage.

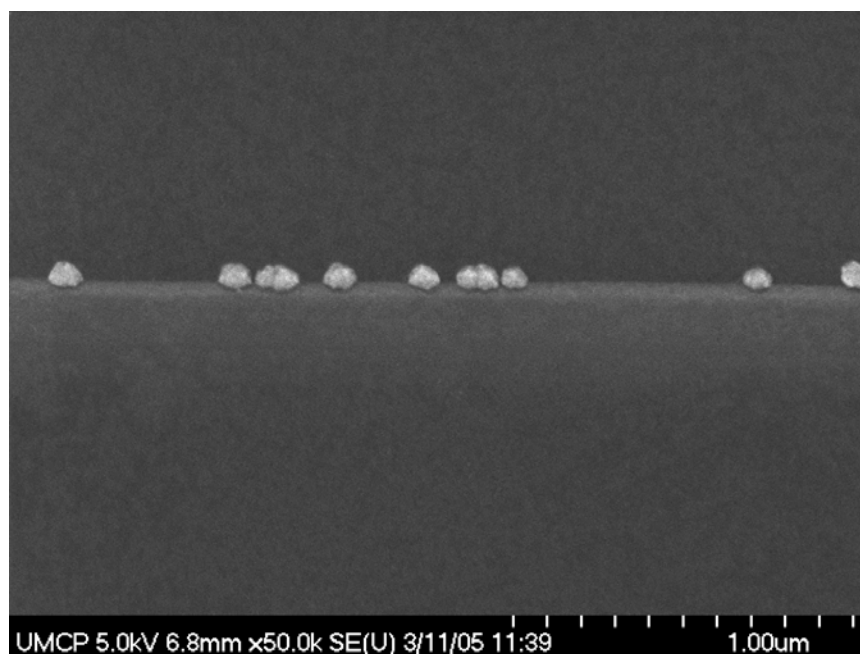


**Figure 63. SEM image of Pd nanoparticles at step edges on HOPG.**

Another experiment was designed to demonstrate the preferential deposition of Pd nanoparticles or nanowires at step edges on HOPG. Normal peeling method with Scotch™ tapes usually generates linear step edges on the surface, but it is well known that thermal oxidation method can produce monolayer-deep pits with circular step edges.<sup>190-192</sup> If the proposed mechanism is true and Pd nanowires form at the step-edges, the Pd nanowires should also deposit at these monatomic pits and form loop-like structures (Figure 64).

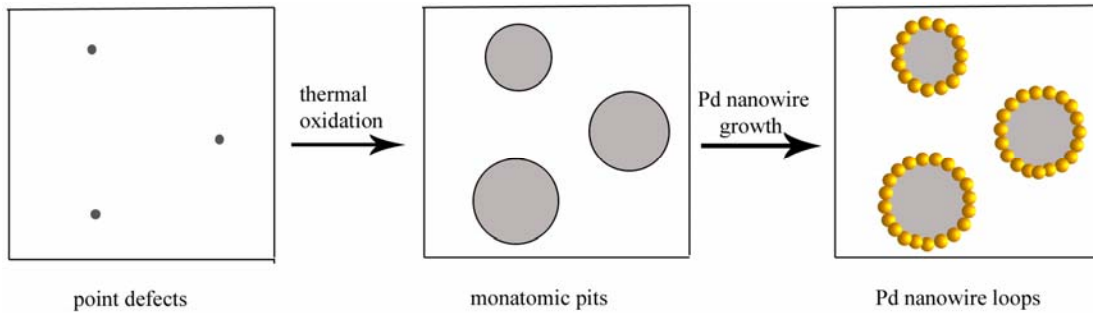


**Figure 64. Schematic illustration of formation of Pd nanowire loops on HOPG surface**

The monatomic pits are believed to initiate from defects on the basal plane, such as vacancy defects where one or a few carbon atoms are missing from the graphite lattice plane. The carbon atoms around a vacancy defect have dangling bonds and are thus more reactive than other carbon atoms. Under proper conditions, they can react with oxygen and get etched away from the lattice plane, and the defect grows larger as such oxidation process continues. As there are no covalent bonds between adjacent graphite layers, the etching tends to occur in the same graphite layer, which results in the formation of monatomic pits. The average pit diameter  $d$  can be estimated by the following formula<sup>190</sup>

$$d = C e^{-E_a/RT} p_{O_2} t \quad (13)$$

where  $R$  is the gas constant,  $T$  is temperature,  $p_{O_2}$  is the partial pressure of oxygen,  $t$  is the reaction time and  $E_a = 1.27 \times 10^5 \text{ J mol}^{-1}$  is the activation energy of  $O_2$  etching reaction.  $C$  is a constant that is found to be dependent on pit density on the surface<sup>193</sup>.  $C = 2 \times 10^4 \text{ nm mbar}^{-1} \text{ s}^{-1}$  for pit density of  $1 \text{ pit } \mu\text{m}^{-1}$ , which is close to the pit density on our HOPG samples (ZYB grade, MikroMasch).

For the test experiment, Cu film was deposited on one side of HOPG first, followed by heating the HOPG sample in a vacuum oven at  $120 \text{ }^\circ\text{C}$  for 18 hours to develop the monatomic pits on the surface. The sample was then immersed in  $\text{Pd}(\text{OAc})_2/\text{HCl}$  mixture solution for nanowire growth. Figure 65 is an AFM image of the sample surface with Pd nanowires. The loop-like structure can clearly be seen in the image (as pointed out with green arrows) along with linear nanowires. The Pd nanowire loops in Figure 65 are not perfectly circular, and their sizes vary a lot. One possible reason is that the monatomic pits spread randomly on the surface, and some of the pits merge together during the oxygen etching growth process. However, these results give strong evidence that the Pd nanowire growth occurs preferentially at the step edges on HOPG surface. This experiment also demonstrates that Pd nanowires with loop-like shape can be fabricated with galvanic displacement method with the sacrificial Cu film. Although similar loop-like metal nanostructure has been fabricated with PVD methods<sup>192</sup>, our approach can be performed without the use of high vacuum instruments.

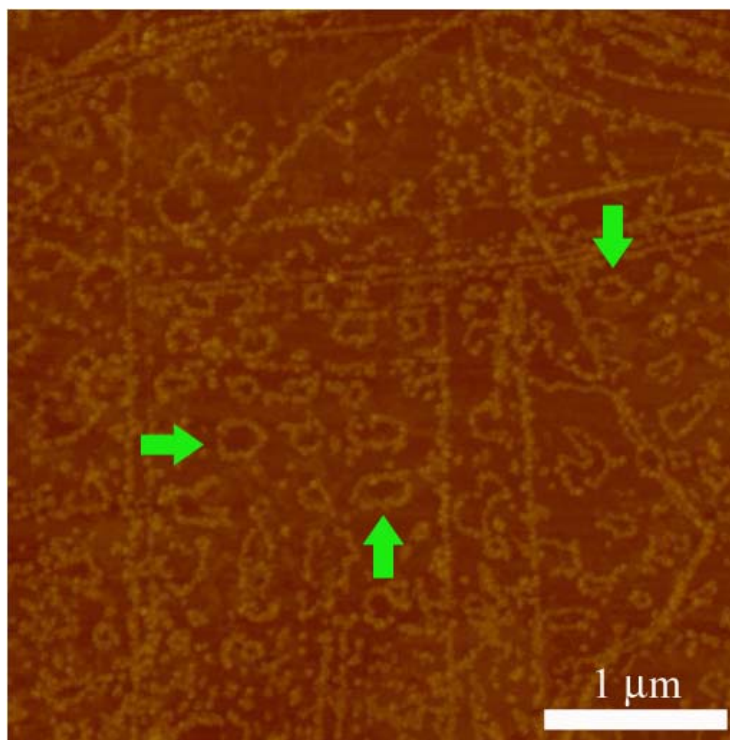


**Figure 65. Pd nanowire loops that formed around monatomic pits on HOPG.**

#### **4.2.4 Size control of the Pd nanowires**

In the proposed mechanism, the total amount of Pd that gets reduced from the electrolyte is quantitatively proportional to the amount of Cu initially deposited on the side of HOPG sample, according to the galvanic replacement reaction  $\text{PdCl}_4^{2-} + \text{Cu} \rightarrow \text{Pd} + \text{Cu}^{2+} + 4\text{Cl}^-$ . The Pd nanowire growth will stop once Cu is completely consumed. Thus the diameter of the Pd nanowire should also be proportional to the amount of Cu used in the experiment, which suggests that the size control of the Pd nanowires can be achieved by controlling the Cu amount.

There are other factors that will affect the final size of the Pd nanowires. The first is the total length of step edges on the sample surface, which determines the total number of nuclei that can form during the initial nucleation phase. As for the same

amount of Cu used, the more Pd nuclei that form on the sample surface, the smaller the final diameter of each Pd nanoparticle and nanowire will be. However, with our current method to generate fresh surfaces of HOPG, the number of step edges is unknown and thus uncontrollable. On the other hand, it is reasonable to assume that the total length of step edges remains relatively constant, or varies in a small range for each HOPG sample. The second factor is the density of defects on the basal planes of HOPG. These defects, mainly vacancy defects, can also be the preferential sites for nucleation and growth of Pd nanoparticles. We assume that for the same HOPG sample, the density of such defects is statistically constant. With these two factors in mind, we decided that the control experiments should be conducted on the same HOPG sample.

In the original experimental setup, Cu plating solution was used to get the side of HOPG coated with Cu. Though it is simple and fast, it is almost impossible to measure the exact amount of Cu that has been deposited on the side. Thus vacuum evaporation was tried out to coat the side with Cu. By controlling the thickness of the Cu film and measuring the side area, we can calculate the amount of Cu deposited on the side and thus the effect of amount of Cu on the morphology of the Pd nanostructure can be evaluated. Figure 66 shows the results of evaporating (a) 5nm-thick and (b) 20 nm-thick Cu film on one side (0.7mm×9.7mm) of HOPG, followed by immersing the piece in Pd(OAc)<sub>2</sub>/HCl mixture solution for Pd nanostructure growth. Nanowires could be observed in both images, but the wires seem not as continuous as those in Figure 60. The reason is believed to be the low nuclei density along the step edges. As shown in the discussion about the results of Dryfe et al., the

nature of galvanic displacement method results in lower nuclei density along step edges compared with the triple-pulse method. So the nanoparticles have to grow big enough to merge with each other and form continuous nanowires. On the other hand, the average diameter of nanoparticles and nanowires (~60 nm) in Figure 66(b) is much larger than that in figure 66(a) (~20 nm), which showed the direct influence of amount of Cu on the size of obtained Pd nanoparticle and nanowires. If we assume the total number of nuclei remained the same in both experiments, we can infer that final diameter of Pd nanostructures  $d$  is dependent on the thickness  $D$  of Cu film in that  $d \propto D^{1/3}$ . Thus the diameter of Pd nanostructures from the 20-nm-thick Cu film should be around 1.6 times as large as that from the 5-nm-thick Cu film. The results from the SEM images showed the former is almost 3 times as large as the latter. The difference between the experimental result and the predicted value may come from the possible oxidation of the Cu film in our experiments. Such oxidation could take place when the chamber of the vacuum evaporator was vented with air and when the sample was transferred from one place to another. Cu film with thickness in the nanometer scale can be very reactive and may get oxidized fast, which may cause the real ratio of Cu amount between the two control experiments to be larger than the expected 4:1 (20 nm : 5 nm).



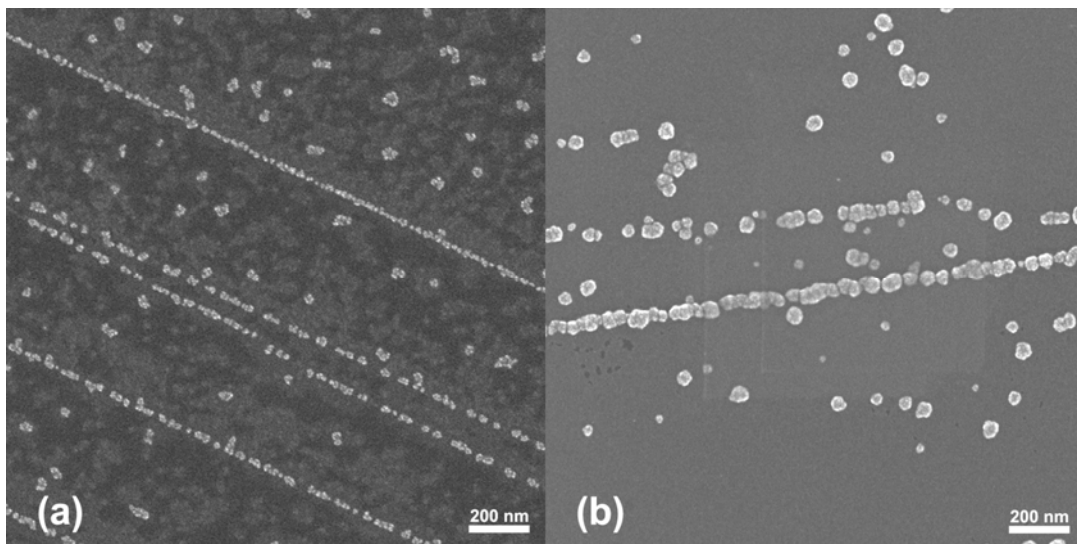


**Figure 66. SEM images of Pd nanowires from Cu films with thickness of (a) 5 nm, (b) 20 nm.**

In short, the comparison experiments here demonstrated that diameter of the Pd nanoparticles/nanowires does depend on the amount of Cu deposited on the side of HOPG sample. Thus varying the amount of Cu should be a convenient way to control the size of Pd nanostructure. However, due to the nature of low nuclei density along step edges with this galvanic displacement method, there seems to be a minimum of Pd nanowire diameter (some value between 60 and 100 nm) in order that the nanowires will be continuous. The exact relationship between the size of Pd nanostructures and the Cu amount couldn't be verified with current comparison experiments because of the possible oxidation of Cu film by ambient oxygen was not excluded. More strict environmental control should be adopted in the future for such comparison experiments.

#### **4.2.5 Galvanic displacement method for other metals**

From Table 2, the three noble metals, Au, Ag and Pt, all have higher standard reduction potentials than Pd, so galvanic displacement reactions can also take place

between any of these three metals and Cu. Thus it is natural to ask whether the galvanic displacement method can also be applied to fabricate nanowires of Au, Ag or Pt. Such attempts were carried out with similar procedures to Pd nanowire fabrication. The electrolyte solutions were 0.1 M  $\text{AgNO}_3$ , 0.1 M  $\text{HAuCl}_4$  and 0.1 M  $\text{H}_2\text{PtCl}_4$ , respectively. Figure 67 showed AFM images of the sample surfaces after immersion of the Cu coated HOPG samples into the corresponding electrolyte solutions for nanowire growth and the following cleaning process. Very few particles (bright spots) can be observed on all three sample surfaces, and the step edges of the HOPG substrate are clearly visible in each image. But no nanowires can be seen on the surface in these images, indicating no nanowires were formed during the experiments. On the other hand, we noticed the color change on the side where Cu film was initially deposited. The color changed from purple red to silver for the Ag and Pt attempts, and from purple red to yellow for the Au attempt. Such color change showed that galvanic replacement reactions did occur, and metals of Ag, Au and Pt did get reduced from the electrolyte solutions. But the AFM images illustrated that the replacement reactions and deposition of the noble metals only took place at the side where Cu film was deposited, not on the basal planes of the graphite samples, which is very different from the Pd nanowire fabrication process.

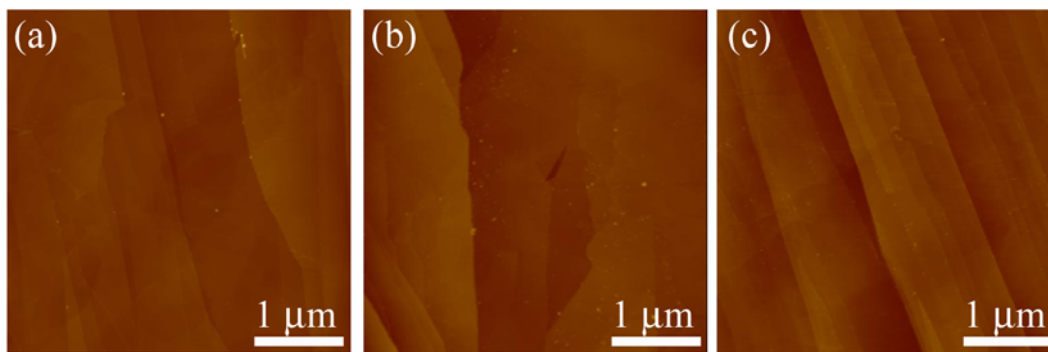


**Figure 67. AFM images of HOPG surfaces in attempts of nanowire fabrication of (a) Ag, (b) Au, (c) Pt**

In our proposed mechanism of Pd nanowire growth, Cu atoms get oxidized to  $\text{Cu}^{2+}$ , and reduction reaction of Pd complex ion takes place on the graphite surface. The reason that these two reactions can occur at different positions is that HOPG is a good conductor and charges like electrons can flow through the bulk graphite. The whole process may take place in a concerted fashion, and our experimental results supported such mechanism. However, besides the graphite surface, the reduction reaction of Pd complex ions may also occur on the Cu film surface. The color change of the Cu film that was observed during the experiments indicates the Pd deposition at where Cu film was grown initially. Thus during the Pd nanowire growth, the Pd deposition takes place both on the graphite surface and the Cu film surface. But in the cases of Ag, Au and Pt, the AFM images and the color changes of the Cu films suggested that the deposition process (or the reduction reactions of these metal precursors) mostly happens on the Cu film. So far we don't know the exact reasons yet. Maybe the binding energy (BE) between Pd atoms and the step edge sites is comparable to the BE between Pd atoms and Cu surface, while BE between Ag, Au or Pt atoms and the step edge sites is much smaller than that between these noble

metal atoms and Cu surface, which means the Cu surface is energetically more favorable for the deposition of Ag, Au and Pt compared with the graphite surface. Another possibility is that the step edge sites have much higher activation energy for the reduction reactions of Ag, Au and Pt precursors than the Cu surface, thus the Cu surface is kinetically more favorable for the deposition of these three noble metals.

### **4.3 conclusion and future plans**

With the galvanic displacement method, we have successfully fabricated Pd nanowires on HOPG surface with the coupling oxidation of Cu films. The morphology and composition of the nanowires were characterized by SEM, AFM and XPS. We proposed a growth mechanism which is similar to the one described by Dryfe *et al.* Specifically, upon exposure to the electrolyte containing Pd precursors, the Cu atoms get oxidized to  $\text{Cu}^{2+}$ , coupled with the reduction of Pd complex ions into Pd atoms on the graphite surface. Pd atoms preferentially nucleate on the step edges of HOPG and grow into nanoparticles. Pd nanowires will subsequently form when these Pd nanoparticles grow large enough to merge with adjacent ones. This mechanism is supported by the experimental results. First, no Pd nanowires were obtained without the sacrificial Cu film, and the size (outer diameter) of the Pd nanowires is strongly dependent on the amount of Cu deposited on the side of HOPG sample. Second, SEM images illustrated grainy morphology on the nanowire surfaces, indicating these nanowires started from multiple nuclei, grew and then merged together. Third, nucleation and growth of Pd nanoparticles were observed on the step edges in some SEM images. Such preference of nucleation on the step edges is

further confirmed by formation of loop-like Pd nanostructures on the HOPG surface, where monatomic pits were developed first by thermal oxidation prior to the growth of Pd nanostructures.

Attempts to prepare nanowires of Ag, Au and Pt from sacrificial Cu films were also carried out, but the results demonstrated that the reduction reaction of the corresponding metal complex ions took place mostly at where Cu films were deposited, and no nanowires were observed on the graphite surface. One possible reason is that the reduction reactions are either energetically or kinetically controlled, which determines the deposition sites of the metal atoms. Thus comprehensive understanding of the adsorption energy between the metal atoms and the substrate surface/step edge sites, as well as the kinetics of the reduction reaction at different sites is required.

As for the future plans, first a more quantitative relationship between the amount of Cu and the diameter of the Pd nanowires can be obtained with stricter environmental control, which can be achieved by installing a small evaporator in a glovebox filled with inert gas such as N<sub>2</sub>. Once the whole process is carried out under inert atmosphere, we can exclude the possible oxidation of the Cu film. Secondly, Pd nanowires have been reported to be removed from the HOPG surface for further applications<sup>119,120,194</sup> like hydrogen sensors. Similar method can be adopted for the Pd nanowire removal in our case, and the continuity of the nanowires can be tested by depositing electrodes at the ends of one nanowire and measuring current-voltage characteristics. And possible application of these nanowires besides hydrogen sensors can be attempted. For example, it is known that Pd can catalyze the electroless

deposition of Cu. Similar idea can be applied if we use the Pd nanowires as templates, and nanowires with core (Pd)-shell (Cu) structure may form subsequently. More interesting structure is possible if we use the loop-like Pd nanostructure for electroless Cu deposition. Thirdly, all our experiments so far used Cu as the sacrificial material, and there are many other metals that can be candidates as sacrificial materials, such as Ni, Fe etc. As we discussed before, the sacrificial metal may also play a key role in determining the deposition sites for the desired metals. Thus fabrication of nanowires of metal other than Pd may be possible by choosing proper sacrificial metals.

#### **4.4 Experimental section:**

##### **Preparation of Cu coated HOPG samples:**

Cu plating solution was made by mixing 3g CuSO<sub>4</sub> (99.0%, J. T. Baker), 14g sodium potassium tartrate (99.3%, Fisher), 4g NaOH (98.5%, J. T. Baker) in 100ml water. A freshly peeled piece of HOPG (10mm×10mm×0.8mm, ZYB grade, MikroMasch) was dipped in a solution of 0.1M Pd(OAc)<sub>2</sub>/0.4M HCl for 1min, rinsed with DI water (>18.0 MΩ·cm, Nanopure, Barnstead), and then dried naturally or by nitrogen. The piece was then put in a mixture of 10ml of the Cu plating solution and 1ml of formaldehyde (37.6%wt, Fisher). The residual Pd on the HOPG surface acts as catalyst which greatly enhanced the reduction speed of Cu<sup>2+</sup> to Cu<sup>0</sup>. The HOPG was taken out of the solution when there was a visible layer of Cu on the HOPG surface, which usually took a few minutes. It was rinsed with DI water and dried naturally or by nitrogen. Scorch tape was used to peel both the top and bottom surfaces of the

HOPG, and sand paper was used to get rid of Cu on 3 sides of the HOPG, leaving only one side coated with Cu.

Recently we are trying vacuum evaporation to coat the HOPG sample with Cu. The experiment was conducted in a vacuum evaporator (DV-503, Denton Vacuum). One side of the HOPG faced upwards and Cu (99.99%, Strem Chemicals) was evaporated from a W basket ~25cm above the sample. The thickness of Cu was carefully controlled. The top and bottom surfaces of the HOPG were then peeled by Scorch tape to give fresh surfaces for preparation of Pd nanostructures.

#### **Preparation of Pd nanowires on HOPG.**

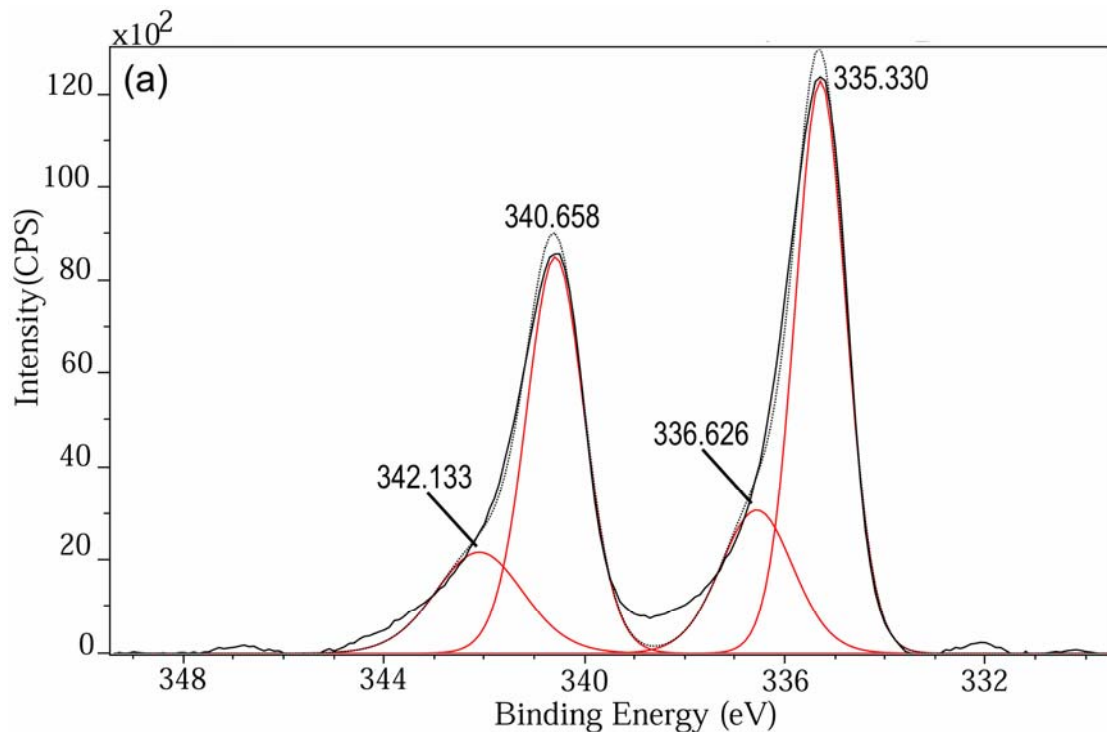
The Cu coated HOPG sample was put in the solution of 0.1M Pd(OAc)<sub>2</sub>/0.4M HCl for 5min. Then the sample was taken out, rinsed with DI water and dried naturally. The color of Cu on the side usually disappeared completely, which indicates the occurrence of the redox reaction.

#### **Characterization of Pd nanostructure.**

AFM studies were performed with a commercial scanning probe microscope (Nanoscope IIIA, Digital Instruments) in a glovebox filled with nitrogen. Commercial Si probes (Nanosensors, force constant 25-55 N/m) with typical tip radius ~15nm were used. Tapping mode was used to minimize the force between the tip and the sample.

The sample was also characterized by SEM (Hitachi S-4700) with base vacuum  $<10^{-5}$  Torr. XPS studies were conducted with a high sensitivity Kratos AXIS 165 spectrometer, with base vacuum better than  $2 \times 10^{-10}$  Torr.

**XPS spectra of Pd and Cu:**



Binding Energy (eV)	Peak assignment	Atomic concentration %	Mass Concentration %
335.330	Pd 3d <sub>5/2</sub>	4.11	19.53
340.658	Pd 3d <sub>3/2</sub>	3.24	15.42
336.626	Pd 3d <sub>5/2</sub>	1.46	6.96
342.133	Pd 3d <sub>3/2</sub>	1.25	5.96

**Figure 68. XPS data from curve fitting of the Pd spectrum.**



## Bibliography

- (1) Ratner, M. A. *Materials Today* **2002**, *5*, 20-27.
- (2) Ross, P. E. In *Forbes*, 1996; Vol. 157, pp 116-117.
- (3) Fuller, D. B.; Akinwande, A. I.; Sodini, C. G. *Industry and Innovation* **2003**, *10*, 179-196.
- (4) Jones, S. W. *Semiconductor International (online)* **08/01/2005**.
- (5) Nuzzo, R. G.; Allara, D. L. *J. Am. Chem. Soc.* **1983**, *105*, 4481-4483.
- (6) Nazin, G. V.; Qiu, X. H.; Ho, W. *Science* **2003**, *302*, 77-81.
- (7) Ramachandran, G. K.; Hopson, T. J.; Rawlett, A. M.; Nagahara, L. A.; Primak, A.; Lindsay, S. M. *Science* **2003**, *300*, 1413-1416.
- (8) Lopinski, G. P.; Wayner, D. D. M.; Wolkow, R. A. *Nature* **2000**, *406*, 48-51.
- (9) Rakshit, T.; Liang, G.-C.; Ghosh, A. W.; Datta, S. *Nano Lett.* **2004**, *4*, 1803-1807.
- (10) He, J.; Chen, B.; Flatt, A. K.; Stephenson, J. J.; Doyle, C. D.; Tour, J. M. *Nature Materials* **2006**, *5*, 63-68.
- (11) He, T.; He, J.; Lu, M.; Chen, B.; Pang, H.; Reus, W. F.; Nolte, W. M.; Nackashi, D. P.; Franzon, P. D.; Tour, J. M. *J. Am. Chem. Soc.* **2006**, *128*, 14537-14541.
- (12) Flatt, A. K.; Chen, B.; Tour, J. M. *J. Am. Chem. Soc.* **2005**, *127*, 8918-8919.
- (13) Tang, J.; Wang, Y.; Klare, J. E.; Tulevski, G. S.; Wind, S. J.; Nuckolls, C. *Angew. Chem., Int. Ed. Engl.* **2007**, *46*, 3892-3895.

- (14) Guo, X.; Small, J. P.; Klare, J. E.; Wang, Y.; Purewal, M. S.; Tam, I. W.; Hong, B. H.; Caldwell, R.; Huang, L.; O'Brien, S.; Yan, J.; Breslow, R.; Wind, S. J.; Hone, J.; Kim, P.; Nuckolls, C. *Science* **2006**, *311*, 356-359.
- (15) Tseng, G. Y.; Ellenbogen, J. C. *Science* **2001**, *294*, 1293-1294.
- (16) Tour, J. M. *Molecular Electronics: Commercial Insights, Chemistry, Devices, Architecture and Programming*; World Scientific Publishing Co. Pte. Ltd., 2003.
- (17) Mann, B.; Kuhn, H. *J. Appl. Phys.* **1971**, *42*, 4398-4405.
- (18) McGinness, J.; Corry, P.; Proctor, P. *Science* **1974**, *183*, 853-855.
- (19) Aviram, A.; Ratner, M. A. *Chem. Phys. Lett.* **1974**, *29*, 277-283.
- (20) Aviram, A. *J. Am. Chem. Soc.* **1988**, *110*, 5687-5692.
- (21) Cui, X. D.; Primak, A.; Zarate, X.; Tomfohr, J.; Sankey, O. F.; Moore, A. L.; Moore, T. A.; Gust, D.; Harris, G.; Lindsay, S. M. *Science* **2001**, *294*, 571-574.
- (22) Wold, D. J.; Frisbie, C. D. *J. Am. Chem. Soc.* **2000**, *122*, 2970-2971.
- (23) Wold, D. J.; Frisbie, C. D. *J. Am. Chem. Soc.* **2001**, *123*, 5549-5556.
- (24) Wold, D. J.; Haag, R.; Rampi, M. A.; Frisbie, C. D. *J. Phys. Chem. B* **2002**, *106*, 2813-2816.
- (25) Ramachandran, G. K.; Tomfohr, J. K.; Li, J.; Sankey, O. F.; Zarate, X.; Primak, A.; Terazono, Y.; Moore, T. A.; Moore, A. L.; Gust, D.; Nagahara, L. A.; Lindsay, S. M. *J. Phys. Chem. B* **2003**, *107*, 6162-6169.
- (26) Cui, X. D.; Primak, A.; Zarate, X.; Tomfohr, J.; Sankey, O. F.; Moore, A. L.; Moore, T. A.; Gust, D.; Nagahara, L. A.; Lindsay, S. M. *J. Phys. Chem. B* **2002**, *106*, 8609-8614.

- (27) Cui, X. D.; Zarate, X.; Tomfohr, J.; Primak, A.; Moore, A. L.; Moore, T. A.; Gust, D.; Harris, G.; Sankey, O. F.; Lindsay, S. M. *Ultramicroscopy* **2002**, *92*, 67-76.
- (28) Cui, X. D.; Zarate, X.; Tomfohr, J.; Sankey, O. F.; Primak, A.; Moore, A. L.; Moore, T. A.; Gust, D.; Harris, G.; Lindsay, S. M. *Nanotechnology* **2002**, *13*, 5-14.
- (29) Leatherman, G.; Durantini, E. N.; Gust, D.; Moore, T. A.; Moore, A. L.; Stone, S.; Zhou, Z.; Rez, P.; Liu, Y. Z.; Lindsay, S. M. *J. Phys. Chem. B* **1999**, *103*, 4006-4010.
- (30) Xiao, X.; Xu, B.; Tao, N. *J. Am. Chem. Soc.* **2004**, *126*, 5370-5371.
- (31) Xiao, X.; Xu, B.; Tao, N. *J. Nano Lett.* **2004**, *4*, 267-271.
- (32) Xu, B.; Tao, N. *J. Science* **2003**, *301*, 1221-1223.
- (33) Xu, B.; Xiao, X.; Tao, N. *J. Am. Chem. Soc.* **2003**, *125*, 16164-16165.
- (34) Xu, B.; Zhang, P.; Li, X.; Tao, N. *Nano Lett.* **2004**, *4*, 1105-1108.
- (35) Morita, T.; Lindsay, S. *J. Am. Chem. Soc.* **2007**, *129*, 7262-7263.
- (36) Beebe, J. M.; Kim, B.; Gadzuk, J. W.; Frisbie, C. D.; Kushmerick, J. G. *Phys. Rev. Lett.* **2006**, *97*, 026801/026801-026801/026804.
- (37) Kim, B.; Beebe, J. M.; Jun, Y.; Zhu, X. Y.; Frisbie, C. D. *J. Am. Chem. Soc.* **2006**, *128*, 4970-4971.
- (38) Fan, F.-R. F.; Lai, R. Y.; Cornil, J.; Karzazi, Y.; Bredas, J.-L.; Cai, L.; Cheng, L.; Yao, Y.; Price, D. W., Jr.; Dirk, S. M.; Tour, J. M.; Bard, A. J. *J. Am. Chem. Soc.* **2004**, *126*, 2568-2573.

- (39) Fan, F.-R. F.; Yang, J.; Cai, L.; Price, D. W., Jr.; Dirk, S. M.; Kosynkin, D. V.; Yao, Y.; Rawlett, A. M.; Tour, J. M.; Bard, A. J. *J. Am. Chem. Soc.* **2002**, *124*, 5550-5560.
- (40) Fan, F.-R. F.; Yang, J.; Dirk, S. M.; Price, D. W.; Kosynkin, D.; Tour, J. M.; Bard, A. J. *J. Am. Chem. Soc.* **2001**, *123*, 2454-2455.
- (41) Fan, F.-R. F.; Yao, Y.; Cai, L.; Cheng, L.; Tour, J. M.; Bard, A. J. *J. Am. Chem. Soc.* **2004**, *126*, 4035-4042.
- (42) Ishida, T.; Mizutani, W.; Choi, N.; Akiba, U.; Fujihira, M.; Tokumoto, H. *J. Phys. Chem. B* **2000**, *104*, 11680-11688.
- (43) Cygan, M. T.; Dunbar, T. D.; Arnold, J. J.; Bumm, L. A.; Shedlock, N. F.; Burgin, T. P.; Jones, L., II; Allara, D. L.; Tour, J. M.; Weiss, P. S. *J. Am. Chem. Soc.* **1998**, *120*, 2721-2732.
- (44) Donhauser, Z. J.; Mantoosh, B. A.; Kelly, K. F.; Bumm, L. A.; Monnell, J. D.; Stapleton, J. J.; Price, D. W., Jr.; Rawlett, A. M.; Allara, D. L.; Tour, J. M.; Weiss, P. S. *Science* **2001**, *292*, 2303-2307.
- (45) Dunbar, T. D.; Cygan, M. T.; Bumm, L. A.; McCarty, G. S.; Burgin, T. P.; Reinerth, W. A.; Jones, L., II; Jackiw, J. J.; Tour, J. M.; Weiss, P. S.; Allara, D. L. *J. Phys. Chem. B* **2000**, *104*, 4880-4893.
- (46) Chen, J.; Calvet, L. C.; Reed, M. A.; Carr, D. W.; Grubisha, D. S.; Bennett, D. W. *Chem. Phys. Lett.* **1999**, *313*, 741-748.
- (47) Chen, J.; Reed, M. A. *Chem. Phys.* **2002**, *281*, 127-145.
- (48) Chen, J.; Reed, M. A.; Rawlett, A. M.; Tour, J. M. *Science* **1999**, *286*, 1550-1552.

- (49) Chen, J.; Wang, W.; Reed, M. A.; Rawlett, A. M.; Price, D. W.; Tour, J. M. *Appl. Phys. Lett.* **2000**, *77*, 1224-1226.
- (50) Wang, W.; Lee, T.; Kretzschmar, I.; Reed, M. A. *Nano Lett.* **2004**, *4*, 643-646.
- (51) Zhou, C.; Deshpande, M. R.; Reed, M. A.; Jones, K., II; Tour, J. M. *Appl. Phys. Lett.* **1997**, *71*, 611-613.
- (52) Chabynyc, M. L.; Chen, X.; Holmlin, R. E.; Jacobs, H.; Skulason, H.; Frisbie, C. D.; Mujica, V.; Ratner, M. A.; Rampi, M. A.; Whitesides, G. M. *J. Am. Chem. Soc.* **2002**, *124*, 11730-11736.
- (53) Holmlin, R. E.; Haag, R.; Chabynyc, M. L.; Ismagilov, R. F.; Cohen, A. E.; Terfort, A.; Rampi, M. A.; Whitesides, G. M. *J. Am. Chem. Soc.* **2001**, *123*, 5075-5085.
- (54) Haag, R.; Rampi, M. A.; Holmlin, R. E.; Whitesides, G. M. *J. Am. Chem. Soc.* **1999**, *121*, 7895-7906.
- (55) Kushmerick, J. G.; Holt, D. B.; Yang, J. C.; Naciri, J.; Moore, M. H.; Shashidhar, R. *Phys. Rev. Lett.* **2002**, *89*, 086802/086801-086802/086804.
- (56) Kushmerick, J. G.; Naciri, J.; Yang, J. C.; Shashidhar, R. *Nano Lett.* **2003**, *3*, 897-900.
- (57) Kushmerick, J. G.; Holt, D. B.; Pollack, S. K.; Ratner, M. A.; Yang, J. C.; Schull, T. L.; Naciri, J.; Moore, M. H.; Shashidhar, R. *J. Am. Chem. Soc.* **2002**, *124*, 10654-10655.
- (58) Park, H.; Lim, A. K. L.; Alivisatos, A. P.; Park, J.; McEuen, P. L. *Appl. Phys. Lett.* **1999**, *75*, 301-303.

- (59) Park, J.; Pasupathy, A. N.; Goldsmith, J. I.; Chang, C.; Yaish, Y.; Petta, J. R.; Rinkoski, M.; Sethna, J. P.; Abruna, H. D.; McEuen, P. L.; Ralph, D. C. *Nature* **2002**, *417*, 722-725.
- (60) Park, J.; Pasupathy, A. N.; Goldsmith, J. I.; Soldatov, A. V.; Chang, C.; Yaish, Y.; Sethna, J. P.; Abruna, H. D.; Ralph, D. C.; McEuen, P. L. *Thin Solid Films* **2003**, *438-439*, 457-461.
- (61) Liang, W.; Shores, M. P.; Bockrath, M.; Long, J. R.; Park, H. *Nature* **2002**, *417*, 725-729.
- (62) Reed, M. A.; Zhou, C.; Muller, C. J.; Burgin, T. P.; Tour, J. M. *Science* **1997**, *278*, 252-254.
- (63) Engelkes, V. B.; Beebe, J. M.; Frisbie, C. D. *J. Phys. Chem. B* **2005**, *109*, 16801-16810.
- (64) Averin, D. V.; Likharev, K. K. In *Mesoscopic Phenomena in Solids*; Altshuler, B., Lee, P. A., Webb, R. A., Eds.; Elsevier, Amsterdam, 1991, p 173.
- (65) Chen, F.; Li, X.; Hihath, J.; Huang, Z.; Tao, N. *J. Am. Chem. Soc.* **2006**, *128*, 15874-15881.
- (66) Li, X.; He, J.; Hihath, J.; Xu, B.; Lindsay, S. M.; Tao, N. *J. Am. Chem. Soc.* **2006**, *128*, 2135-2141.
- (67) Tao, N. *J. Mater. Chem.* **2005**, *15*, 3260-3263.
- (68) Venkataraman, L.; Klare, J. E.; Tam, I. W.; Nuckolls, C.; Hybertsen, M. S.; Steigerwald, M. L. *Nano Lett.* **2006**, *6*, 458-462.
- (69) Venkataraman, L.; Park, Y. S.; Whalley, A. C.; Nuckolls, C.; Hybertsen, M. S.; Steigerwald, M. L. *Nano Lett.* **2007**, *7*, 502-506.

- (70) Jo, M.-H.; Grose, J. E.; Baheti, K.; Deshmukh, M. M.; Sokol, J. J.; Rumberger, E. M.; Hendrickson, D. N.; Long, J. R.; Park, H.; Ralph, D. C. *Nano Lett.* **2006**, *6*, 2014-2020.
- (71) Averin, D. V.; Nazarov, Y. V. In *Single Charge Tunneling: Coulomb Blockade Phenomena in Nanostructures*; Grabert, H., Devoret, M. H., Eds.; Plenum Press and NATO Scientific Affairs Division: New York, 1992, p 217.
- (72) Kondo, J. *Progr. Theoret. Phys. (Kyoto)* **1964**, *32*, 37-69.
- (73) Collier, C. P.; Wong, E. W.; Belohradsky, M.; Raymo, F. M.; Stoddart, J. F.; Kuekes, P. J.; Williams, R. S.; Heath, J. R. *Science* **1999**, *285*, 391-394.
- (74) Collier, C. P.; Matterstei, G.; Wong, E. W.; Luo, Y.; Beverly, K.; Sampaio, J.; Raymo, F. M.; Stoddart, J. F.; Heath, J. R. *Science* **2000**, *289*, 1172-1175.
- (75) Lau, C. N.; Stewart, D. R.; Williams, R. S.; Bockrath, M. *Nano Lett.* **2004**, *4*, 569-572.
- (76) Moore, A. M.; Dameron, A. A.; Mantooth, B. A.; Smith, R. K.; Fuchs, D. J.; Ciszek, J. W.; Maya, F.; Yao, Y.; Tour, J. M.; Weiss, P. S. *J. Am. Chem. Soc.* **2006**, *128*, 1959-1967.
- (77) Lindsay, S. *Faraday Discussions* **2006**, *131*, 403-409.
- (78) Houck, A. A.; Labaziewicz, J.; Chan, E. K.; Folk, J. A.; Chuang, I. L. *Nano Lett.* **2005**, *5*, 1685-1688.
- (79) Kaun, C.-C.; Guo, H. *Nano Lett.* **2003**, *3*, 1521-1525.
- (80) Kaun, C.-C.; Larade, B.; Guo, H. *Phys. Rev. B* **2003**, *67*, 121411/121411-121411/121414.

- (81) Xue, Y.; Ratner, M. A. *Phys. Rev. B* **2003**, *68*, 115407/115401-115407/115411.
- (82) Xue, Y.; Ratner, M. A. *Phys. Rev. B* **2003**, *68*, 115406/115401-115406/115418.
- (83) Engtrakul, C.; Sita, L. R. *Nano Lett.* **2001**, *1*, 541-549.
- (84) Engtrakul, C. *Ferrocene-based nanoelectronics: design, synthesis, and evaluation.[Ph.D. dissertation]*; University of Maryland: College Park, 2003.
- (85) Binnig, G.; Quate, C. F.; Gerber, C. *Phys. Rev. Lett.* **1986**, *56*, 930-933.
- (86) Chen, L.; Cheung, C. L.; Ashby, P. D.; Lieber, C. M. *Nano Lett.* **2004**, *4*, 1725-1731.
- (87) Hafner, J. H.; Cheung, C.-L.; Oosterkamp, T. H.; Lieber, C. M. *J. Phys. Chem. B* **2001**, *105*, 743-746.
- (88) Yenilmez, E.; Wang, Q.; Chen, R. J.; Wang, D.; Dai, H. *Appl. Phys. Lett.* **2002**, *80*, 2225-2227.
- (89) Langmuir, I. *J. Am. Chem. Soc.* **1917**, *39*, 1848-1906.
- (90) Blodgett, K. B. *J. Am. Chem. Soc.* **1935**, *57*, 1007-1022.
- (91) Love, J. C.; Estroff Lara, A.; Kriebel Jennah, K.; Nuzzo Ralph, G.; Whitesides George, M. *Chemical reviews* **2005**, *105*, 1103-1169.
- (92) Bain, C. D.; Troughton, E. B.; Tao, Y. T.; Evall, J.; Whitesides, G. M.; Nuzzo, R. G. *J. Am. Chem. Soc.* **1989**, *111*, 321-335.
- (93) Frens, G. *Nature (London), Physical Science* **1973**, *241*, 20-22.
- (94) Hirai, H.; Aizawa, H. *J. Colloid Interface Sci.* **1993**, *161*, 471-474.



- (95) Binning, G.; Rohrer, H.; Gerber, C.; Weibel, E. *Phys. Rev. Lett.* **1982**, *49*, 57-61.
- (96) Lindahl, J.; Takanen, T.; Montelius, L. *J. Vac. Sci. Technol., B* **1998**, *16*, 3077-3081.
- (97) Melmed, A. J. *J. Vac. Sci. Technol., B* **1991**, *9*, 601-608.
- (98) Fotino, M. *Appl. Phys. Lett.* **1992**, *60*, 2935-2937.
- (99) Bumm, L. A.; Arnold, J. J.; Dunbar, T. D.; Allara, D. L.; Weiss, P. S. *J. Phys. Chem. B* **1999**, *103*, 8122-8127.
- (100) Poirier, G. E. *Langmuir* **1997**, *13*, 2019-2026.
- (101) Poirier, G. E.; Fitts, W. P.; White, J. M. *Langmuir* **2001**, *17*, 1176-1183.
- (102) Poirier, G. E.; Tarlov, M. J.; Rushmeier, H. E. *Langmuir* **1994**, *10*, 3383-3386.
- (103) Fitts, W. P.; White, J. M.; Poirier, G. E. *Langmuir* **2002**, *18*, 2096-2102.
- (104) Fitts, W. P.; White, J. M.; Poirier, G. E. *Langmuir* **2002**, *18*, 1561-1566.
- (105) Poirier, G. E.; Herne, T. M.; Miller, C. C.; Tarlov, M. J. *J. Am. Chem. Soc.* **1999**, *121*, 9703-9711.
- (106) Chen, S.; Li, L.; Boozer, C. L.; Jiang, S. *Langmuir* **2000**, *16*, 9287-9293.
- (107) Chen, S.; Li, L.; Boozer, C. L.; Jiang, S. *J. Phys. Chem. B* **2001**, *105*, 2975-2980.
- (108) Noh, J.; Hara, M. *Langmuir* **2000**, *16*, 2045-2048.
- (109) Kelly, K. F.; Shon, Y. S.; Lee, T. R.; Halas, N. J. *J. Phys. Chem. B* **1999**, *103*, 8639-8642.
- (110) Weare, W. W.; Reed, S. M.; Warner, M. G.; Hutchison, J. E. *J. Am. Chem. Soc.* **2000**, *122*, 12890-12891.

- (111) Getty, S. A.; Engtrakul, C.; Wang, L.; Liu, R.; Ke, S.-H.; Baranger, H. U.; Yang, W.; Fuhrer, M. S.; Sita, L. R. *Phys. Rev. B* **2005**, *71*, 241401/241401-241401/241404.
- (112) Yang, Z.; Lang, N. D.; Di Ventra, M. *Appl. Phys. Lett.* **2003**, *82*, 1938-1940.
- (113) Slot, E.; Holst, M. A.; Van der Zant, H. S. J.; Zaitsev-Zotov, S. V. *Physical Review Letters* **2004**, *93*, 176602/176601-176602/176604.
- (114) Sosa, I. O.; Noguez, C.; Barrera, R. G. *Journal of Physical Chemistry B* **2003**, *107*, 6269-6275.
- (115) Opitz, J.; Zahn, P.; Mertig, I. *Physical Review B: Condensed Matter and Materials Physics* **2002**, *66*, 245417/245411-245417/245419.
- (116) Schmid, G. *Encyclopedia of Nanoscience and Nanotechnology* **2004**, *5*, 387-398.
- (117) Gopal, V.; Stach, E. A.; Radmilovic, V. R.; Mowat, I. A. *Applied Physics Letters* **2004**, *85*, 49-51.
- (118) Oon, C. H.; Thong, J. T. L. *Nanotechnology* **2004**, *15*, 687-691.
- (119) Favier, F.; Walter, E. C.; Zach, M. P.; Benter, T.; Penner, R. M. *Science (Washington, DC, United States)* **2001**, *293*, 2227-2231.
- (120) Walter, E. C.; Penner, R. M.; Liu, H.; Ng, K. H.; Zach, M. P.; Favier, F. *Surface and Interface Analysis* **2002**, *34*, 409-412.
- (121) Yun, M.; Myung, N. V.; Vasquez, R. P.; Lee, C.; Menke, E.; Penner, R. M. *Nano Letters* **2004**, *4*, 419-422.
- (122) Bangar, M. A.; Ramanathan, K.; Yun, M.; Lee, C.; Hangarter, C.; Myung, N. V. *Chemistry of Materials* **2004**, *16*, 4955-4959.

- (123) Han, L.; Shi, X.; Wu, W.; Kirk, F. L.; Luo, J.; Wang, L.; Mott, D.; Cousineau, L.; Lim, S. I. I.; Lu, S.; Zhong, C.-J. *Sensors and Actuators, B: Chemical* **2005**, *B106*, 431-441.
- (124) Nath, N.; Chilkoti, A. *Analytical Chemistry* **2002**, *74*, 504-509.
- (125) Murray, B. J.; Newberg, J. T.; Walter, E. C.; Li, Q.; Hemminger, J. C.; Penner, R. M. *Analytical Chemistry* **2005**, *77*, 5205-5214.
- (126) Sellmyer, D. J.; Zheng, M.; Skomski, R. *Journal of Physics: Condensed Matter* **2001**, *13*, R433-R460.
- (127) Skomski, R.; Zeng, H.; Zheng, M.; Sellmyer, D. J. *Physical Review B: Condensed Matter and Materials Physics* **2000**, *62*, 3900-3904.
- (128) He, H.; Tao, N. J. *Encyclopedia of Nanoscience and Nanotechnology* **2004**, *2*, 755-772.
- (129) Roucoux, A.; Schulz, J.; Patin, H. *Chemical Reviews (Washington, DC, United States)* **2002**, *102*, 3757-3778.
- (130) Iijima, S. *Nature (London, United Kingdom)* **1991**, *354*, 56-58.
- (131) Fullam, S.; Cottell, D.; Rensmo, H.; Fitzmaurice, D. *Advanced Materials (Weinheim, Germany)* **2000**, *12*, 1430-1432.
- (132) Bezryadin, A.; Lau, C. N.; Tinkham, M. *Nature (London)* **2000**, *404*, 971-974.
- (133) Zhang, Y.; Dai, H. *Applied Physics Letters* **2000**, *77*, 3015-3017.
- (134) Choi, H. C.; Shim, M.; Bangsaruntip, S.; Dai, H. *Journal of the American Chemical Society* **2002**, *124*, 9058-9059.
- (135) Kim, H. J.; Roh, Y.; Hong, B. *Journal of Vacuum Science & Technology, A: Vacuum, Surfaces, and Films* **2006**, *24*, 1327-1331.

- (136) Nishinaka, T.; Takano, A.; Doi, Y.; Hashimoto, M.; Nakamura, A.; Matsushita, Y.; Kumaki, J.; Yashima, E. *Journal of the American Chemical Society* **2005**, *127*, 8120-8125.
- (137) Hashimoto, Y.; Matsuo, Y.; Ijiro, K. *Chemistry Letters* **2005**, *34*, 112-113.
- (138) Park, S. H.; Prior, M. W.; LaBean, T. H.; Finkelstein, G. *Applied Physics Letters* **2006**, *89*, 033901/033901-033901/033903.
- (139) Gu, Q.; Cheng, C.; Haynie, D. T. *Nanotechnology* **2005**, *16*, 1358-1363.
- (140) Ijiro, K.; Matsuo, Y.; Hashimoto, Y. *e-Journal of Surface Science and Nanotechnology* **2005**, *3*, 82-85.
- (141) Quake, S. R.; Scherer, A. *Science* **2000**, *290*, 1536-1540.
- (142) Hopkins, D. S.; Pekker, D.; Goldbart, P. M.; Bezryadin, A. *Science (Washington, DC, United States)* **2005**, *308*, 1762-1765.
- (143) Remeika, M.; Bezryadin, A. *Nanotechnology* **2005**, *16*, 1172-1176.
- (144) Minko, S.; Kiriya, A.; Gorodyska, G.; Stamm, M. *Journal of the American Chemical Society* **2002**, *124*, 10192-10197.
- (145) Kiriya, A.; Minko, S.; Gorodyska, G.; Stamm, M.; Jaeger, W. *Nano Letters* **2002**, *2*, 881-885.
- (146) Djalali, R.; Li, S.-Y.; Schmidt, M. *Macromolecules* **2002**, *35*, 4282-4288.
- (147) Keller, F.; Hunter, M. S.; Robinson, D. L. *Journal of the Electrochemical Society* **1953**, *100*, 411-419.
- (148) Masuda, H.; Fukuda, K. *Science (Washington, D. C.)* **1995**, *268*, 1466-1468.
- (149) Masuda, H.; Yamada, H.; Satoh, M.; Asoh, H.; Nakao, M.; Tamamura, T. *Applied Physics Letters* **1997**, *71*, 2770-2772.

- (150) Zhao, W.-B.; Zhu, J.-J.; Chen, H.-Y. *Journal of Crystal Growth* **2003**, *258*, 176-180.
- (151) Strijkers, G. J.; Dalderop, J. H. J.; Broeksteeg, M. A. A.; Swagten, H. J. M.; de Jonge, W. J. M. *Journal of Applied Physics* **1999**, *86*, 5141-5145.
- (152) Wang, X. W.; Fei, G. T.; Xu, X. J.; Jin, Z.; Zhang, L. D. *Journal of Physical Chemistry B* **2005**, *109*, 24326-24330.
- (153) Chu, S.-Z.; Inoue, S.; Wada, K.; Kurashima, K. *Journal of Physical Chemistry B* **2004**, *108*, 5582-5587.
- (154) Ji, G. B.; Tang, S. L.; Gu, B. X.; Du, Y. W. *Journal of Physical Chemistry B* **2004**, *108*, 8862-8865.
- (155) Zhan, Q.; Chen, Z.; Xue, D.; Li, F.; Kunkel, H.; Zhou, X.; Roshko, R.; Williams, G. *Physical Review B: Condensed Matter and Materials Physics* **2002**, *66*, 134436/134431-134436/134436.
- (156) Saedi, A.; Ghorbani, M. *Materials Chemistry and Physics* **2005**, *91*, 417-423.
- (157) Liang, H.-P.; Guo, Y.-G.; Hu, J.-S.; Zhu, C.-F.; Wan, L.-J.; Bai, C.-L. *Inorganic Chemistry* **2005**, *44*, 3013-3015.
- (158) Nicewarner-Pena, S. R.; Griffith Freeman, R.; Reiss, B. D.; He, L.; Pena, D. J.; Walton, I. D.; Cromer, R.; Keating, C. D.; Natan, M. J. *Science (Washington, DC, United States)* **2001**, *294*, 137-141.
- (159) Yi, G.; Schwarzacher, W. *Applied Physics Letters* **1999**, *74*, 1746-1748.
- (160) Tian, M.; Wang, J.; Snyder, J.; Kurtz, J.; Liu, Y.; Schiffer, P.; Mallouk, T. E.; Chan, M. H. W. *Applied Physics Letters* **2003**, *83*, 1620-1622.

- (161) Wirtz, M.; Martin, C. R. *Advanced Materials (Weinheim, Germany)* **2003**, *15*, 455-458.
- (162) Li, G.-R.; Tong, Y.-X.; Kay, L.-G.; Liu, G.-K. *Journal of Physical Chemistry B* **2006**, *110*, 8965-8970.
- (163) Liu, K.; Nagodawithana, K.; Searson, P. C.; Chien, C. L. *Physical Review B: Condensed Matter* **1995**, *51*, 7381-7384.
- (164) Wang, J.-G.; Tian, M.-L.; Mallouk, T. E.; Chan, M. H. W. *Nano Letters* **2004**, *4*, 1313-1318.
- (165) Thurn-Albrecht, T.; Schotter, J.; Kastle, G. A.; Emley, N.; Shibauchi, T.; Krusin-Elbaum, L.; Guarini, K.; Black, C. T.; Tuominen, M. T.; Russell, T. P. *Science (Washington, D. C.)* **2000**, *290*, 2126-2129.
- (166) Bal, M.; Ursache, A.; Touminen, M. T.; Goldbach, J. T.; Russell, T. P. *Applied Physics Letters* **2002**, *81*, 3479-3481.
- (167) Ajayan, P. M.; Iijima, S. *Nature (London, United Kingdom)* **1993**, *361*, 333-334.
- (168) Guerret-Piecourt, C.; Le Bouar, Y.; Loiseau, A.; Pascard, H. *Nature (London)* **1994**, *372*, 761-765.
- (169) Démoncy, N.; Stephan, O.; Brun, N.; Colliex, C.; Loiseau, A.; Pascard, H. *European Physical Journal B: Condensed Matter Physics* **1998**, *4*, 147-157.
- (170) Liu, S.; Tang, X.; Mastai, Y.; Felner, I.; Gedanken, A. *Journal of Materials Chemistry* **2000**, *10*, 2502-2506.
- (171) Liu, S.; Zhu, J.; Mastai, Y.; Felner, I.; Gedanken, A. *Chemistry of Materials* **2000**, *12*, 2205-2211.

- (172) Satishkumar, B. C.; Taubert, A.; Luzzi, D. E. *Journal of Nanoscience and Nanotechnology* **2003**, *3*, 159-163.
- (173) Kawamura, M.; Paul, N.; Cherepanov, V.; Voigtlander, B. *Physical Review Letters* **2003**, *91*, 096102/096101-096102/096104.
- (174) Bode, M.; Kubetzka, A.; Pietzsch, O.; Wiesendanger, R. *Surface Science* **2002**, *514*, 135-144.
- (175) Prokop, J.; Kukunin, A.; Elmers, H. J. *Physical review letters* **2005**, *95*, 187202.
- (176) McChesney, J. L.; Crain, J. N.; Himpsel, F. J.; Bennowitz, R. *Physical Review B: Condensed Matter and Materials Physics* **2005**, *72*, 035446/035441-035446/035444.
- (177) Himpsel, F. J.; McChesney, J. L.; Crain, J. N.; Kirakosian, A.; Perez-Dieste, V.; Abbott, N. L.; Luk, Y.-Y.; Nealey, P. F.; Petrovykh, D. Y. *Journal of Physical Chemistry B* **2004**, *108*, 14484-14490.
- (178) Petrovykh, D. Y.; Himpsel, F. J.; Jung, T. *Surface Science* **1998**, *407*, 189-199.
- (179) Blanc, M.; Kuhnke, K.; Marsico, V.; Kern, K. *Surface Science* **1998**, *414*, L964-L969.
- (180) Gambardella, P.; Blanc, M.; Brune, H.; Kuhnke, K.; Kern, K. *Physical Review B* **2000**, *61*, 2254-2262.
- (181) de la Figuera, J.; Huerta-Garnica, M. A.; Prieto, J. E.; Ocal, C.; Miranda, R. *Applied Physics Letters* **1995**, *66*, 1006-1008.
- (182) Cross, C. E.; Hemminger, J. C.; Penner, R. M. *Langmuir* **2007**, *23*, 10372-10379.

- (183) Zach, M. P.; Inazu, K.; Ng, K. H.; Hemminger, J. C.; Penner, R. M. *Chemistry of Materials* **2002**, *14*, 3206-3216.
- (184) Zach, M. P.; Ng, K. H.; Penner, R. M. *Science (Washington, D. C.)* **2000**, *290*, 2120-2123.
- (185) Penner, R. M. *Journal of Physical Chemistry B* **2002**, *106*, 3339-3353.
- (186) Walter, E. C.; Murray, B. J.; Favier, F.; Kaltenpoth, G.; Grunze, M.; Penner, R. M. *Journal of Physical Chemistry B* **2002**, *106*, 11407-11411.
- (187) Walter, E. C.; Zach, M. P.; Favier, F.; Murray, B. J.; Inazu, K.; Hemminger, J. C.; Penner, R. M. *ChemPhysChem* **2003**, *4*, 131-138.
- (188) Dryfe, R. A. W.; Walter, E. C.; Penner, R. M. *ChemPhysChem* **2004**, *5*, 1879-1884.
- (189) Eugster, N.; Fermin, D. J.; Girault, H. H. *Journal of Physical Chemistry B* **2002**, *106*, 3428-3433.
- (190) Hoevel, H.; Becker, T.; Bettac, A.; Reihl, B.; Tschudy, M.; Williams, E. J. *Journal of Applied Physics* **1997**, *81*, 154-158.
- (191) Heszler, P.; Revesz, K.; Reimann, C. T.; Mechler, A.; Bor, Z. *Nanotechnology* **2000**, *11*, 37-43.
- (192) Hennig, G. R. *Journal of Chemical Physics* **1964**, *40*, 2877-2882.
- (193) Yang, R. T.; Wong, C. *Journal of Chemical Physics* **1981**, *75*, 4471-4476.
- (194) Walter, E. C.; Favier, F.; Penner, R. M. *Analytical Chemistry* **2002**, *74*, 1546-1553.